Doctoral Dissertation

Study on Cell Performance and Durability of High-Temperature Proton Exchange Membrane Fuel Cells

December, 2013

Yuka Oono

Contents

Chapter 1
Introduction

1.1 Background

Fuel cells have attracted considerable attention as an environmentally friendly, clean energy system and a broad range of research has been conducted in this area. Presently, the most actively studied fuel cell is the perfluorosulfonic acid-type low temperature proton exchange membrane fuel cell (LT-PEMFC). The LT-PEMFC is different from previous generation fuel cells in that it uses a solid polymer membrane as the electrolyte, so that it conducts protons via water, and can therefore operate in the temperature range below 100 ◦C. Consequently, the LT-PEMFC has extended the range of applications of fuel cells to small-scale power sources for automobiles, portable and residential use, and this trend is expected to continue into the future. The recent trend in Japan is the commercialization of 1 kW-class domestic cogeneration systems using both electricity and electrically generated waste heat[1-6], due to significant improvements in fuel cell performance and durability[7,8]. However, a major stumbling block for commercialization is that the system tends to be very complex and expensive because LT-PEMFC inherently requires humidification for proton conduction via water. In addition, the system efficiency is relatively low due to the low operating temperature of <100℃[7], and it requires a CO selective oxidizer as the CO resistance of the electrode catalyst is reduced at lower temperatures[9–12].

The development of next generation PEMFC is actively being researched in order to solve these problems by simplification of the system, reduction of production costs, and improvement of the operational efficiency in the temperature range of 135–160℃[13,14]. In addition, next generation PEMFC must have sufficient heat resistance under zero humidification conditions, and be based on polymer electrolytic membranes that can chemically couple with acids capable of proton conduction. Research has been conducted on acids that are capable of proton conduction at temperatures exceeding 100 ℃, in addition to various polymers that adsorb acids[15–23], and the results suggest that sulfuric and phosphoric acids have high proton conduction capability[24–26]. With regard to the polymers that form the structure of the membranes, various elementary studies have

been carried out on polybenzimidazole (PBI)[27], polyethylene oxide (PEO)[28], polyvinyl alcohol (PVA) [29-32], polyacrylamide (PAAM) [33,34] and polyethylenimine (PEI) [35].

It is thought that one of the most promising candidates of the membranes for a high-temperature proton exchange membrane fuel cell (HT-PEMFC) is the phosphoric acid-doped PBI-based membrane (PBI-H_3PO_4). HT-PEMFC does not require large shift converters or selective oxidizers due to their high CO tolerance, which exceeds 10,000ppm[9-12]. Neither do they require humidifiers, because proton transport in the PEM occurs without water dragging[36,37]. They can also be used without vaporizers for supplying steam to a fuel reformer, because the vapor produced by electrode-reaction thermal heat is recirculated. HT-PEMFC is anticipated to be used for residential applications, because they are cheaper and more efficient than phosphoric acid fuel cells (PAFC) [38-41].

1.2 HT-PEMFC

1.2.1 Power generation principle of HT-PEMFC

Fuel cells are classified into several types by the difference in the operating temperature range and the difference in the electrolyte. A proton exchange membrane (PEM) is usually used as the electrolyte layer of PEMFC. The membrane is sandwiched by both the air and fuel electrode layers. With supplying reactant gases to the electrodes, the electrode reaction occurs in the "three-phase interface" where electrode catalyst, electrolyte and reactant gas contact. At an anode electrode, as shown in equation (1-1), hydrogen is oxidized to generate protons (H^+).

$$H_2 \rightarrow 2H^+ + 2e^- \qquad (1\text{-}1)$$

This proton is transferred from anode side to cathode side through PEM accompanied by water molecules. At this time, the electrons pass through the external circuit. Equation (1-2) shows the reaction at a cathode electrode. As shown in the equation, water is produced with electrons and protons moved from the anode side being used for the reduction of oxygen. At this time, current flows from cathode side to anode side.

$$1/2O_2 + 2H^+ + 2e^- \rightarrow H_2O \qquad (1\text{-}2)$$

Equation (1-3) shows the entire electrode reaction of PEMFC. As shown in the equation, the carbon dioxide is not exhausted from the electrode reaction of PEMFC.

$$H_2 + 1/2O_2 \rightarrow H_2O \qquad (1\text{-}3)$$

In these cases, the theoretical electrode potential of a single fuel cell is 1.23V, which is driven from the equations (1-1) to (1-3), the standard electrode potential from Gibbs equation, and the Nernst equation. However, even the open circuit voltage actually becomes lower than the theoretical electrode potential due to various losses. In fact, the cell voltage of PEMFC is 0.95V-1.0V at most.

1.2.2 PBI-based membrane for HT-PEMFC

Phosphoric acid- doped PBI was first proposed as an electrolyte material in 1995[42], and since then membranes have been developed and characterized [43]. High conductivity [17,36], good mechanical properties [38,45] and excellent thermal stability [46] at temperature of up to 200℃ and ambient pressure have been reported. Efforts have been made to modify the polymer structures, aiming at optimizing polymer properties such as molecular weight, solubility and processibility as well as tailoring the basicity of polymers for acid-base interactions.

This has been accomplished in two ways, either by synthetically modifying the monomers prior to polymerization or by post-polymerization substitution of the polymer at the reactive benzimidazole N-H sites. Examples of modified PBI include(poly[2,2'-(phenylene)-5,5'- benzimidazole]) [47-50], pyridine-containing PBI [49-51], AB-PBI [52,53], napfthalene-PBI [51], sulfone-PBI [54], dihydroxy-PBI [55], and hexafluoro PBI [56,57]. The NH groups in the imidazole rings are reactive, allowing for N-substitution (e.g., sulfonation) [58] or cross-linking of polymer [59-62].

1.2.3 HT-PEMFC with PBI-H_3PO_4

Since phosphoric acid- doped PBI (PBI-H_3PO_4) was proposed in 1995 [42], various studies were started using it [63,64]. Especially, studies have focused on HT-PEMFC with PBI-H_3PO_4, from the point of view of membrane conductivity and heat resistance[36,65-67], and the power generation of actual cells [43,68-77]. Zhang et al. reported that higher cell performance

was achieved as the operating temperature approached 200℃ [13]. In addition, the results of long-term power generation tests (exceeding 10,000 h) have been reported by BASF and Samsung [9,78], and these PEMFC are considered to be the closest to commercialization.

1.3 Cell configuration of HT-PEMFC

1.3.1 Cell assembly

Fig.1.1 shows the diagram of the cell configuration of a HT-PEMFC. As shown in the figure, HT-PEMFC consists of PEM, catalyst layers on its both surfaces, and gas diffusion layers (GDL) on their outer surfaces. An assembly of membrane, catalyst layers and gas diffusion layers is named as "Membrane Electrode Assembly (MEA)". Cell appearance of HT-PEMFC is almost the same as that of LT-PEMFC. Furthermore, bi-polar plates are arranged on both sides of the MEA. And the reformed gas including hydrogen and dry air are supplied the respective anode and cathode sides of the bi-polar plates.

In case of LT-PEMFC, the hydrocarbon or perfluorosulfonic acid proton exchange membranes are usually used as electrolyte membranes. In case of HT- PEMFC of this study, the polymer film, such as imidazole group, which is doped with phosphoric acid is used as an electrolyte membrane.

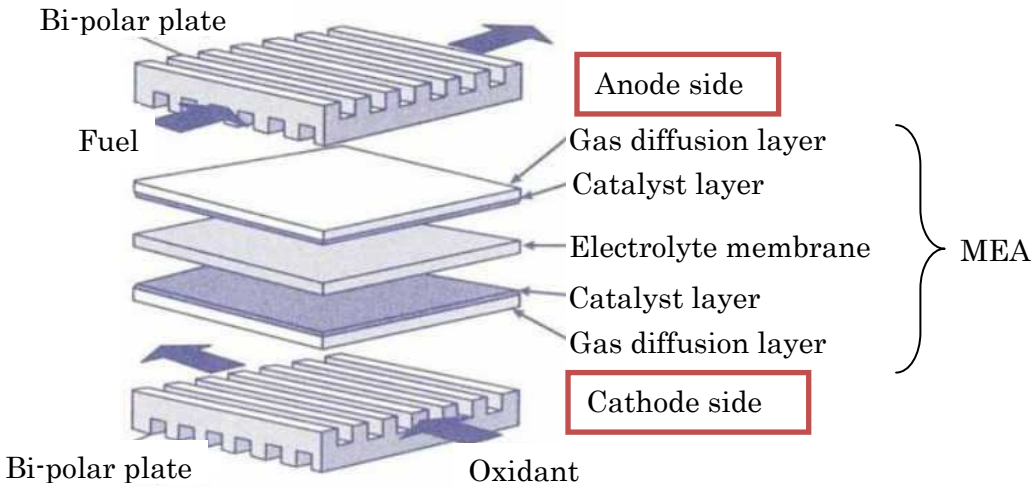

Fig.1.1 Diagram of the cell configuration of HT-PEFC

1.3.2 Catalyst layer

The catalyst layer (CL) of HT-PEMFC is a thin layer of a few tens μm thick. It consists of carbon particles supported -catalysts and the fluorine-based resin as a water repellent and a binder. Usually platinum-based electrode catalysts are used for both the anode and cathode sides in order to reduce an activation overvoltage. Fig.1.2 shows a high magnification electron micrograph of carbon-supported platinum catalyst used in the electrode of HT-PEMFC. As shown in the figure, the platinum catalysts are fine particles with the diameter of 2 to 5nm, their specific surface area is about 50 to 200$m^2\ g^{-1}$. Meanwhile, the particle diameter of the carbon supports used in this study is about 20 to 40nm, the specific surface area extends to the 200 to 800$m^2\ g^{-1}$.

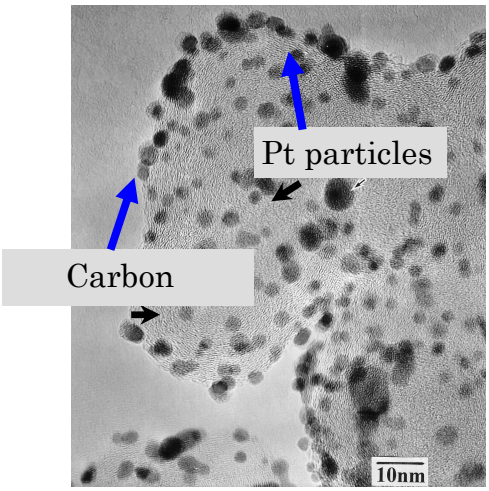

Fig.1.2 High magnification electron micrograph of carbon-supported platinum catalyst

1.3.3 Gas diffusion layer

In the case of HT-PEMFC as well as LT-PEMFC, the catalyst layers are provided on both surfaces of an electrolyte membrane, the reactant gases are supplied from the opposite sides of the electrolyte membrane to the catalyst layers. Such an electrode is usually called as "a gas diffusion electrode". In the case of HT-PEMFC as well as LT-PEMFC, gas diffusion layers (GDL) are arranged on the opposite sides of the electrolyte membrane of the catalyst layers. And the GDL is composed of carbon paper or cloth of 100 to 300μm thick, which has excellent conductivity and gas permeability. Fig1.3 shows the electron micrograph of carbon paper surface as an example of a gas diffusion layer. As shown in the figure,

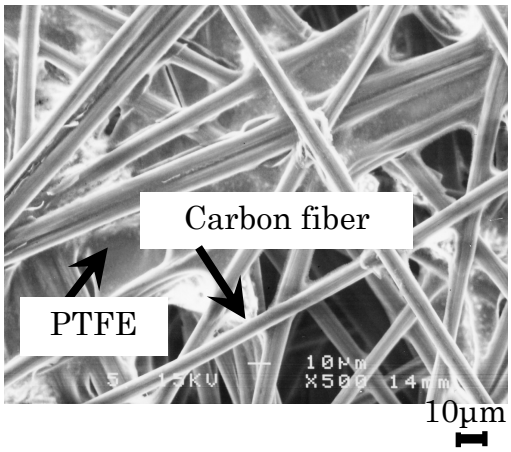

Fig.1.3 Eelectron micrograph of carbon paper surface

the carbon paper consists of carbon fiber with the diameter of about 5μm and polytetrafluoroethylene (PTFE) with strong water repellency. Carbon fibers forms the porosities with the diameter of about a few hundreds μm. PTFE is distributed so as to cross-link the carbon fibers. Fuel and air diffuse into the catalyst layer through the GDL. Conversely, water generated in the catalyst layer of cathode side by the electrode reaction is also discharged to the gas flow channels of bi-polar plate through the GDL.

1.3.4 Bi-polar plate

Fig.1.4 shows an example of the configuration of the bi-polar plate. As shown in the figure, bi-polar plate is a plate with both the air and fuel gas channels. The bi-polar plate has the other functions than such a gas flow; the function of separating fuel and air, the gas manifold function of supplying fuel and air to each cell and discharging the unused gas and generated water to the outside of cell stack, the function of collecting the electricity generated by the electrode reaction, the gas seal function of avoiding gas leak from the inside of cell stack to its outside and so on.

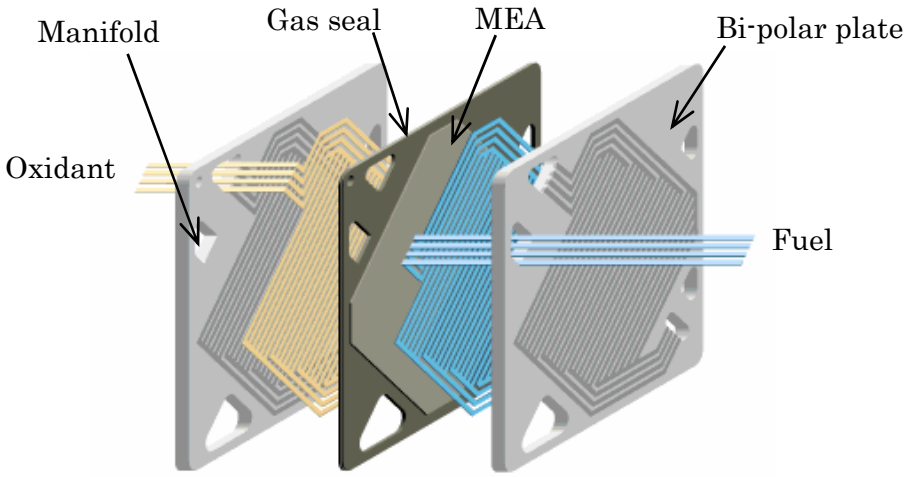

Fig.1.4 An example of bi-polar plate configuration

1.3.5 Cell stack configuration

Cell voltage that can be generated by one cell of not only LT-PEMFC but also HT-PEMFC is at most about 0.7 to 0.8 V. However, in the actual system of PEMFC, further higher voltage is required. In order to obtain such a high voltage, it is generally stacked to join together a required number of cells in series. Fig.1.5 schematically shows the configuration of the cell stack of HT-PEMFC. As shown in the figure, the call stack is assembled by stacking

alternately several tens or hundreds MEAs and bi-polar plates and by tightening them.

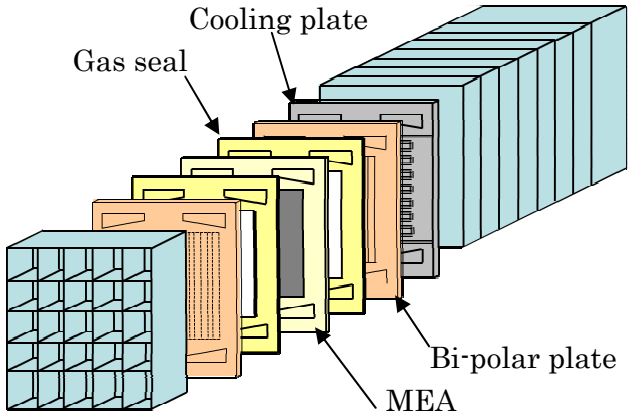

Fig.1.5 An example of cell stack configuration

1.4 Characteristics of HT-PEMFC

1.4.1 Operation regions of HT-PEMFC

Fig.1.6 shows conceptually the operation regions of both the PEMFCs for automobile use and for residential uses in relation between the power density range and the cell operation temperature range [79]. As shown in the figure, the PEMFC for automobile use is operated in the wide cell temperature range from -40℃ up to 120℃ to suit the environmental temperature and in the wide power density range from the low loads such as

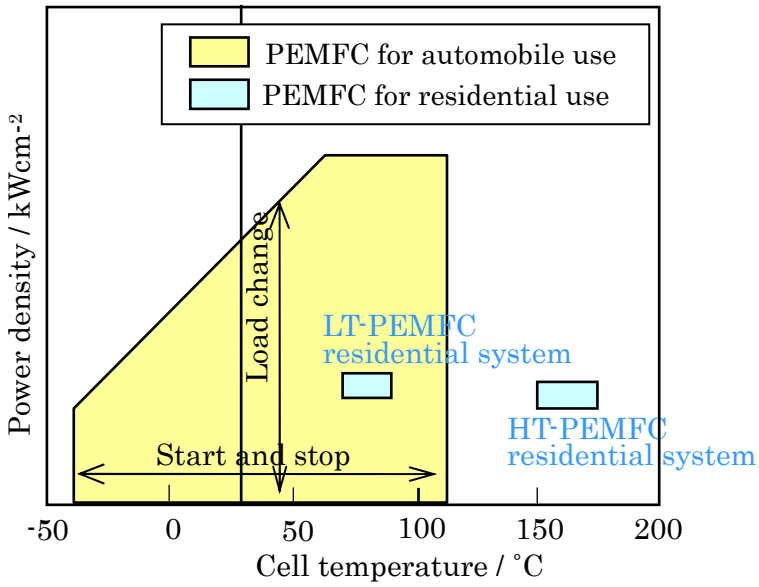

Fig.1.6 Operation regions of the LT-PEMFC for automobile use and both the LT-PEMFC and HT-PEMFC for residential uses.

a light-stop to the high loads such as upslope. On the other hand, the PEMFC for residential use is operated at a power density of almost constant except for the DSS operation, by using power systems [80]. Two types of residential systems with LT-PEMFC and HT-PEMFC are shown in the figure. LT-PEMFC is incorporated with perfluorosulfonic acid polymer membrane and is operated in a temperature range of 70 to 80℃. HT-PEMFC is incorporated with an electrolyte membrane such as phosphoric acid-doped PBI membrane and is operated in a temperature range of 150 to 170℃.

Fig.1.7 shows the operating ranges of LT-PEMFC and HT-PEMFC which are obtained by taking the amount of vapor contained in both the fuel and oxidant as a vertical axis and taking the cell temperature as a horizontal axis. As shown in the figure, at the gas outlet of LT-PEMFC, the vapor in fuel and oxidant is generally included almost up to the saturated vapor pressure with fuel and oxidant humidification vapor, fuel reformation steam and water produced by electrode reaction being accumulated. On the other hand, at the gas outlet of HT-PEMFC, the vapor in fuel and oxidant is originated only from the fuel reformation steam and water produced by electrode reaction. However, in case of HT-PEMFC, the cell operating temperature is 150 to 170℃ and consequently dry state is kept allover its inside.

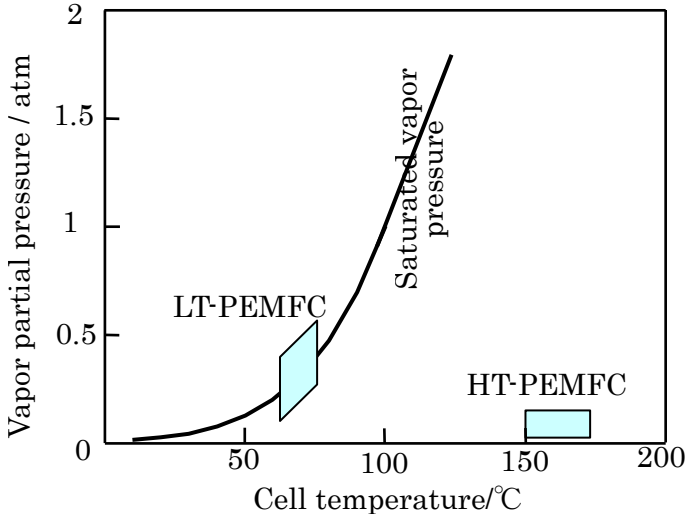

Fig.1.7 Humidity in the cell of LT-PEMFC and HT-PEMFC

The proton conductivity of the PBI-H_3PO_4 membranes depends on the phosphoric acid doping level, relative humidity, and temperature [53,81]. Even though the proton conductivity of the PBI-H_3PO_4 membrane increases with increasing relative humidity, the dependence is much weaker than that of Nafion [82].

1.4.2 System of HT-PEMFC

Fig.1.8 shows a conceptual diagram of a system for household cogeneration with a LT-PEMFC. In the LT-PEMFC with the electrolyte membrane of perfluorosulfonic acid-based polymer film, protons move from

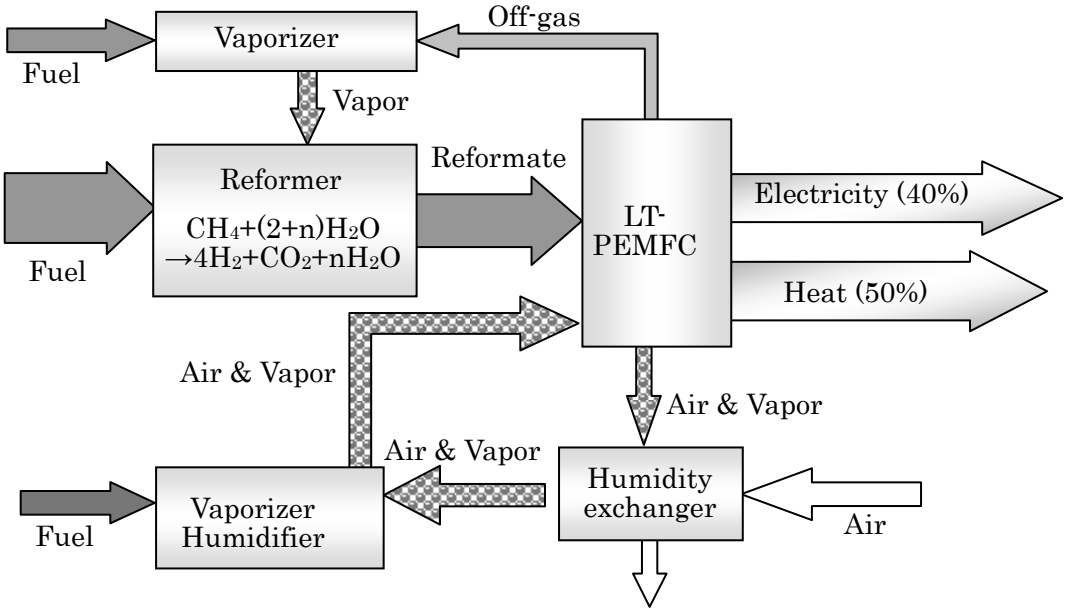

Fig.1.8 A conceptual diagram of household cogeneration system with LT-PEMFC which is operated in the temperature range from 70 to 80℃.

anode side to cathode side together with drag water and the polymer shows high proton conductivity only when electrolyte membrane and catalyst layers are in sufficient wet state. Therefore, it is necessary to humidify sufficiently ionomer in the catalyst layer and the electrolyte membrane [83-85]. For such a humidification, the systems to collect liquid water and to return again produced water to the cells are required [86], which hinders the high reliability and the cost reduction of the system.

Fig.1.9 shows a conceptual diagram of a system for household cogeneration with a HT-PEMFC with the electrolyte membrane such as PBI membranes doped with phosphoric acid. As shown in the figure, the system to humidify the electrolyte membrane is not necessary. Since HT-PEMFC is operated in a temperature range of 150 to 170℃, the steam required for reforming reaction ($CH_4+(2+n)H_2O \rightarrow 4H_2+CO_2+nH_2O$) can be covered by the vapor contained in the exhausted steam. Therefore, it is possible that the system operation is not only simplified, but also the steam of 140 to 160℃ can be taken out with waste heat from the cell, thereby, fuel is not consumed to generate the steam for the reforming reaction unlike LT-PEMFC.

Therefore, even if cell voltage of HT-PEMFC is lower than that of LT-PEMFC, its power generation efficiency can exceed that of LT-PEMFC.

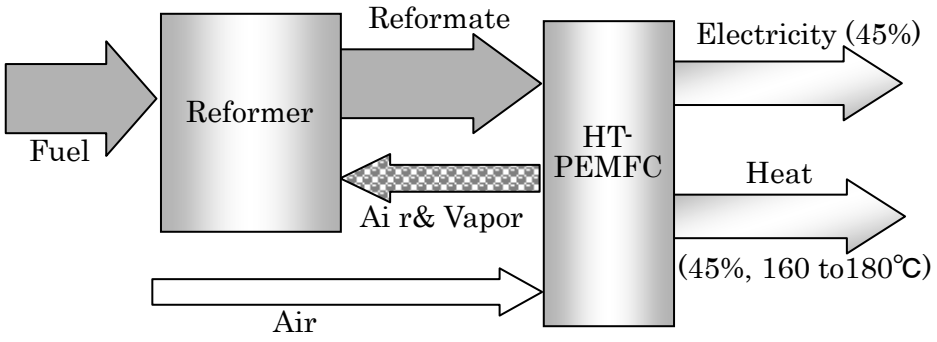

Fig.1.9 A conceptual diagram of household cogeneration system with HT-PEMFC which is operated in the temperature range from 150 to 170℃.

1.4.3 Electric efficiency of HT-PEMFC

High power generation efficiency and high thermal efficiency are desired for the household fuel cell cogeneration system. Especially, the electric efficiency over 45% is desired. High electric efficiency is achieved by both the high cell voltage and high fuel utilization. Fig.1.10 shows the influence of cell voltages and fuel utilizations on system electric efficiencies. In order to heighten the cell voltage, three over-voltages of activation, resistance and concentration are required to be reduced.

On the other hand, in order to heighten the fuel utilization, high gas sealing properties should be maintained, and the steam required for reforming reaction ($CH_4+(2+n)H_2O \rightarrow 4H_2+CO_2+nH_2O$) should be covered by the vapor generated using the heat exhausted by the electrode reaction. The operation temperature of LT- PEMFC is too low to use its exhausted heat as the steam for the above reforming reaction. In the case of SOFC consisting of ceramics, a suitable gas sealing method has not yet been found. In contrast, in the case of HT-PEMFC, although its cell voltage is not so high, its gas seal material can be easily found due to its operation temperature of 150 to 170℃ and its operation temperature is enough high to generate the steam for reforming reaction by the heat exhausted from the electrode reaction. Thus, HT-PEMFC is expected to achieve a high electric efficiency over 45 %.

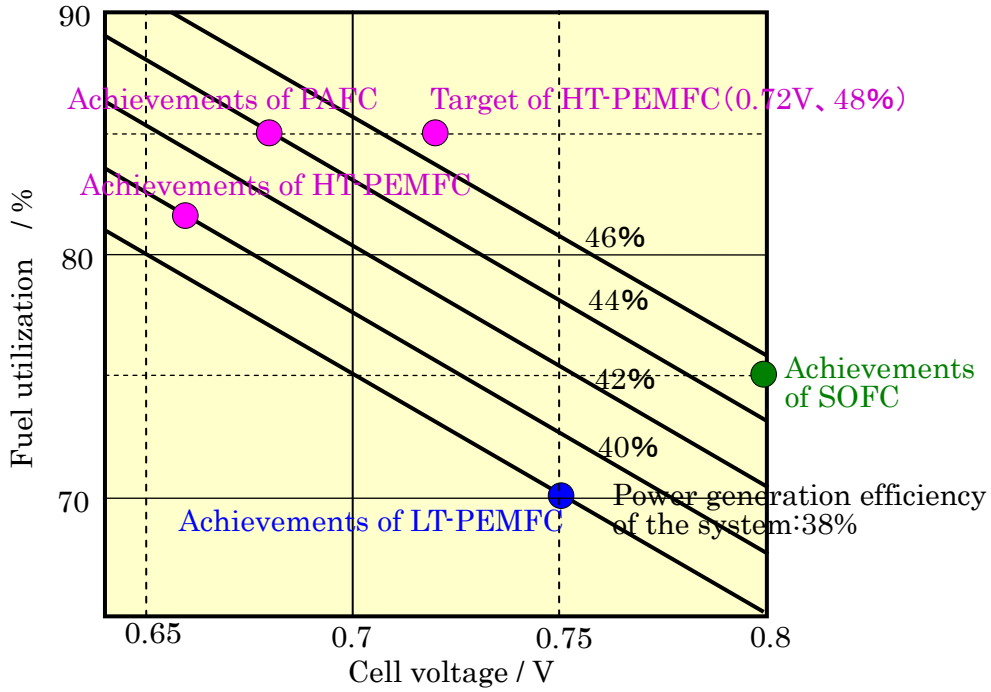

Fig.1.10 Relationship of fuel utilization and cell voltage on the system power generation efficiency

1.4.4 Characteristics of HT-PEMFC

Table 1.1 shows the comparisons of the specifications, operations and characteristics among LT-PEMFC, HT-PEMFC and PAFC. As shown in the table, the electrolyte membrane of LT-PEMFC consists of perfluorosulfonic acid-based polymer and that of HT-PEMFC consists of a polymer film such as PBI doped with phosphoric acid. Comparing two types of PEMFC, HT-PEMFC is superior to LT-PEMFC in the tolerance of CO poisoning of the anode catalyst and in the electric efficiency. On the other hand, PAFC is operated in the same temperature range as HT-PEMFC. However, the carbon separator gas flow channels are machined and are heat-treated at a high temperature near 3,000 ℃ to ensure corrosion resistance against phosphoric acid, so this is refused the cost reduction of the PAFC, which has resulted in driving PAFC into a niche market. However, in recent years, progress in the development of press forming technology and metallic bipolar plate is remarkable, metallic bipolar plate is thought to be applicable to HT-PEMFC.

Table 1.1 Comparisons among LT-PEMFC, HT-PEMFC and PAFC

	Proton Exchange Membrane Fuel Cell (PEMFC)		Phosphoric Acid Fuel Cell (PAFC)
	LT- PEMFC	HT-PEMFC	
Electrolyte	Perfluorosulfonic acid-based polymer	Phosphoric acid-doped PBI polymer	SiC porous matrix Phosphoric acid aqueous solution
Humidification	With	Without	
Operation pressure	Ambient pressure		
Cell temperature	70 to 80 ℃	150 to 170 ℃	150 to 220 ℃
Electrode	Pt and/or its alloy		
Anti-CO poison	Tens ppm	A few percentages	
Bi-polar plate	Resin-carbon composite	Metal	Graphite carbon
Electric efficiency	40 %	45 %	43 %
Heat utilization	Hot water	Hot water, Steam, Air conditioner	

1.5 Issues of HT-PEMFC

1.5.1 Cell performance

HT-PEMFC requires cell voltages of over 0.7V to achieve higher system efficiencies than LT-PEMFC. However, its cell performance is currently still low compared with such a target. The reason why cell performance is not so high is thought to be that oxygen cannot diffuse to the catalyst sites at a sufficiently high rate, and consequently that the over-potential is not so low due to the reduction of oxygen at the cathode [67,87].

In order to hasten the diffusion rate of oxygen to the catalyst sites, a few methods have been tried. One of them was the method to replace the phosphoric acid as a proton carrier in a cathode with a thin polymer proton carrier such as the ionomer used for LT-PEMFC. In this case, it is expected that oxygen can be diffused at a sufficiently high rate through the thinner proton carrier by far than phosphoric acid, and that the oxygen carrier mechanism differ from that of the conventional phosphoric acid-doped PBI ionomer. However, a high performance cannot be achieved with this method [74].

Thus, in the HT-PEMFC, a higher cell performance is not only strongly desired, but also the factors which dominate the cell performance should be

identified and their impacts should be quantitatively estimated.

1.5.2 Improvement of durability

Many experimental[13,66,-69,75,88-91] and analytical[92-95] studies have been conducted on HT-PEMFC using a phosphoric acid-doped PBI membrane, which functions most efficiently in the temperature range 120–200℃[13], and several reports have described the endurance of these membranes [9,41,69,78]. Furthermore, PBI composites [48,51,57,96-99] have also been developed to improve the performance and/or stability of PBI membranes.

In previous studies, it was also reported that the size of Pt electrocatalyst particles grew during power generation in a relatively short period of approximately 500h at 150℃ [69-72,77,105]. Especially, Zhai showed that Pt aggregation occurred by increasing its size from 4.0 to 8.3nm in the early stage of power generation during the first about 300 h [72], and increasing its size from 4.02 to 8.88nm during 550h [69] at 150℃. Hu and Liu also reported the Pt agglomeration from 3.8nm to 6.9nm during 500h [70,105] and from 3.72nm to 8.39nm during 600h at 150℃[71].

On the other hand, there is a dilemma in that raising the operating temperature in order to increase the cell voltage and improve the efficiency makes it difficult to sustain long-term durability. Conversely lowering the temperature improves the durability but leads to lower cell voltages. To date, only a few reports have dealt with the relationship between the operating temperature and the cell durability, including the deterioration mechanism during approximately 500h operation at 150℃[9,93-95].

As above-mentioned, in the field of HT-PEMFC, there has been almost no study to verify the durability over 10,000hr. Of course, the factors which dominate the cell voltage drop have not been identified by now. Therefore, it is very important for the commercialization of HT-PEMFC to verify the long term durability over at least 20,000h, to identify the factors which dominate the cell voltage drop and to clarify the cell degradation mechanism.

1.5.3 Analytical Estimation of durability

PEMFC is required to operate for over 5000h for vehicular and 40,000 to 90,000h for stationary cogeneration systems. It takes a lot of time to evaluate experimentally the irreversible deterioration phenomena such as a thinning or a decomposition of electrolyte membranes and a sintering of

electrocatalysts. In order to save the numbers and time of cell endurance test, theoretical evaluation schemes have been presented by now.

For example, numerical 1D non-isothermal models [92,93,100], 2D steady-state isothermal and transient non-isothermal models [101-103], and 3D steady and unsteady state models [94,95,103,104] for HT-PEMFCs have been proposed. However, the main problem with all of these models is the assumption that proton conductivity is constant, which has shown to vary with both relative humidity and temperature [92, 93, 104]. While the previous HT-PEMFCs models have been helpful to understand the effects of various operating conditions such as temperature and pressure on cell performance, none have focused on predicting theoretically the deterioration mechanisms. Through them the morphological properties of the aging CL where Pt sintering or phosphoric acid loss can be seen, which has the possibility of great impact on the gradual progress of oxygen reduction reactions (ORR) and gradual cell performance over time.

The other methodology is dealing with small areas by the ab-initio method which forces one to develop a model composed of a few numbers of atoms due to the high computational demand. Temperature is hard to consider in the ab-initio computation method, and the static Monte Carlo method lacks of the factor of time. Nevertheless, both are indispensable factors to discuss the phenomena of durability.

Thus, by now, although it takes a lot of time to evaluate experimentally the irreversible deterioration phenomena of HT-PEMFC as well as LT-PEMFC, any analytical approaches have not effectively used to estimate the cell durability of HT-PEMFC. Therefore, the effective analytical approaches are expected to use for supporting the experimental approaches.

1.6 Purpose and composition of this thesis

1.6.1 Purpose of this thesis

HT-PEMFC has been actively developed as a next generation PEMFC, in order to solve the problems of LT-PEMFC by simplification of the system, reduction of production costs, and improvement of the operational efficiency in the temperature range of around 150℃. It is said that one of the most promising candidates of the electrolyte membranes for HT-PEMFC is the phosphoric acid-doped PBI-based polymer membrane (PBI-H_3PO_4). HT-PEMFCs do not require large shift converters or selective oxidizers due

to their high CO tolerance, which exceeds 10,000ppm. Neither do they require humidifiers, because proton transport in the PEM occurs without water dragging. They can also be used without vaporizers for supplying steam to a fuel reformer, because the vapor produced by electrode-reaction thermal heat is recirculated.

On the other hand, in spite of many attractive characteristics of HT-PEMFCs, their cell performances are currently lower than the expected ones. Thus, higher cell performances are not only strongly desired, but also the factors which dominate the cell performances should be identified and their impacts should be quantitatively estimated. In addition, regarding the durability of HT-PEMFC, there has been almost no study to achieve the durability over 10,000hr. Of course, the factors which dominate the cell voltage drops have not been identified by now.

Under such a situation, this thesis aims at verifying the long-term durability of HT-PEMFCs over at least 20,000h, identifying the factors which dominate their cell voltage drops and at clarifying their cell degradation mechanism.

1.6.2 Composition of this thesis

The text of this thesis consists of five chapters, Chapter 2, Chapter 3, Chapter 4, Chapter 5 and Chapter 6, as follows;

In the chapter 2, the cell tests was conducted on cells of HT-PEMFC with the phosphoric acid-doped membrane (PBI-H_3PO_4) of various doping levels, in order to search for an optimum acid-doping level and doping condition. Furthermore, attempts were made to clarify the mechanism for the migration of phosphoric acid from the PBI-H_3PO_4 membrane to the electrodes during cell operation and to clarify how this influences cell performance.

In the chapter 3, the effects of temperature on the cell voltage and durability were evaluated by conducting long-term durability tests on cells with PBI-H_3PO_4 and newly developed electrodes at cell temperatures of 150, 170, and 190℃. The deterioration mechanism of the cells was investigated based on the results of time variations of cell voltage, internal cell resistance and impedance during the durability tests, in addition to post-analysis by transmission electron microscopy (TEM) observations.

In the chapter 4, the effects of temperature on sintering of nanoparticles

of electrocatalysts, cell voltage, and durability were theoretically evaluated by executing long-term durability simulation of the HT-PEMFC. Simulated results were compared with the measured results of experimental durability tests of HT-PEMFC using PBI-H_3PO_4 membranes at cell temperatures of 150˚C, 170˚C, and 190˚C in the chapter 3. The deterioration mechanism of the cells was also theoretically investigated based on the time variations of cell voltage and internal cell resistance during the durability tests, and was confirmed by post analysis TEM observations.

In the chapter 5, in order to clarify the causes of long-term cell deterioration, five identical cells with PBI-H_3PO_4 were tested for periods of up to 17,860h, and their MEAs were then removed and subjected to microstructural analysis. The deterioration mechanism was investigated based on chronological changes in the cell voltage and internal cell resistance, chronocoulometry (CC) measurements of the hydrogen crossover, and post-analysis using transmission electron microscopy (TEM) and electron probe micro-analysis (EPMA).

In the chapter 6, in order clarify whether the stability of electrolyte membrane is the main factor influencing cell deterioration, power generation tests were carried out on two cells with the cross-linked ABPBI-H_3PO_4 for operation times of 1,000 and 17,500h. The MEAs removed from the cells were observed using EPMA. In order to clarify the effect of the membrane on cell deterioration, the EPMA results were compared between the MEA with ABPBI- H_3PO_4 membrane cell-tested for 17,500h and that with PBI membrane cell-tested for 17,800h in the chapter 5.

Reference

[1] K. Endo ; Proceedings of the 4th International Hydrogen & Fuel Cell Expo, Keynote(2008) 27.

[2] T. Omata ; J. Fuel Cell Technol. 7 (2) (2007) 6.

[3] M. Hiwatari ;J. Fuel Cell Technol. 7 (2) (2007) 11.

[4] H. Yamada ; J. Fuel Cell Technol. 7 (2) (2007) 24.

[5] M. Ochi ; J. Fuel Cell Technol. 7 (2) (2007) 29.

[6] A. Matsui, M. Kawai, Y. Kimura, H. Tachi ; J. Fuel Cell Technol. 7 (2) (2007) 33.

[7] M. Kawahara ; 5th Int'l Hydrogen & Fuel Cell Expo Keynote (2009) 17.

[8] T. Shimizu ; 7th Int'l Hydrogen & Fuel Cell Expo, FC-4 (2011) 18.

[9] J. Baurmeister, T. Kohno ; Proceedings of the 13th Fuel Cell FCDIC Symposium (2006) 122.

[10] P. Krishnan, J.S. Park, C.S. Kim ; J. Power Sources 159 (2006) 817.

[11] H. Xu, Y. Song, H.R. Kunz, J.M. Fenton ; J. Power Sources 159 (2006) 979.

[12] C.P. Wang, H.S. Chu, Y.Y. Yan, K.L. Hsueh ; J. Power Sources 170 (2007) 235.

[13] J. Zhang, Y. Tang, C. Song, J. Zhang ; J. Power Sources 172 (2007) 163.

[14] J. Karstedt, J. Ogrzewalla, C. Severin, S. Pischinger ; J. Power Sources 196 (2011) 9998.

[15] Q. Li, R. He, J.O. Jensen, N.J. Bjerrum ; Chem. Mater. 15 (2003) 4896.

[16] M. Kawahara, J. Morita, M. Rikukawa, K. Sanui, N. Ogata ; Electrochim. Acta 45 (2000) 3045.

[17] R. He, Q. Li, G. Xiao, N.J. Bjerrum ; J. Membr. Sci. 226 (2003) 169.

[18] Q. Li, R. He, J.O. Jensen, N.J. Bjerrum ; Fuel Cells Fundam. Syst. 4 (2004) 147.

[19] P. Staiti, F. Lufrano, A.S. Arico, E. Passalacqua, V. Antonucci ; J. Membr. Sci. 188 (2001) 71.

[20] P. Staiti, M. Minutoli ; J. Power Sources 94 (2001) 9.

[21] D. Plackett, A. Siu, Q. Li, C. Pan, C. Pan, J.O. Jensen, S.F.Nielson, A.A. Permyakova, N.J. Bjerrum ; J. Membr. Sci. 383 (2011) 78.

[22] J. Lobato, P. Canizares, M.A. Rodrigo, D. Ubeda, F.J. Pinar ; J. Membr. Sci. 369 (2011)105.

[23] J. Hu, J. Luo, P. Wagner, O. Conrad, C. Agert ; Electrochem. Commun. 11 (2009) 2324.

[24] R. Bouchet, E. Siebert ; Solid State Ionics 118 (1999) 287.
[25] X. Glipa, B. Bonnet, B.B. Mula, D.J. Jones, J. Roziere ; J. Mater. Chem. 9 (1999) 3045.
[26] H. Pu, W.H. Meyer, G. Wegner ; J. Polym. Sci. B: Polym. Phys. 40 (2002) 663.
[27] B. Xing, O. Savadogo ; Electrochem. Commun. 2 (2000) 697.
[28] P. Donoso, W. Gorecki, C. Berthier, F. Defendini, C. Poinsignon, M. Armand ; Solid State Ionics 28–30 (1988) 969.
[29] S.P. Weeks, J.J. Zupancic, J.R. Swedo ; Solid State Ionics 31 (1988) 117.
[30] M.A. Vargas, R.A. Vargas, B.E. Mellander ; Electrochim. Acta 44 (1999) 4227.
[31] M.S. Boroglu, S.U. Celik, A. Bozkurt, I. Boz ; J. Membr. Sci. 375 (2011) 157.
[32] S. Zeng, L. Ye, S. Yan, G. Wu, Y. Xiong, W. Xu ; J. Membr. Sci. 367 (2011) 78.
[33] J.C. Lassegues, B. Desbat, O. Trinquet, F. Cruege, C. Poinsignon ; Solid State Ionics 35 (1989) 17.
[34] D. Rogriguez, C. Jegat, O. Trinquet, J. Grondin, J.C. Lassegues ; Solid State Ionics 61 (1993) 195.
[35] M.F. Daniel, B. Desbat, F. Cruege, O. Trinquet, J.C. Lassegues ; Solid State Ionics 28–30 (1988) 637.
[36] Y.L. Ma, J.S. Wainright, M.H. Litt, R.F. Savinell ; J. Electrochem. Soc. 151 (2004) A8.
[37] Q.Li, R.He, R.W.Berg, H.A.Hjuler, N.Bjerrum ; Solid State Ionics 168 (2004) 177.
[38] A.J.Appleby ; J. Power Sources 58 (1996) 153.
[39] Watanabe, M.Matsumoto, K.Takasu ; J. Power Sources 61 (1996) 53.
[40] H.Y. Kwak, H.S. Lee, J.Y. Jung, J.S. Jeon, D.R. Park ; Fuel (Guildford) 83 (2004) 2087.
[41] A. Sounai, J. Baurmeister, T.J. Schmidt, M. Hori, J. Fuel Cell Technol. 7 (2) (2007) 86.
[42] J.S.Wainright, J.T.Wang, D.Weng, R.F.Savinell, M.Litt ; J.Electrochem. Soc. 142 (1995) L121.
[43] Q. Li, J.O. Jensen, R.F. Savinell, N.J. Bjerrum ; Prog. Polym. Sci. 34 (2), (2009) 449.
[44] M.Litt, R.Ameri, Y.Wang, R.F.Savinell, J.Wainwright ; Mater. Res. Soc. Symp. Proc. 548 (1999) 313.

[45] R.H.He, Q.F.Li, A.Bach, J.O.Jensen, N.J.Bjerrum ; J. Membr. Sci.277 (2006) 38.
[46] S.R.Samms, S.Wasmus, R.F.Savinell ; J. Electrochem. Soc. 143 (1996) 1225.
[47] A. Sannigrahi, D.Arunbabu, R.M.Sankar, T.Jana ; J. Phys. Chem. 111B (2007) 12124.
[48] T.H.Kim, T.W.Lim, J.C.Lee ; J. Power Sources 172 (2007) 172.
[49] L.X.Xiao, H.F.Zhang, E.Scanlon, L.S.Ramanathan, E.W.Choe, D.Rogers, T.Apple, B.C.Benicewicz ; Chem. Mater. 17 (2005) 5328.
[50] L.X.Xiao, H.F.Zhang, T.Jana, E.Scanlon, R.Chen, E.W.Choe, L.S.Ramanathan, S.Yu, B.C.Benicewicz ; Fuel Cells 5 (2005) 287.
[51] A.Carollo, E.Quatarone, C.Tomasi, P.Mustarelli, F.Belotti, A.Magistris, F.Maestroni, M.Parachini, L.Garlaschelli, P.P.Righetti ; J.Power Sources 160 (2006) 175.
[52] J.S.Wainright, M.H.Litt, R.F.Savinell, W.Vielstichm, A.Lamm, H.A.Gasteiger ; Handbook of Fuel Cells, Vol.3, John Wiley & Sons Ltd. (2003) 436.
[53] J.A. Asensio, S. Borros, P.G. Romero ; J Electrochem Soc 151(2) (2004) A304.
[54] S.B.Qing, W.Huang, D.Y.Yan ; Eur.Polym.J.41 (2005) 1589.
[55] S.Yu, L.Xiao, B.C.Benicewicz ; Fuel Cells 8 (2008) 165.
[56] S.W.Chuang, S.L.C.Hsu ; J.Polym. Sci. 44 (2006) 4508.
[57] S.W.Chuang, S.L.C.Hsu, C.L.Hsu ; J.Power Sources 168 (2007) 172.
[58] J.M.Bae, I.Honma, M.Murata, T. Yamamoto, M.Rikukawa, N.Ogata ; Solid State Ionics 147 (2002) 189.
[59] F.Schönberger, A.Chromik, J.Kerres, M.Hein, Th.Häring, Q.F.Li, J.O.Jensen, P.Noyē, N.J.Bjerrum ; Fuel Cells 8 (2008) 175.
[60] Q.F.Li, J.O.Jensen, C.Pan, V.Bandur, M.Nilsson, F.Schönberger, A.Chromik, J.Kerres, M.Hein, Th. Th, N.J.Bjerrum ; Fuel Cells 8 (2008) 188.
[61] P.Noyē, Q.F.Li, C.Pan, N.J.Bjerrum ; Polym. Adv. Technol. 19 (2008) 1270.
[62] Q.F.Li, C.Pan, J.O.Jensen, P.Noyē, N.J.Bjerrum ; Mater. Chem. 19 (2007) 350.
[63] Q.F.Li, R.H.He, J.O.Jensen, N.J.Bjerrum ; Fuel Cells 4 (2004) 147.
[64] Q.F.Li, J.O.Jensen, R.F.Savinell, N.J.Bjerrum ; Prog. Polym. Sci. 34 (2009) 449.

[65] J.A. Asensio, S. Borros, P.G. Romero ; J. Electrochem. Soc. 151 (2004) A304.
[66] J.R.P. Jayakody, S.H. Chung, L. Durantio, H. Zhang, L. Xiao, B.C. Benicewicz, S.G.Greenbaum ; J. Electrochem. Soc. 154 (2007) B242.
[67] N.H. Jalani, M. Ramani, K. Ohlsson, S. Buelte, G. Pacifico, R. Pollard, R. Staudt, R.Datta ; J. Power Sources 160 (2006) 1096.
[68] Z. Qi, S. Buelte ; J. Power Sources 161 (2006) 1126.
[69] Y. Zhai, H. Zhang, G. Liu, J. Hu, B. Yi ; J. Electrochem. Soc. 154 (2007) B72.
[70] J. Hu, H. Zhang, G. Liu, B. Yi ; Hydrogen Energy 31 (2006) 1855.
[71] G. Liu, H. Zhang, J. Hu, Y. Zhai, D. Xu, Z. Shao ; J. Power Sources 162 (2006) 547.
[72] Y. Zhai, H. Zhang, D. Xing, Z.G. Shao ; J. Power Sources 164 (2007) 126.
[73] J. Lobato, P. Canizares, M.A. Rodrigo, J.J. Linares ; Electrochim. Acta 52-2 (2007) 3910.
[74] J.H. Kim, H.J. Kim, T.H. Lim, H.I. Lee ; J. Power Sources 170 (2007) 275.
[75] C. Pan, Q. Li, J.O. Jensen, R. Je, L.N. Cleemann, M.S. Nilsson, N.J. Bjerrum, Q. Zeng ; J. Power Sources 172 (2007) 278.
[76] J. Parrondo, F. Mijangos, B. Rambabu ; J. Power Sources 195 (2010) 3977.
[77] J. Lobato, P. Canizares, M.A. Rodrigo, D. Ubeda, F.J. Pinar ; J. Power Sources 196 (2011), 8265.
[78] A. Sounai, K. Sakai ; Proceedings of the 13th Fuel Cell FCDIC Symposium (2006) 125.
[79] H.Nakayama, T.Minamide, M.Hori, Y.Sakiyama, Y.Aoki, K.Okubo, H.Katagiri; Proceedings of the 14th Fuel Cell FCDIC Symposium (2007) 101.
[80] K.Nishizaki, M.Kawamura, N.Osaka , K.Ito , N.Fujiwara , Y.Nishizaka , H.Kitazawa ; Fuel Cell Seminar (2005)
[81] J. Zhang, Z. Xiea, J. Zhanga, Y. Tanga, C. Songa, T. Navessina,et al ; J. Power Sources 160 (2006) 872.
[82] Q. Li, R. He, J.O. Jensen, N.J. Bjerrum ; Fuel Cells 4(3) (2004) 147.
[83] Y.Hiramitsu, H.Sato, K.Kobayashi, M.Hori ; J Power Source 196 (13) (2011) 5453.
[84] Y.Hiramitsu, K.Kobayashi, M.Hori ; J Power Source 195 (22) (2010) 7559.

[85] Y.Hiramitsu, Y.Hayashi, K.Kobayashi, M.Hori; Electrical Eng. in Japan 169 (3) (2009) 10.
[86] S.Motomori, K.Nakayama, S.Sekiguchi, H.Takahashi ; 14th Fuel Cell FCDIC Symposium (2006)
[87] Z. Liu, J.S.Wainright, M.H. Litt, R.F. Savinell ; Electrochim. Acta 51 (2006) 3914.
[88] I.M. Petrushina, V.A. Bandur, N.J. Bjerrum, F. Cappeln, L. Qingfeng ; J. Electrochem. Soc. 149 (2002) D143.
[89] J. Lobato, M.A. Rodrigo, J.J. Linares, K. Scott ; J. Power Sources 157 (2006) 284.
[90] A.R. Korsgaard, R. Refshauge, M.P. Nielsen, M. Bang, S.K. Kaer ; J. Power Sources 162 (2006) 239.
[91] K.C. Neyerlin, A. Singh, D. Chu ; J. Power Sources 176 (2008) 112.
[92] D.Cheddie, N. Munroe ; J. Power Sources 156 (2006) 414.
[93] D.Cheddie, N. Munroe ; J. Power Sources 160 (2006) 215.
[94] J. Peng, S.J. Lee ; J. Power Sources 162 (2006) 1182.
[95] J. Peng, J.Y. Shin, T.W. Song ; J. Power Sources 179 (2008) 220.
[96] P. Staiti, M. Minutoli, S. Hocevar ; J. Power Sources 90 (2000) 231.
[97] C. Hasiotis, L. Qingfeng, V. Deimede, J.K. Kallitsis, C.G. Kontoyannis, N.J. Bjerrum ; J. Electrochem. Soc. 148 (5) (2001) A513.
[98] M.Y. Jang, Y. Yamazaki ; J. Power Sources 139 (2005) 2.
[99] Y. Zhai, H. Zhang, Y. Zhang, D. Xing ; J. Power Sources 169 (2007) 259.
[100] D.Cheddie, N.Munroe ; Energy Convers Manage 47 (2006) 1490.
[101] T.Sousa, M.Mamlouk, K.Scott ; Chem. Eng. Sci. 65 (2010) 2513.
[102] T.Sousa, M.Mamlouk, K.Scott ; Int J. Hydrogen Energy 35 (2010) 12065.
[103] K.Jiao, X.Li ; Fuel Cells 10 (2010) 351.
[104] E.U. Ubong, Z.Shi, X.Wang ; J Electrochem.Soc. 156 (2009) B1276.
[105] J.Hu, H.Zhang, Y.Zhai, G.Liu, J.Hu, B.Yi ; Electrochim. Acta 52 (2) (2006) 394.

Chapter 2

Influence of the phosphoric acid-doping level in a polybenz imidazole membrane on the cell performance of HT-PEMFC

2.1 Introduction

HT-PEMFC requires cell voltages of over 0.7V to achieve higher system efficiencies than LT-PEMFC; however, their cell performance is currently still low compared with such a target. The reason for their low performance is thought to be that oxygen cannot diffuse to the catalyst sites at a sufficiently high rate, and the resulting overpotential loss is quite high for the reduction of oxygen at the cathode [1, 2]. In order to realize high efficiency HT-PEMFC residential systems, the author has been developing PBI/phosphoric acid HT-PEMFC that can achieve high cell voltages. To reduce the over potential at the cathode and to achieve a high cell voltage, it has been proposed that phosphoric acid as a proton carrier in the cathode side be reduced, and that instead of using only phosphoric acid, a thin polymer proton carrier, such as the ionomer used for LT-PEMFC, be dispersed in the cathode catalyst. Oxygen should then be diffused at a sufficiently high rate through the thin proton carrier, and the oxygen carrier mechanism should differ from that of the conventional phosphoric acid-doped PBI ionomer, which cannot achieve high performance [3].

In this chapter, as the first stage of this investigation, an attempt was made to clarify the mechanism for the migration of phosphoric acid doped in the PBI membrane from the membrane to the electrodes during cell operation and to clarify how this influences cell performance. Ex-situ tests were conducted to ascertain the relationship between the change in doping level with the temperature of the acid solution and the time in which the PBI membranes were immersed during doping. PBI membranes with various phosphoric acid-doping levels were prepared and power generation tests were conducted on cells using membranes with several acid-doping levels. One doping method involves prior doping of the acid in both the membrane and catalyst layers; however, the method adopted in this study was to dope all the phosphoric acid in the membrane, because the author has more extensive experience with this method [4].

AC impedance spectroscopy was used to clarify the effect of acid doping level on cell performance. This technique has been used to provide

information on the three main processes that limit cell performance: charge transfer, mass transport and ohmic resistance in single cells [5–7], LT-PEMFC stacks [8, 9], HT-PEMFC [10] and PAFC [11]. The cells were disassembled after the cell operation tests had been completed, and the weights and dimensions of the membranes were measured after removing the electrodes, in order to assess the phosphoric acid migration in the cells.

2.2 Experimental

2.2.1 Acid-doping level ex situ test survey

Three PBI membranes with areas of 3cm×3cm and thick nesses of approximately 40 μm were supplied by a collaborative organization, and their weights and dimensions were measured with a high-precision balance (AUW120D, Shimadzu Corp., Japan) and micrometer, respectively. The three membranes were then immersed in an 85% phosphoric acid solution: one membrane at 20℃ for approximately 500 min, another at 40℃ and the other at 60℃ for 80 min. In order to avoid acid condensation due to evaporation during heating, the phosphoric acid was kept in a covered container in a water bath at the given temperature. The membranes were removed from the container at intervals, the surfaces wiped, and their weights and dimensions measured. In this study, the acid-doping level was defined as the percentage ratio of membrane weight increment from the membrane weight prior to doping to the weight of the acid-containing membrane after doping.

2.2.2 PBI membrane preparation

PBI membranes with different acid-doping levels of 65%, 71%, 75% and 78% were prepared for single cells and used to evaluate the influence of acid-doping level on cell performance. In order to achieve the target acid-doping levels, PBI membranes with active areas of 5cm×5cm and thicknesses of approximately 40 μm were immersed in 85% phosphoric acid solution at 20, 40 or 60℃ for times ascertained from the acid-doping level ex-situ test survey. Their weights and dimensions were measured before and after doping.

2.2.3 Electrode preparation

Carbon paper (TGP-H-090, Toray Corp., Japan) was employed as the gas

diffusion layer (GDL). For wet proofing, the carbon paper was immersed in a 12wt% polytetrafluoroethylene (PTFE; DuPont) dispersion for a few minutes and dried at 80℃ in an atmospheric oven for 15min. A micro porous layer (MPL), which consisted of Ketjenblack carbon (EC-600JD, Akzo Nobel Corp., UK) and PTFE powder (DuPont) as a binder (weight ratio of 65:35),was deposited (2mg cm^{-2}) on the surface of the wet-proofed carbon paper using a dry-deposition facility [12]. The carbon paper with a MPL was sintered at a temperature of 350℃ in an atmospheric furnace for 15 min to melt the PTFE binder, and it was then rolled to flatness [12]. Catalyst ink was prepared by the addition of polyvinylidene fluoride (PVDF; Kureha Corp., Japan) and N-methyl-2-pyrrolidone (NMP; Sigma–Aldrich Corp., USA) to a Pt–Co/C catalyst powder (Pt + Co : C weight ratio of 50 : 50, TKK Corp., Japan) [13]. After magnetically stirring (PSH-4A, As One Corp., Japan) the catalyst ink for 60 h, it was evenly spread on the MPL-deposited carbon paper using an adjustable doctor blade (MHAI-13, Mitutoyo Corp., Japan). The electrode was dried at a temperature of 80℃ in an atmospheric oven for 1 h and was kept at 160℃ in a vacuum furnace for 25 h to degas the NMP solvent from the electrode. The average thickness of the catalyst layer (CL) was 20 μm and the Pt loading of the electrode was approximately 0.7mgcm^{-2}. The same electrode was used for both the anode and cathode. An electron probe micro analyzer (EPMA; EPMA-1610, Shimadzu, Japan) was employed to observe the cross-section of the electrode consisting of a GDL, a MPL and a CL.

2.2.4 Single cell assembly

The acid-doped PBI membrane and the electrodes were sandwiched together using a cell holder (JARI, Japan) to form a membrane electrode assembly (MEA). The cell holder was composed of a pair of graphite plates, which functioned as current collectors, and two stainless-steel end plates. The graphite plates have an active area of 25 cm^2 with machined serpentine flow channels. Two end plates with heaters attached and eight screw bolts were used to clamp the MEA together with the graphite plates.

2.2.5 Single cell test

The single cells were installed in fuel cell test stands (Kofloc Corp., Japan) equipped with reactant mass flow-controllers, an electronic load (Kikusui Electronics Corp., Japan) for controlling the electric current, an AC

milliohm tester (Model-3566, Tsuruga Electric Corp., Japan) with a constant frequency of 1 kHz, and a personal computer for equipment monitoring and data output. The cells were operated at 150℃ under a 0.1MPa atmosphere of pure hydrogen and air without humidification for 450 h. The flow rates of hydrogen and air were 130mLmin^{-1} (stoich: 3.7) and 310mLmin^{-1} (stoich: 3.7), respectively. A potentiostat-galvanostat (HZ-5000 HAG-3001, Hokuto Denko Corp., Japan) was used for chronocoulometry (CC) measurements of the hydrogen crossover rate through the PBI membrane [14]. During the measurement, single cells were operated at 150℃ with pure hydrogen at the anode and nitrogen at the cathode. Under these operation conditions, a voltage of 0.2V was applied across the cell, so that hydrogen crossing through the membrane was electrochemically oxidized. During the measurement of the hydrogen crossover rates of the cells, the hydrogen and nitrogen flow rates were controlled at 300 and 500mLmin^{-1}, respectively. Impedance spectra of single cells were measured at 150℃ by sweeping the frequency range 20,000-0.01Hz at cell operation times of 0, 50, 100, 150, 250 and 450 h using a frequency response analyzer (FRA 5020A, NF Corp., Japan) connected to a potentiostat-galvanostat (HZ-5000 HAG-3001, Hokuto Denko Corp., Japan) in constant-current mode at a DC current of 5A (0.2Acm^{-2}) and an AC amplitude of 0.5A. The flow rates of hydrogen and air during the measurements were the same as those used for the single cell tests.

2.2.6 Evaluation of acid migration

After approximately 450h of cell operation, all the cells were disassembled and both electrodes were scraped away from the membranes. The weights and dimensions of the membranes were then measured. The amount of phosphoric acid exhausted from the cells was evaluated by analyzing the concentration of phosphoric acid in the water exhausted from the cells using inductively coupled plasma mass spectroscopy (ICPMS; ICPM-8500, Shimadzu, Japan). Phosphoric acid migration in the cells was evaluated based on the weights and dimensions of the membranes before and after doping and after cell testing.

2.3. Results and discussion

2.3.1 Structural analysis of electrode

Fig.2.1 shows typical EPMA cross-sectional images of an electrode composed of GDLs, MPLs and CLs, observed before assembling the electrodes and membrane in a single cell. The thicknesses of the GDL, MPL and CL are 280, 30 and 20 μ m, respectively. Fig.2.1(a) and (b) indicates that platinum is limited to the CL, and that fluorine from PTFE is distributed in the GDL and MPL.

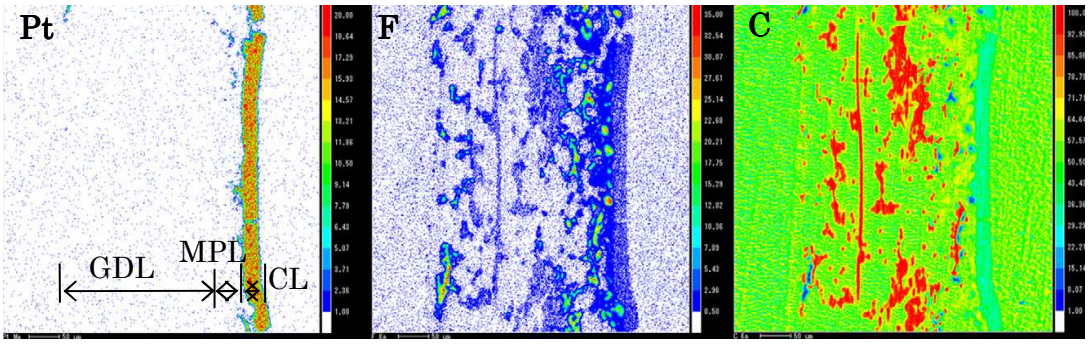

Fig.2.1 Typical EPMA cross-sectional images of the electrode composed of GDL, MPL and CL: (a) platinum, (b) fluorine, and (c) carbon images.

Fig.2.2(a) shows a cross-sectional SEM micrograph of the electrode indicating that the surface of the GDL is filled with the MPL, and Fig.2.2(b) shows the surface of the CL in contact with the membrane. During the initial period of cell operation, phosphoric acid migrates from the PBI membrane, through the interfaces, and into the porous CL shown in Fig. 2(b).

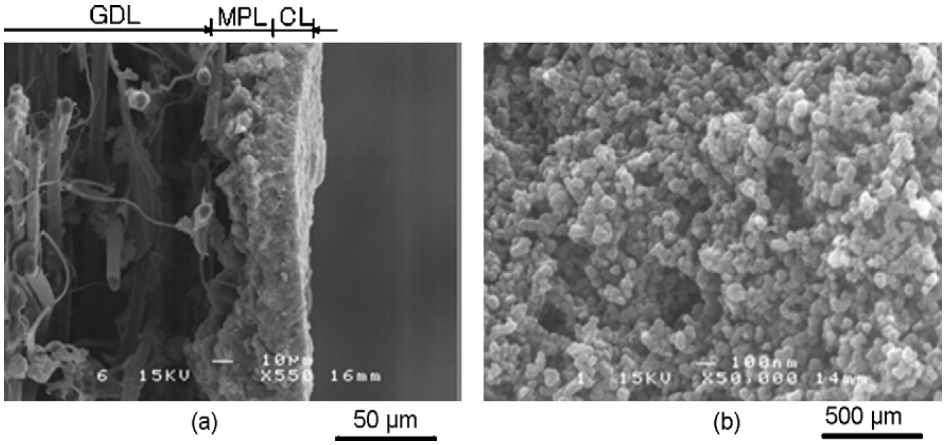

Fig.2.2 Typical SEM micrographs of the electrode: (a) cross-sectional micrograph of the electrode composed of a GDL, MPL and CL and (b) surface micrograph of the catalyst

2.3.2 Ex-situ test survey for acid-doping level

For preliminary evaluation of the influence of the acid-doping level of PBI membranes on cell voltage, the acid-doping level was experimentally verified as being controllable. Fig.2.3 shows the changes in the acid-doping level with time, obtained by immersing the PBI membranes (areas of 25 cm^2) in acid solutions at 20, 40 and 60℃. At 60℃, the acid was rapidly doped into the PBI membrane to the equilibrium level of 78%for an 85%phosphoric acid solution[4] over a period of less than 10min. On the other hand, at temperatures of 40 and 20℃, the acid was slowly doped into the PBI membranes up to the same equilibrium level, taking approximately 30 and 300min, respectively. Thus, higher acid temperatures resulted in amore rapid acid-doping rate. However, irrespective of the solution temperature, the PBI membranes eventually equilibrated at the same acid-doping level of approximately 78%.

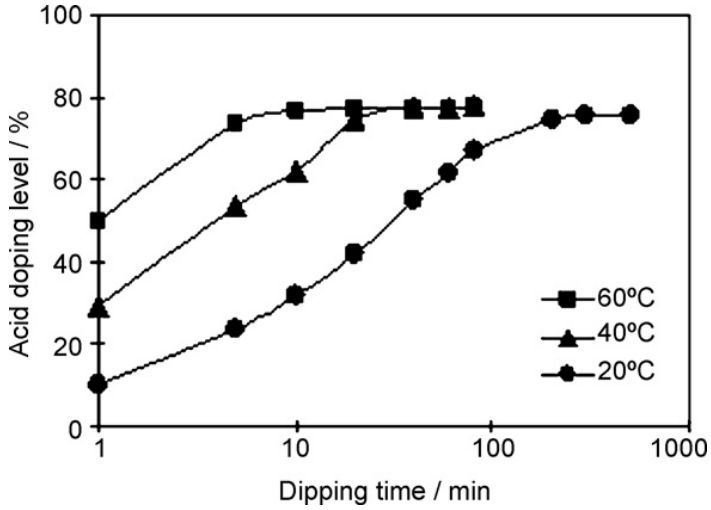

Fig.2.3 Influence of phosphoric acid solution temperature and immersion time on the acid-doping level of PBI.

Fig.2.4 shows the relationship between the immersion time for acid doping up to levels of 60%, 70%, and 78% and the temperature of the acid solution. There is an inversely proportional relationship between the immersion time up to the designated acid-doping level plotted with a non-logarithmic scale, and the solution temperature plotted with a logarithmic scale. Such a relationship shows that it is possible to control the acid-doping level of the PBI membrane by managing the solution temperature and the immersion time.

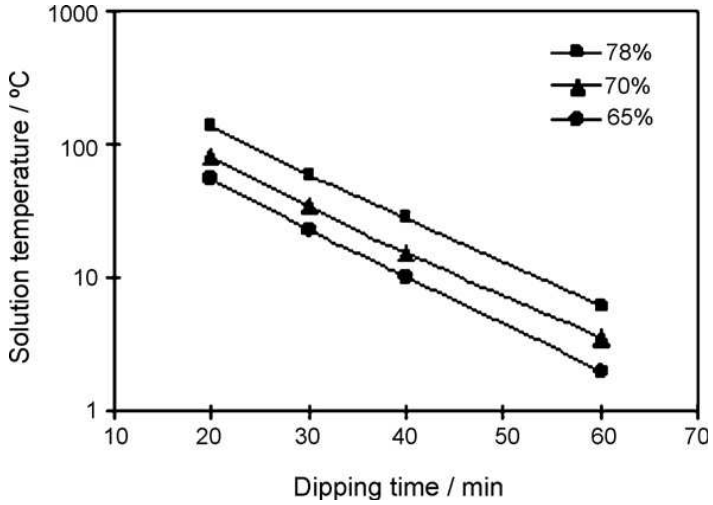

Fig.2.4 Relationship between the solution temperature and the immersion time to achieve designated acid-doping levels of 65%, 70% and 78%.

Fig.2.5 shows the relationship between the increase in the acid-doping weight/volume and the acid-doping level of the PBI membrane with an initial area of 5cm×5cm and initial thickness of 40 μ m, at a temperature of 40℃. The increase in the PBI membrane volume was calculated as the difference between the initial and expanded volume, obtained by taking the product of the experimentally measured length, width and thickness. There is a good correlation between the weight and volume increases and the increase in the acid-doping level; not only does the PBI membrane weight increase, but its volume also increases.

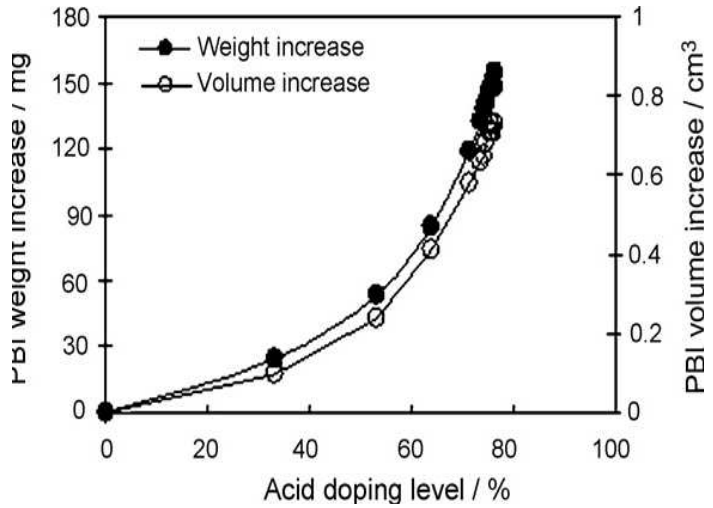

Fig.2.5 Relationship between the increase in the weight/volume and acid-doping level of the PBI membrane at 40℃.

2.3.3 Single cell test

Fig. 2.6 shows the cell voltage and internal resistance over time for single cells with acid-doped PBI membranes at levels of 65%, 71%, 75% and 78%, and at 0.2Acm^{-2}. The internal resistance was measured at a constant frequency of 1 kHz using an AC milliohm tester. All the cell tests were conducted for 450h (19 days). It was found that all the cell voltages had reached the saturation level after 200h of operation. The slow increase in cell voltage is thought to be due to the time required for volatilization of the solvent in the PBI membrane and the CL; therefore, the phosphoric acid flows slowly into the pores formed by solvent volatilization, and consequently, the proton conductivity is gradually improved.

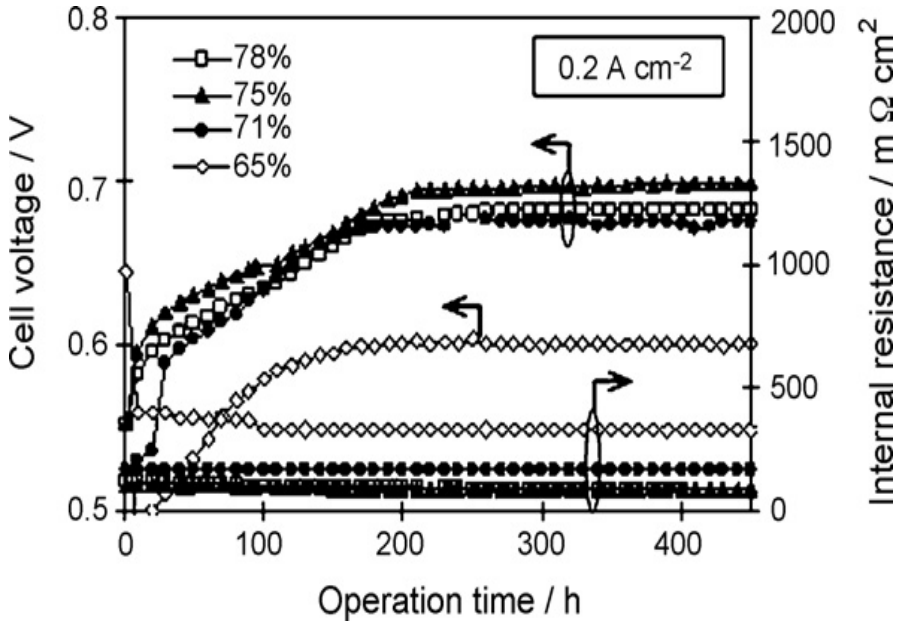

Fig.2.6 Cell voltage and internal resistance over time for single cells with acid-doping levels of 65%, 71%, 75% and 78% at 0.2Acm^{-2}.

Fig.2.7 shows the relationship of the cell voltage and internal resistance to the acid-doping level at an operation time of 450h. The cell voltage becomes higher with the increase in acid-doping level from 65% to 75%, peaks at around 75%, and then declines slightly with an increase in the acid-doping level over 75%. The relationship between the leak current of each cell obtained from the CC measurements and the doping levels are also shown in Fig.2.7. There was negligible crossover detected for all acid-doping levels, which verified that reduction of the acid-doping level in PBI membranes does not cause crossover.

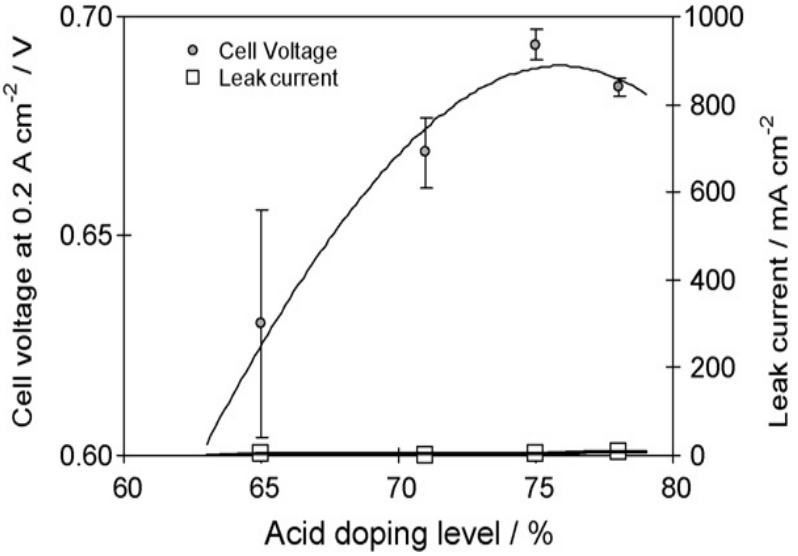

Fig.2.7 Relationship of cell voltage, internal resistance at 0.2Acm^{-2}, and leak current with respect to the acid-doping levels.

Fig. 2.8 shows the I–V curves and internal resistance for single cells with PBI membranes at acid-doping levels of 65%, 71%, 75% and 78% after 450h of operation. The stoichiometric flow rates of fuel and oxidant were 1.4 and 5, respectively. For acid-doping levels up to 75%, the cell voltage increases and the cell resistance declines with an increase in the acid-doping levels. With regard to the cell voltage drop from the open circuit voltage to the inflection point of the I–V curves in the low current density region below 0.1Acm^{-2}, which is often considered as the activation overpotential, there

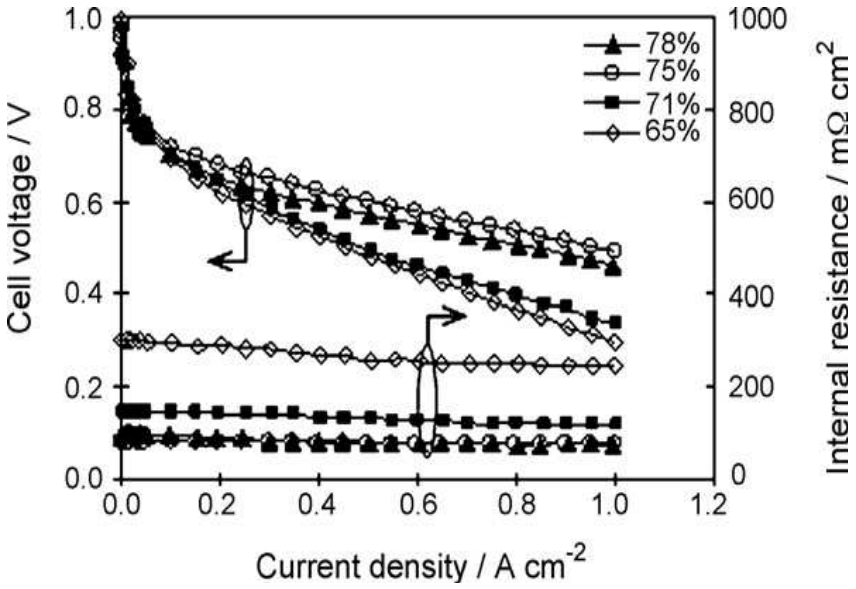

Fig.2.8 Influence of the acid-doping levels of PBI membranes on I–V characteristics and internal resistance of single cells.

were no significant differences among the single cells with various acid-doping levels. On the other hand, there was significant dependence of the resistance overpotential, which is usually defined as the product of the I–V curve slope and the current density, on the acid-doping levels.

In order to clarify this tendency, the relationship between the resistance overpotential of the single cells with various acid-doping levels and the current density is shown in Fig.2.9, and the relationship of the internal resistance at 0.2Acm^{-2} with the acid-doping level is shown in Fig. 2.10. It is thought that such an increase in the cell internal resistance with reduction

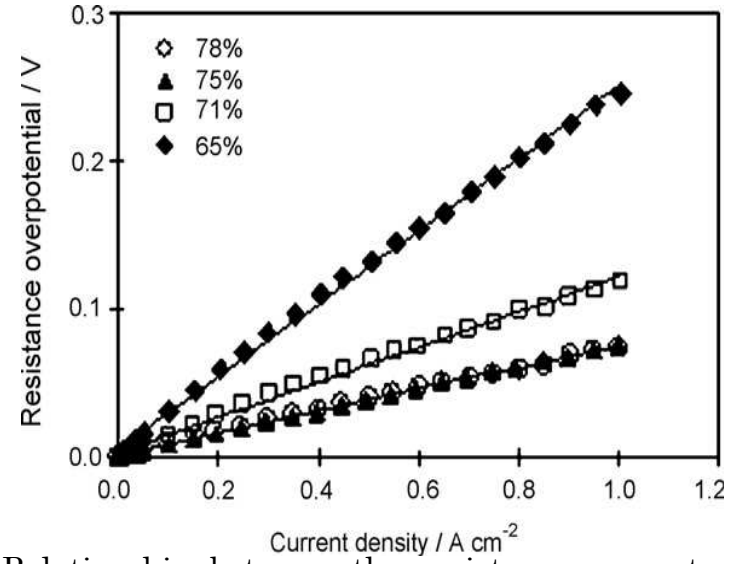

Fig.2.9 Relationship between the resistance overpotential and the current density for single cells with various acid-doping levels.

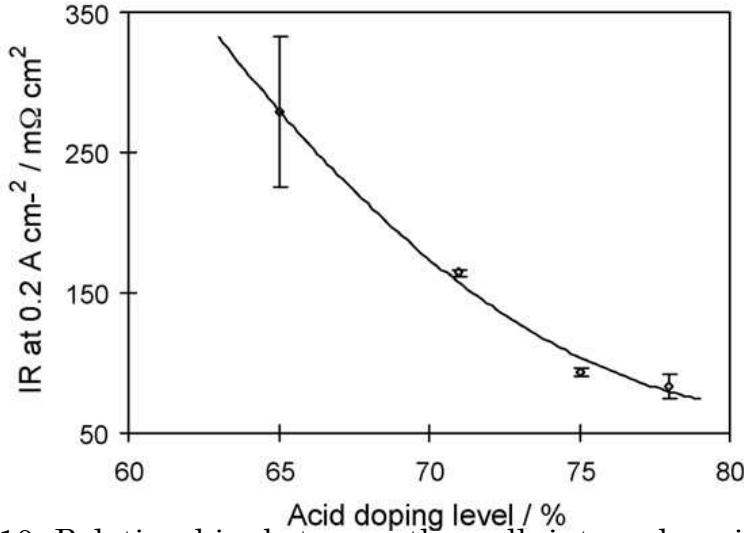

Fig.2.10 Relationship between the cell internal resistance at 0.2Acm^{-2} and the acid-doping level.

in the acid-doping level is caused by the reduction in the activation area of the catalyst layers, as shown in Fig. 11. For a single cell with a doping level below 75%, it is thought that there was not enough phosphoric acid migrating from the PBI film to the catalyst layers to obtain a sufficient active area, as shown schematically in Fig.2.11 (a) and (b). On the contrary, for the single cell with a doping level above 75%, it is thought that the catalyst layers were flooded with phosphoric acid that migrated from the PBI film, as shown in Fig.2.11(c).

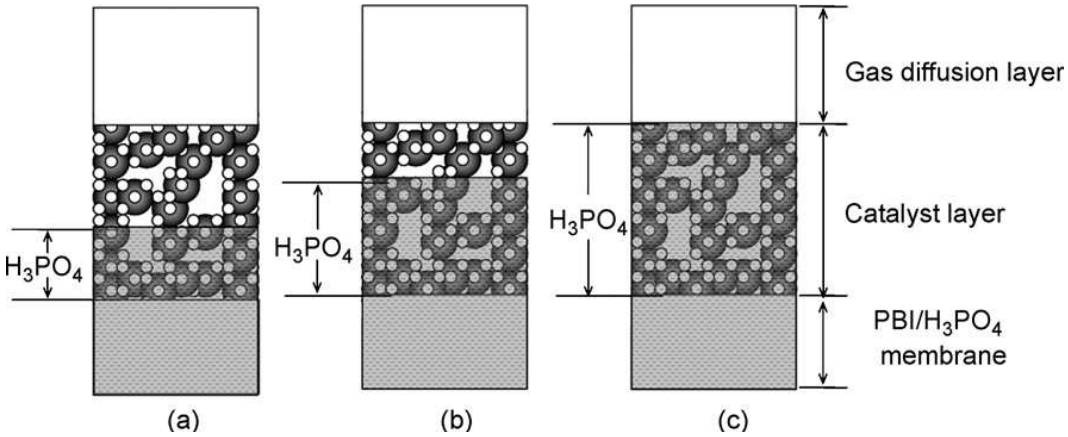

Fig.2.11 Schematic diagram illustrating the difference in the amount of phosphoric acid migration from the PBI film to the catalyst layer in single cells with different acid-doping levels of (a) 65%, (b) 71%, and (c) 78%.

2.3.4 AC impedance diagnosis for cell performance

AC impedance was used to clarify the influence of acid-doping level on the three main processes that limit cell performance: charge transfer, mass transport and ohmic resistance. AC impedance spectra of single cells with acid-doping levels of 65%, 71%, 75% and 78%were measured at a current density of 0.2Acm^{-2} throughout their entire operation, including the cell conditioning processes. During the measurement, pure hydrogen and air or oxygen were supplied to the anode and cathode sides, respectively.

Fig.2.12 shows typical AC impedance spectra for a cell with an acid-doping level of 75% when air was supplied to the cathode side. Two comparatively distinct arcs and one indistinct arc are observed in the regions of high and low frequency, respectively. With respect to these arcs, previous reports [5-11] have indicated that the high frequency intercept of the kinetic loop and the real impedance axis expresses the sum of the ohmic

resistance of the membrane, etc. In addition, the distance from the high-frequency real axis intercept to the next lower-frequency real axis intercept represents the anodic and cathodic charge transfer, and the third low frequency arc represents the mass transport impedance that occurs under conditions such as high current density, low airflow or cathode flooding. According to these previous studies, the AC impedance spectra suggest that the ohmic resistance of the membrane, etc., does not change significantly over time, even though there is acid migration from the membrane to the catalyst layer. They also imply that the charge transfer decreases over time with the volatilization of the solvent contained in the PBI membrane and catalyst layers and that the third low frequency arc begins from450 h with flooding of the CL with phosphoric acid that migrated from the membrane.

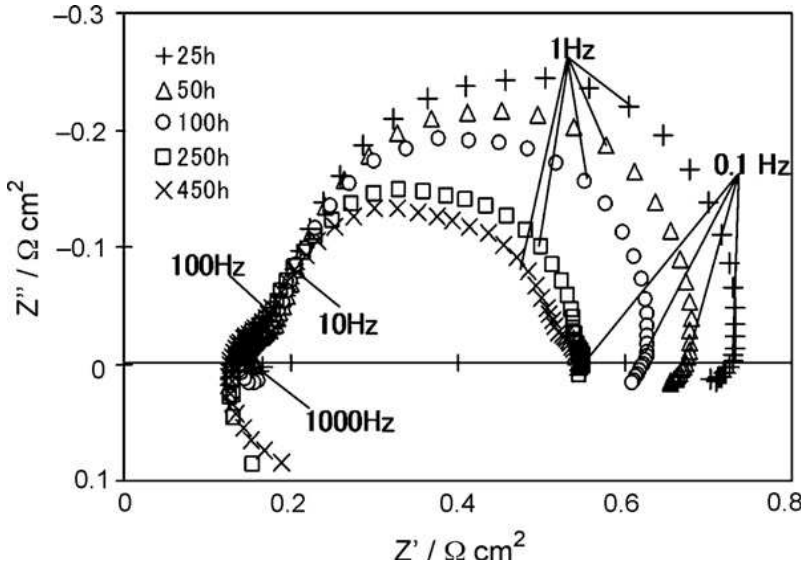

Fig.2.12 AC impedance spectra of a single cell with an acid-doping level of 75% at operation times of 25, 50, 100, 250 and 450h at current density of 0.2Acm^{-2} with pure hydrogen and air supplied to the anode and cathode sides, respectively.

Fig.2.13 shows the impedance spectra of single cells with acid doping levels of 65%, 71%, 75% and 78% when oxygen is supplied to the cathode side. Two high-frequency arcs and one distorted low-frequency arc are observed. The shapes of these arcs suggest the following that the ohmic resistance of the membrane, etc., decreases with increasing acid-doping level. They also imply that the charge transfer resistance does not necessarily depend on the acid-doping level and that the mass transport resistance of the cathode CL increases with an increase in the acid-doping

levels. Therefore, the result shown in Fig. 7, where the cell performance has a maximum around an acid-doping level of 75%, is supported by the AC impedance results; the ohmic resistance decreases and the mass transport resistance increases with increasing acid-doping level, and the sum of both resistances has a minimum value around an acid-doping level of 75%.

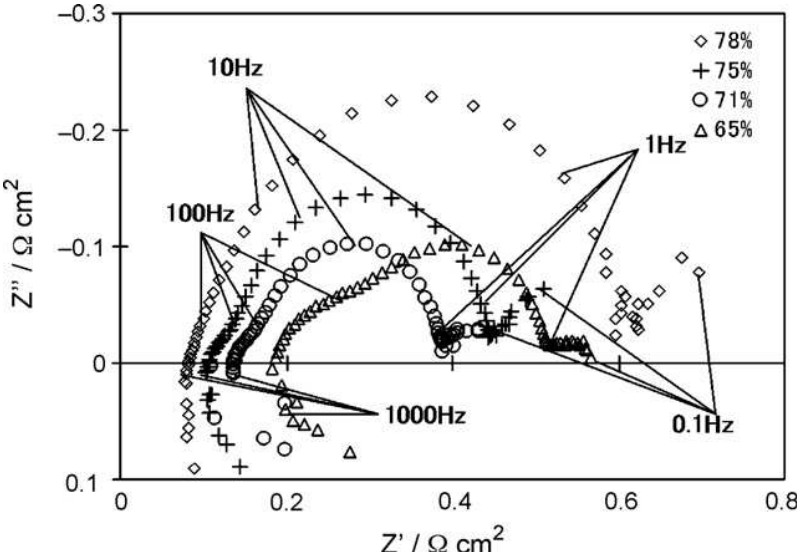

Fig.2.13 AC impedance spectra of single cells with acid-doping levels of 65%, 71%, 75%, 78% at an operation time of 450h at current density of 0.2Acm^{-2} with hydrogen and oxygen supplied to the anode and cathode sides, respectively.

2.3.5 Evaluation of acid migration

In order to have supporting data for the discussions on both the results of the single cell tests in Section 2.3.3 and the AC impedance spectra in Section 2.3.4, the weights of the membranes were measured before doping, after doping and after cell operation tests. The membrane weights divided by the active area are shown in Fig.2.14. Before doping, the four membranes had almost the same weights. With acid-doping, the weights increased to 2.86, 3.48, 3.98 and 4.54 times that of the initial weight for doping levels of 65%, 71%, 75% and 78%, respectively. After the cell operation tests, the weights decreased to 2.03, 2.18, 2.32 and 2.32 times the initial weight, respectively.

In addition to the weight measurements, the concentrations of phosphoric acid included in the total water exhausted from the cells were analyzed using ICPMS after the cell operation tests. Fig.2.15 shows typical amounts of phosphoric acid included in the water exhausted from cells with acid-doping levels of 65% and 78% after 450h operation (1.2×10^{-7} and

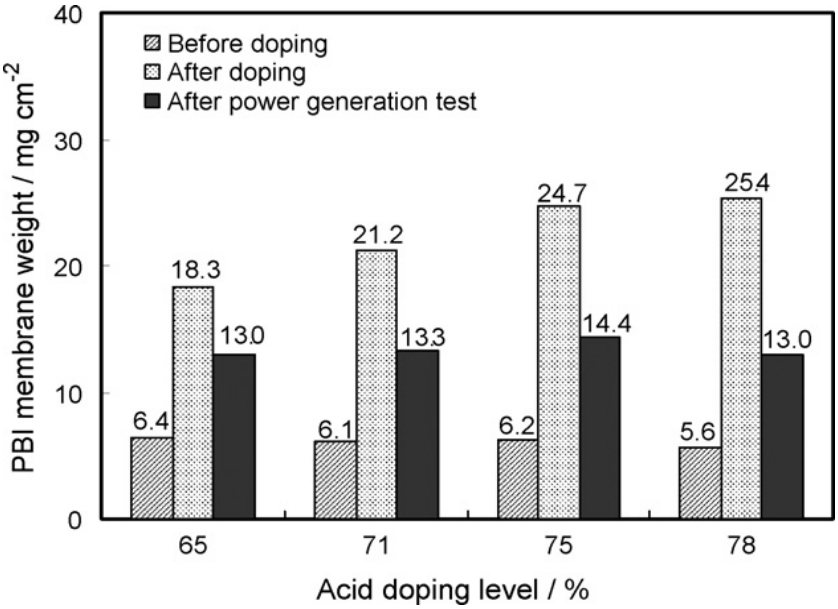

Fig.2.14 Change in the membrane weight before doping, after doping, and after the power generation tests.

2.3×10^{-7} mgcm^{-2}). The results indicate that the amounts of phosphoric acid included in the water exhausted from the cell were negligible, for both low and high acid doping levels. By combining the results of Figs.2.15 and 14, it was estimated that the amounts of phosphoric acid remaining in the catalyst layers after operation of single cells with acid-doping levels of 65%, 71%, 75% and 78% (5.3, 7.9, 10.3 and 12.4mgcm^{-2}) were 0.83, 1.30 and 1.66

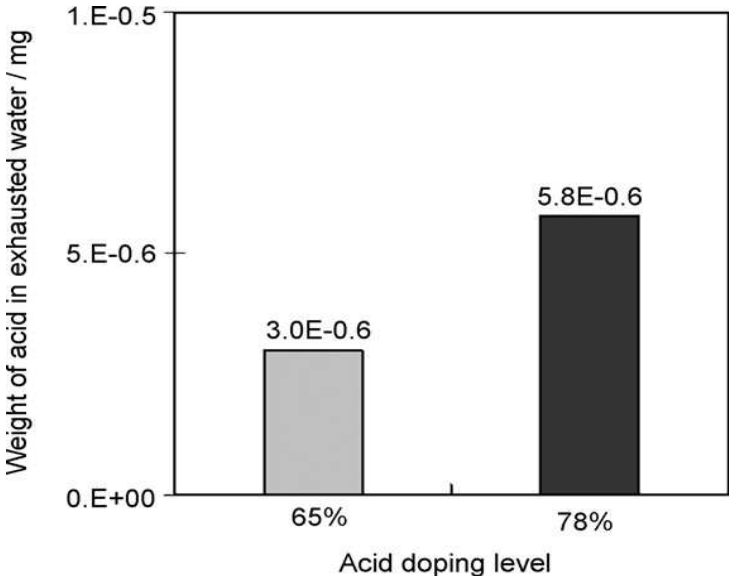

Fig.2.15 Weight of phosphoric acid included in the water exhausted from single cells with acid-doping levels of 65% and 78% during cell operation over 450h.

and 2.21 times that of the initial membrane weights, respectively. In the light of this result and those of the single cell tests in Section 2.3.3 and the AC impedance spectra in Section 2.3.4, it was concluded that approximately 10mgcm^{-2} is the optimum amount of phosphoric acid in a CL with a thickness of approximately 20μm, as used in this study.

2.4 Conclusions

For HT-PEMFC based on phosphoric acid-doped PBI membranes, it was clarified that the amounts of phosphoric acid doped in the membranes could be controlled by changing the phosphoric acid solution temperature and the immersion time in the phosphoric acid solution. Cell performance was improved by optimizing the amounts of phosphoric acid doped in the membrane and by the diffusion of phosphoric acid into the catalyst layer at the initial stage of cell operation. It was concluded that approximately 10mg cm^{-2} is the optimum amount of phosphoric acid for a catalyst layer with a thickness of approximately 20μm.

References

[1] N.H. Jalani, M. Ramani, K. Ohlsson, S. Buelte, G. Pacifico, R. Pollard, R. Staudt, R. Datta ; J. Power Sources 160 (2006) 1096.
[2] Z. Liu, J.S.Wainright, M.H. Litt, R.F. Savinell ; Electrochim. Acta 51 (2006) 3914.
[3] J.H. Kim, H.J. Kim, T.H. Lim, H.I. Lee ; J. Power Sources 170 (2007) 275.
[4] A. Sounai, K. Sakai ; Proceeding of FCDIC Symposium 13 (2006) 125.
[5] O. Antoine, Y. Bultel, R. Durand ; J. Electroanal. Chem. 499 (2001) 85.
[6] I.A. Schneider, H. Kuhn, A. Wokaun, G.G. Schere ; J. Electrochem. Soc. 152 (10) (2005) A2092.
[7] X. Yuan, H.Wang, J.C. Sun, J. Zhang ; Int. J. Hydrogen Energy 32 (2007) 4365.
[8] X. Yuan, J.C. Sun, M. Blanco, H.Wang, J. Zhang, D.P.Wilkinson ; J. Power Sources 161 (2006) 920.
[9] X. Yuan, J.C. Sun, H.Wang, J. Zhang ;J. Power Sources 161 (2006) 929.
[10] J. Zhang, Y. Tang, C. Song, J. Zhang ; J. Power Sources 172 (2007) 163.
[11] R.H. Song, D.J. Kim, C.S. Kim, D.R. Shin ; J. New Mater. Electrochem. Syst. 4 (2001) 47.
[12] J. Yu, Y. Yoshikawa, T. Matsuura, M.N. Islam, M. Hori ; Electrochem. Solid-State Lett. 8 (3) (2005) A152.
[13] Y. Zhai, H. Zhang, G. Liu, J. Hu, B. Yi ; J. Electrochem. Soc. 154 (2007) B72.
[14] J. Yu, T. Matsuura, Y. Yoshikawa, M.N. Islam, M. Hori ; Electrochem. Solid-State Lett. 8 (3) (2005) A156.

Chapter 3

Influence of operating temperature on cell performance and endurance of HT-PEMFC

3.1 Introduction

As mentioned in the chapter 2, it is very important for HT-PEMFC to improve its cell performance. Increasing the cell temperature is the easiest way to improve the cell performance. However, there is a dilemma in that raising the operating temperature in order to increase the cell voltage and improve the efficiency makes it difficult to sustain long-term durability. Conversely lowering the temperature improves the durability but leads to lower cell voltages. To date, only a few reports have dealt with the relationship between the operating temperature and the cell durability, including the deterioration mechanism during approximately 500h operation at 150℃ [1–4].

Therefore, in this chapter, the effects of temperature on the cell voltage and durability were evaluated by conducting long-term durability tests on cells using PBI membranes doped with phosphoric acid and using newly developed electrodes for cell temperatures of 150, 170, and 190℃. The deterioration mechanism of the cells was investigated based on the results of time variations of cell voltage, internal cell resistance and impedance during the durability tests, in addition to post-analysis by transmission electron microscopy (TEM) observations.

3.2 Experimental

3.2.1 Preparation of PBI electrolyte membrane

PBI membranes (5.5cm×5.5cm, ca. 40μm thick) provided by the Joint Research Institute were immersed in a 85% phosphoric acid solution heated to 40℃ for 40min to dope the membranes [5]. Identical membranes doped under identical conditions were used for all tests in this chapter. The phosphoric acid doping ratio was determined by measuring the weight of the membranes before and after doping using a precision electronic balance (AUW120D Shimadzu Corp., Japan). The doping ratio was defined as the weight of phosphoric acid doped into the membrane divided by the weight of the membrane after doping.

3.2.2 Production of electrodes

A sheet of carbon paper with a thickness of 280μm (TGP-H090, Toray Corp., Japan) was used as a gas diffusion layer. A mixed powder of Ketchen Black (EC-600JD, Akzo Nobel Corp., UK) and polytetrafluoroethylene (PTFE, DuPont) in a weight ratio of 65:35 was applied onto the carbon paper using a dry coating device [5-7] until it formed a coating of 2mg cm^{-2}. This was then heated at 350℃ in an atmospheric oven, and the surface leveled by a roller press [5-7] to produce a filled carbon layer.

A catalyst ink was then prepared by mixing polyvinylidene fluoride (PVDF; Kureha Corp., Japan), Pt–Co-supported on Ketchen Black powder (carbon/metal: 50/50, TKK Corp., Japan) [5] and N-methyl pyrrolidone (NMP; Sigma–Aldrich Corp., USA) with agitation for 60h. For preparation of the electrode, the catalyst ink was applied using a wet coating method onto the coated carbon paper, dried for 1h at 80℃ in air, and then finally held in a vacuum oven at 160℃ for 25h to remove NMP [5]. The amount of supported Pt was approximately 0.8mgcm^{-2} for both anode and cathode electrodes.

3.2.3 Single cell assembly

The electrolyte membrane doped with phosphoric acid was sandwiched by two electrodes prepared according to Section 3.2.2 to produce the membrane electrode assembly (MEA). This was sandwiched between a pair of bi-polar plates made of carbon, on which a serpentine flow pattern was machined. The flow pattern was designed by Japan Automobile Research Institute (JARI) and had a reaction area of 5cm×5cm. Further, this assembly was in turn sandwiched by current collector plates and stainless steel end plates fitted with a rubber heater on the outermost surface and tightened using eight M6 bolts to produce a single cell [5]. Five of these single cells were prepared.

3.2.4 Single cell power generation tests

The five single cells described in Section 3.2.3 were mounted on a fuel cell test stand (Kofloc Corp., Japan) equipped with massflow controllers, an electronic loading device (Kikusui Electronics Corp., Japan) for controlling the electric current, an AC milliohm tester (Model 3566, Tsuruga Electric Corp., Japan) with a constant frequency of 1kHz, and a personal computer for equipment monitoring and data output. Tests of the initial

characteristics, long-term durability and power output over 1000h were conducted on a single cell, three single cells and the remaining single cell, respectively. During all tests, 130mLmin^{-1} (stoich: 3.7) of pure hydrogen was supplied to the anode side, and 310mLmin^{-1} (stoich: 3.7) of air or 66mLmin^{-1} (stoich: 3.7) of pure oxygen was supplied to the cathode side, with none of the reaction gases being humidified [5]. All power generation processes were conducted under atmospheric conditions.

3.2.4.1 Initial performance test

In this test, power was generated from a single cell at a cell temperature of 150℃ and a current density of 0.2Acm^{-2} for 500h until the cell voltage reached its peak and stabilized. The cell temperature was then varied from 140 to 200℃ with 10℃ increments, holding the temperature at each stage for approximately 1h to measure the cell voltage and internal resistance.

The impedance was then measured by sweeping a constant AC current of 5A(0.2Acm^{-2}) with an amplitude of 0.5A within the frequency range of 20,000-0.01Hz using a potentiostat-galvanostat (HZ 5000 HAG-3001, Hokuto Denko Corp.) and a frequency response analyzer (FRA 5020A, NF Corp., Japan) to examine details of the cell resistance [5]. In this case, hydrogen was supplied to the anode side and pure oxygen to the cathode side.

3.2.4.2 Long-term durability test

In this test, the temperatures of the three single cells were fixed at 150, 170, and 190℃, respectively, and the current density was controlled to maintain a current density of 0.2Acm^{-2} using an electronic loading device. In this case, the rate of decrease in cell voltage was calculated based on the difference between the peak cell voltage and that measured during long-term power generation. Power generation was terminated when the cell voltage dropped by 10%. For the cell at 170℃, the impedance was measured in the same manner as described in Section 3.2.4.1 after 5,000h of operation, and power generation was then terminated.

The remaining cell was operated for approximately 1,000h at 150℃ at a current density of 0.2Acm^{-2} and the catalyst was then examined using TEM.

3.2.5 Post-analysis

TEM observations were carried out both on as-prepared electrode catalysts and those following testing for about 1,000h at 150 and 190℃. In addition, scanning electron microscopy (SEM) observations were performed on the membrane subjected to the long-term durability test at 170℃.

3.3 Results and discussion

3.3.1 Initial performance test

Fig. 3.1 shows the relation between the cell voltage and cell temperature obtained from the initial performance test described in Section 3.2.4.1, as an Arrhenius plot. When the cell temperature was subsequently raised from 140℃ ($10^3/(140+273)=2.4K^{-1}$) to 200℃($10^3/(200+273=2.1K^{-1}$) in increments of 10℃, the cell voltage increased at a rate of approximately 10mV per 10℃, i.e., at $1mV \circ C^{-1}$. A similar dependence of cell voltage on temperature has been previously reported for phosphoric acid-PBI electrolyte membranes [8, 9, 10].

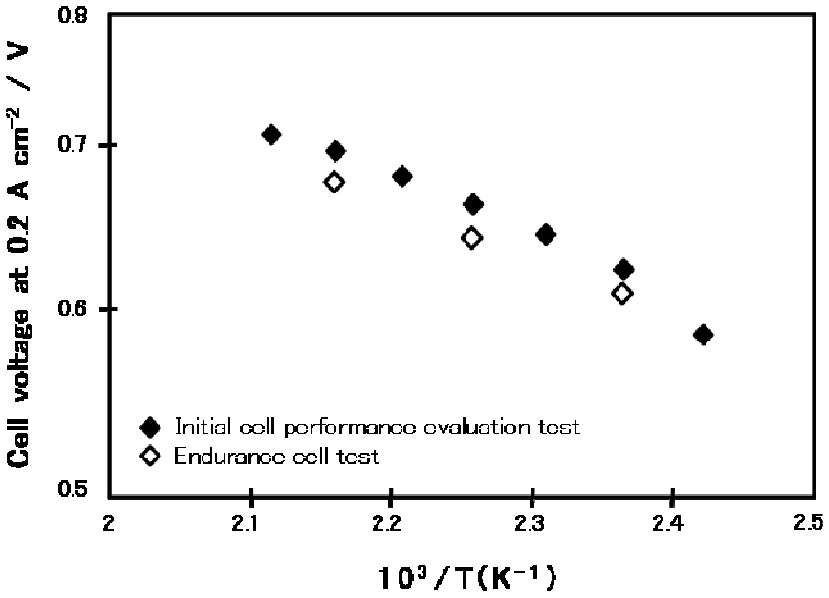

Fig.3.1 Relationship between cell voltage and cell temperature obtained from the power generation tests.

Fig.3.2 shows a Cole–Cole plot obtained from impedance measurements conducted at $0.2Acm^{-2}$ for the same single cell, whereas Fig.3.3 plots the ohmic, electric charge transfer, and mass transport resistance values derived from the data of Fig.3.2 relative to the cell temperatures.

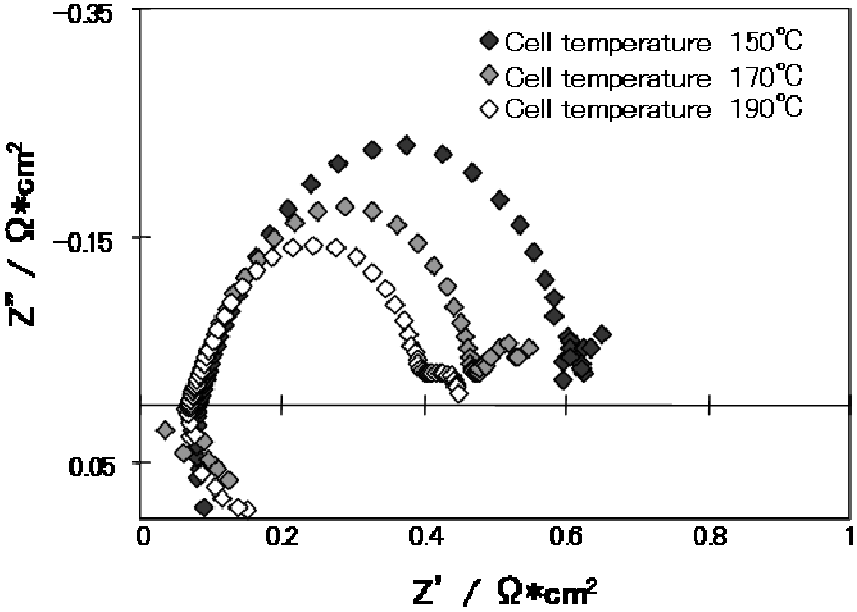

Fig.3.2 Cell temperature dependence of the Cole–Cole plots at 0.2Acm^{-2} for an initial performance evaluation after 500h operation.

As can be seen, the ohmic resistance drops slightly with increasing cell temperature. In general, ohmic resistance is related to electrical resistance, contact resistance, and the membrane proton conductivity. The decrease in ohmic resistance seen in Fig.3.3 is believed to be due to an improvement in proton conductivity in the electrolyte membrane with increasing cell temperature. This is supported by the work of Zhang et al. [8] on the influence of cell temperature on membrane resistance, and the relation between proton conductivity in phosphoric acid-PBI electrolytic membranes and cell temperature reported by Ma et al. [11].

Furthermore, Fig.3.3 shows that the charge transfer resistance is markedly reduced with increasing cell temperature. It is generally believed that the electrical charge transfer resistance is related to the catalyst activity of the cathode and anode. Therefore, it seems likely that an increase in temperature gave rise to an increase in catalyst activity, promoting electrode reactions and consequently leading to an increase in cell voltage. Zhang et al. also measured the impedance spectra of HT-PEMFCs at various cell temperatures and similarly concluded that the charge transfer resistance is reduced by the promotion of anode oxidization and cathode reduction as the cell temperature increases [8]. Further, Ajani et al. showed that the activation overpotential of HT-PEMFCs was reduced as the cell

temperature increased [9], which lends further support to this idea.

In Fig.3.3, it can be seen that a slight reduction in the mass transport resistance occurs as the cell temperature increases. The mass transport resistance is determined by the rate of diffusion of the reactant gas in the porous electrode and the electrolyte, and by its solubility into the electrolyte. Increasing the cell temperature leads not only to higher gas diffusion rates, but also a reduction in gas solubility. Which of these factors has the dominant influence on the mass transport resistance depends on the current density. It has been reported that at high current density, the reduction in gas solubility dominates and an increase in cell temperature leads to a higher mass transport resistance [8]. However, in this study, the impedance measurements were conducted at a low current density of 0.2Acm^{-2}. Under these conditions, the enhancement of gas diffusion had the largest impact, leading to a reduction in mass transport resistance as the temperature increased.

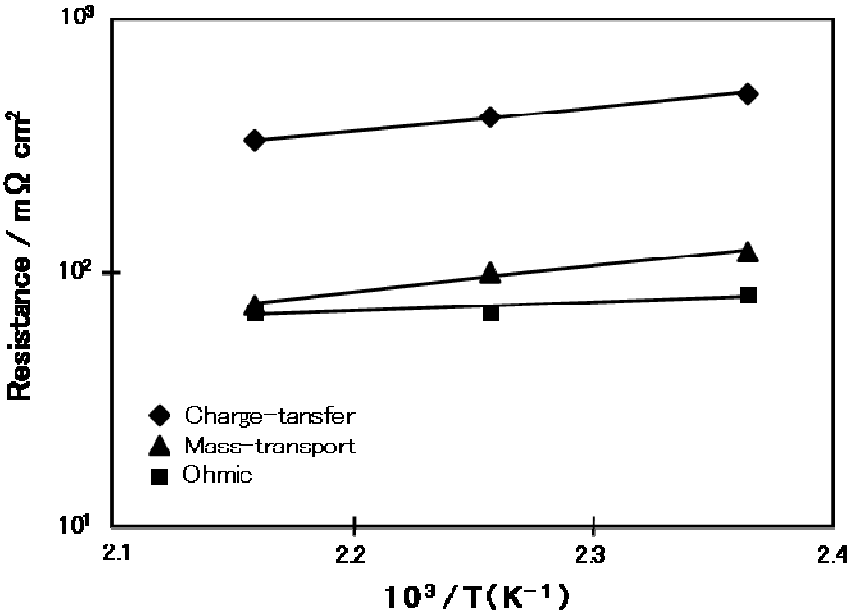

Fig.3.3 Relationship of the ohmic, charge transfer and mass transport resistance to the cell temperature.

3.3.2 Long-term durability test

Fig.3.4 (a), (b), and (c) show the changes in cell voltage and internal resistance over time during the long-term durability tests at 150, 170, and 190℃, respectively. In these tests the current density was constant at 0.2Acm^{-2}.

As seen in Fig.3.4 (a), in the case of the 150℃ cell, the cell voltage

gradually increased from the beginning of power generation, reached a peak value after several hundred hours, and then declined very gradually for the

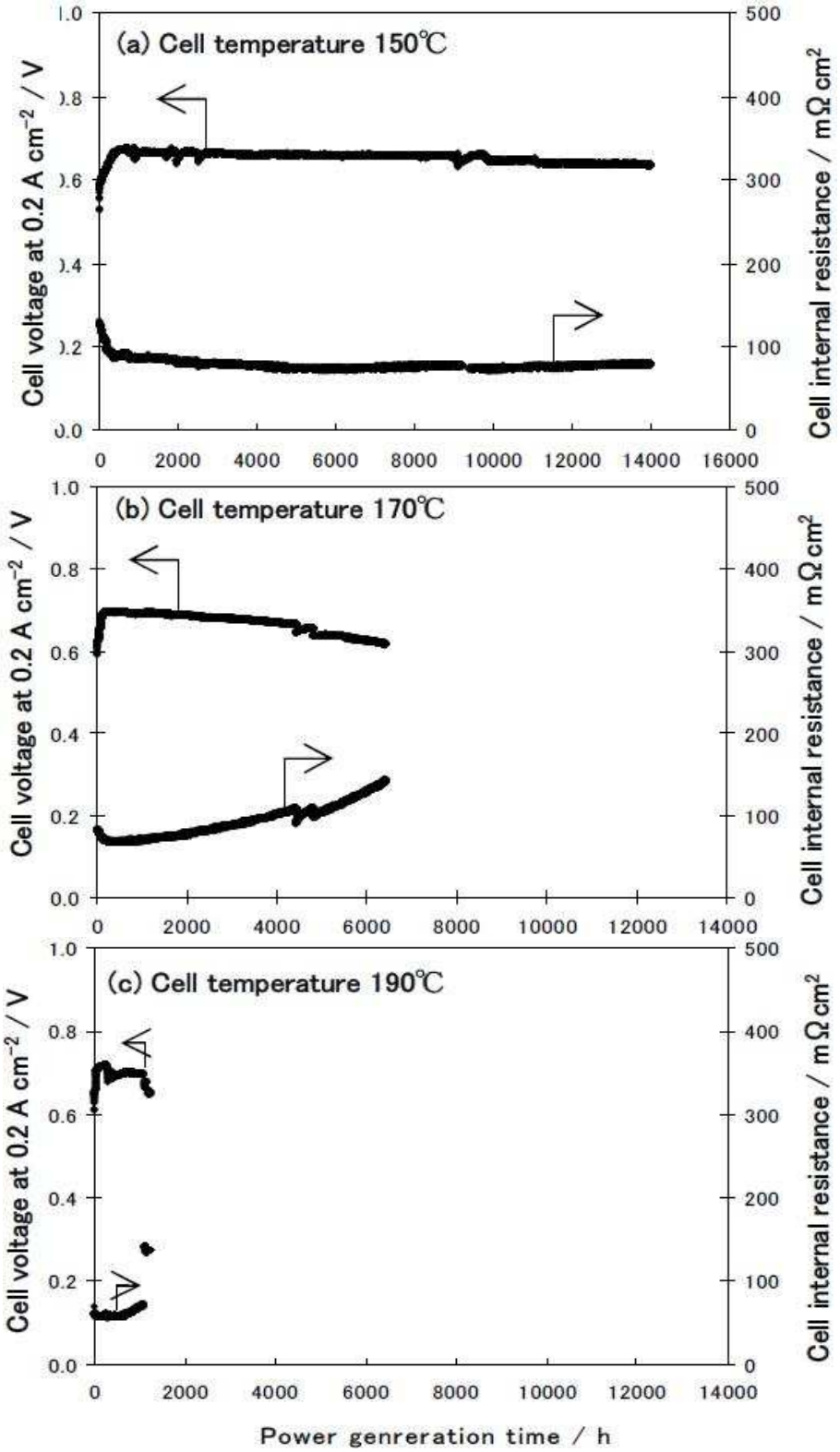

Fig.3.4 Time course of cell voltages and internal resistances of three cells operated at 0.2Acm^{-2} at cell temperatures of 150, 170 and 190°C.

remaining period. Even following 16,000h (2 years) of operation, the cell voltage drop is still within 7% of its peak value, and the power generation test is currently still in progress. The three temporary drops which appear in the curve are due to emergency stops of the test stand. On the way, up to approximately 12,000h, no significant changes were observed in the cell internal resistance, which is related to the ohmic resistance and the proton conductivity resistance, although a gradual increase was observed over 12,000h.

In the 170℃ cell shown in Fig.3.4 (b), the cell voltage increased relatively rapidly from the beginning of power generation, reached its peak value in a few hundred hours, and then dropped gradually. At around 4,500h, a sharp drop occurred due to a gas stoppage incident, but recovery took place within several hundred hours. However, from approximately 5,000h, the cell voltage began to drop with increasing speed. Power generation was terminated after 6,400h of operation, at which point the cell voltage had declined 10% from its peak value. During the entire duration of the test, apart from the very early period, the internal resistance continued to increase as the voltage decreased.

As seen in Fig.3.4 (c), the voltage of the 190℃ cell reached a peak almost immediately after the start of the power generation and then dropped due to a gas stoppage incident, similar to those for the 150 and 170℃ cells. However, in contrast to the other two cells, the cell voltage did not quickly recover, but remained at a low level for approximately 500h, and then dropped sharply after 1,000h of operation. Power generation was terminated after 1,220h of operation when the cell voltage had dropped by 10% from its peak value.

Fig.3.5 shows the relation between the rate of increase of the cell voltage during the initial period of power generation and the cell temperature, which was obtained by arranging the results shown in Fig.3.4. Clearly, the initial cell voltages increase more rapidly as the temperature increases. The initial time required for the cell voltage to stabilize is considered to correspond to the time taken for the NMP solvent remaining in the catalyst layer to evaporate and for the space thus produced to be filled with enough phosphoric acid to secure a sufficient charge transfer path in the cell [6]. In fact, all of the cell temperatures are fairly close to the boiling point, 220℃, of NMP. In particular, in the cell operating at 190℃, the solvent would be expected to quickly evaporate due to its high saturated vapor pressure.

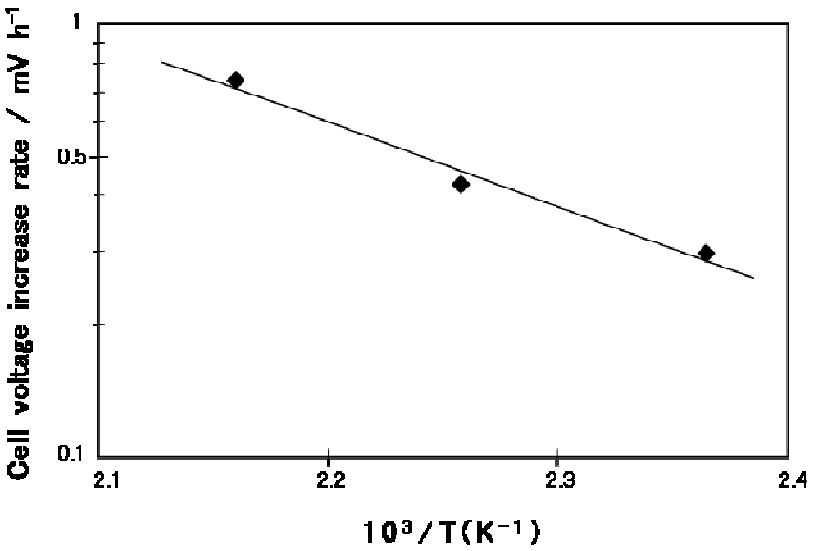

Fig.3.5 Relationship of cell voltage increase rate to cell temperature during initial power generation.

Fig.3.6 shows the rate of decrease of the cell voltage from its peak value as a function of the cell temperature. For the 150℃ cell, the rate was obtained by dividing the cell voltage drop from its peak to 16,000h, read from Fig.3.4 (a). For the 170 and 190℃ cells, the rates were obtained by dividing the cell voltage drops of 10% from the peak voltage, shown in Fig.3.4 (b) and (c), by the final power generation time of 6,400 and 1,220h, respectively. As seen in Fig.3.6, the cell voltage deterioration rate was strongly dependent on temperature, and had a value of 3.6mVh^{-1} for a cell temperature of 150℃.

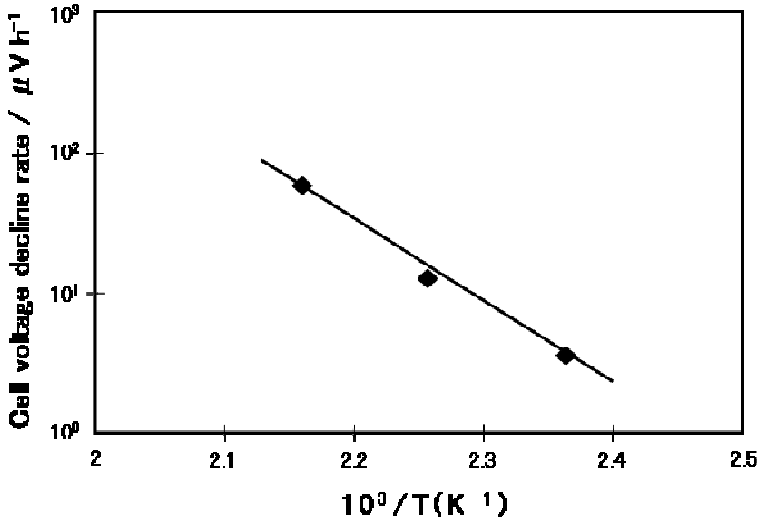

Fig.3.6 Relationship of cell voltage decline rate to cell temperature over long-term power generation.

Fig.3.7 shows the time dependence of the resistance overpotential and the cell voltage loss excluding resistance. The “resistance overpotential” is the product of the current density ($0.2Acm^{-2}$) and the cell internal resistance taken from Fig. 4. “Loss excluding resistance” is obtained by subtracting the

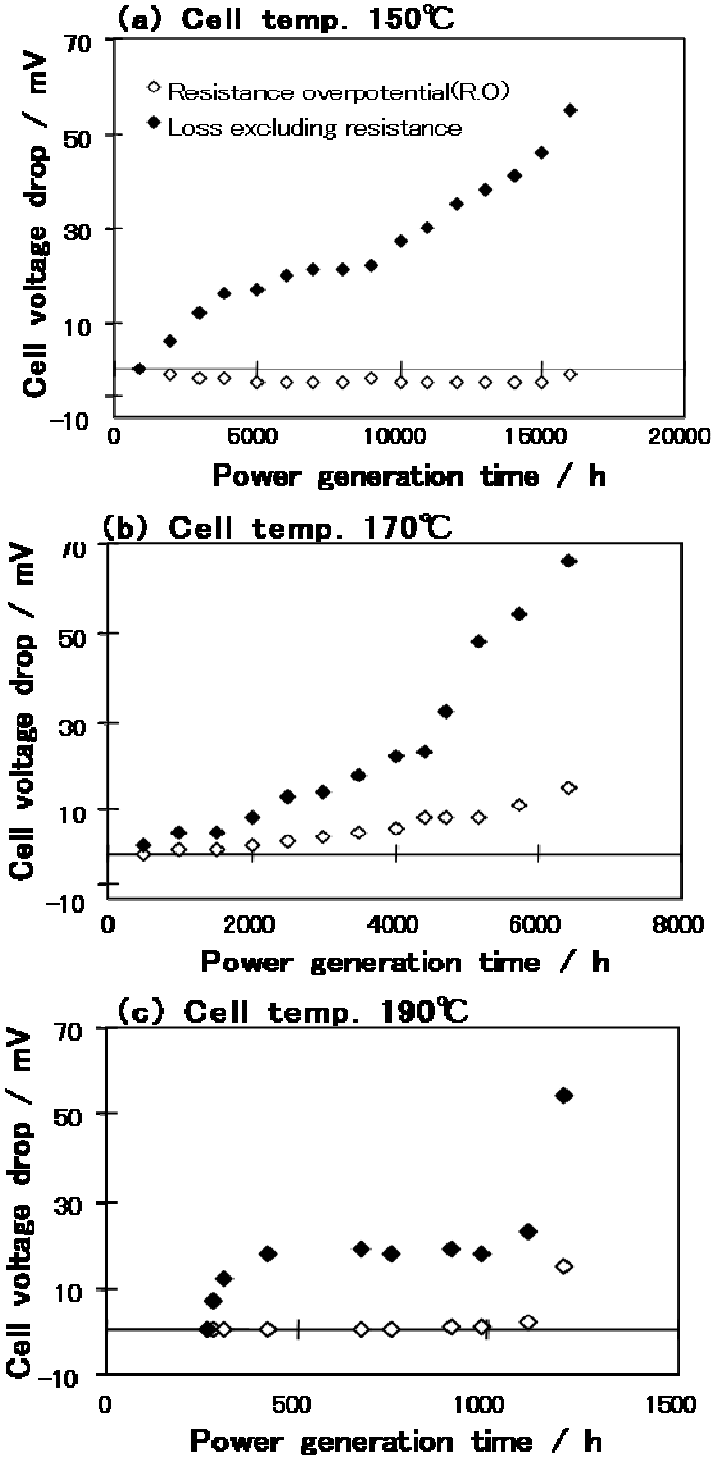

Fig.3.7 Time course of the cell voltage drop due to the resistance overpotential and losses except cell resistance for cells operated at 150, 170 and 190℃.

resistance overpotential portion from the total cell voltage drop. Therefore, the loss excluding resistance includes the increase of activation overpotential, the increase of diffusion overpotential, and the decrease in the open circuit voltage (OCV). However, the effect of diffusion overpotential is very small, because the long-term durability tests were conducted at a low current density of $0.2 Acm^{-2}$, as has been discussed previously.

As shown in Fig.3.7 (a), for the cell operating at 150℃, the resistance overpotential dropped gradually from the initial period of power generation to approximately 4,000h, and remained constant thereafter until 16,000h. On the other hand, the loss excluding resistance increased gradually from approximately 500h, became almost constant from about 5,000 to 10,000h, and then began to increase again. For the cell operating at 170℃, the resistance overpotential increased gradually from approximately 500h and then more rapidly after roughly 5,000h, as shown in Fig.3.7(b). The loss excluding resistance increased gradually from 500h, became constant from 2,500 to 3,000h, and then increased sharply again after 4,000h. Further, for the cell operating at 190℃, as shown in Fig.3.7 (c), the resistance overpotential remained constant from 250 to about 1,000h, after which it sharply increased. The loss excluding resistance increased rapidly from approximately 250h, became constant after 500h, and then increased sharply again from 1,000 h.

Although the cell voltage deterioration rate varies with temperature, the losses excluding resistance showed a similar trend in all cells: an initial increase, an almost flat period, and finally a sharp increase accompanying the final reduction of cell voltage. Furthermore, the resistance overpotential in the 170 and 190℃ cells also showed a tendency to increase sharply as if synchronized with the final increase of the loss excluding resistance.

Fig.3.8 shows TEM images of electrode catalysts, (a) just prior to assembly into the cell (see Section 3.2.2), (b) after a power generation test at 150℃ for 1,029h, and (c) after a power generation test at 190℃ for 1,220 h (see Fig. 3.4(c)). Particle size distributions and mean particle diameters for the platinum-cobalt grains are also shown in Fig.3.8. As seen in Fig.3.8 (a), the mean particle diameter in the catalyst before power generation was 3.8 nm. However, following power generation for approximately 1,000 h at 150 and 190℃, the mean diameters of the catalyst particles grew to 4.1 and 6.0 nm, respectively, as shown in Fig.3.8 (b) and (c). In previous studies, it was also reported that the size of platinum catalyst particles grew during power

generation in a relatively short period of approximately 500h at 150℃ [1-4]. Further, Zhai et al. showed that platinum aggregation occurs in the early stage of power generation and that the cell performance is reduced due to a decrease in the specific surface area of the platinum particles and an

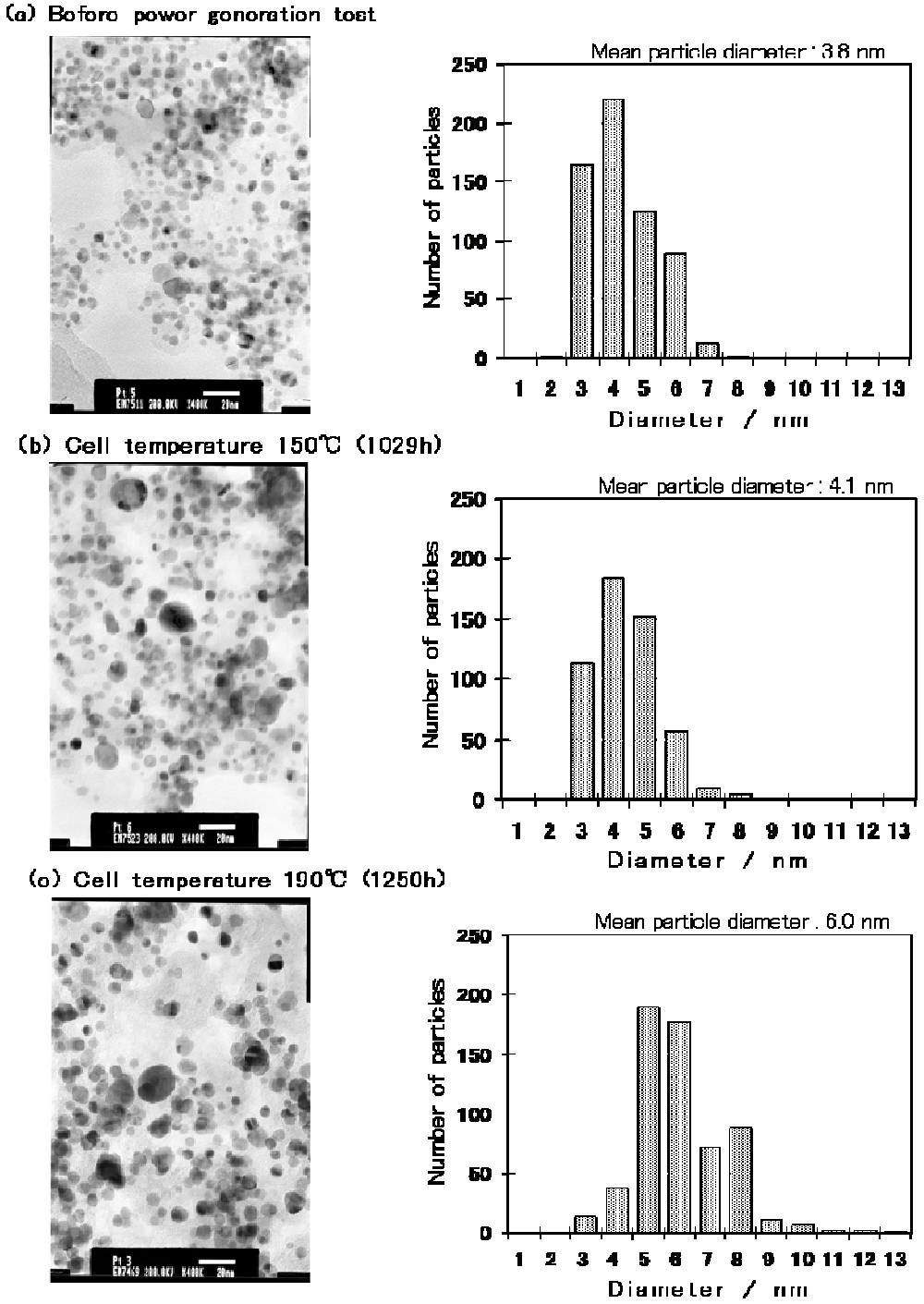

Fig.3.8 TEM micrographs of the Pt-Co catalyst (a) before the power generation test, (b) after 1,029 h operation at 150℃, and (c) after 1,250 h operation at 190℃.

increase in the reaction resistance [4]. Taking these results into account, it is suggested that grain growth in the catalysts is largely responsible for the reduction of cell voltage of approximately 20mV in the initial period of the durability test, due to an increase of the activation overpotential. However, since the cell voltage remains constant for a long time after its initial drop of 20mV, as shown in Fig.3.7, it is believed that some other factor is responsible for the final drop in cell voltage and increase of resistance overpotential. In order to investigate factors other than catalyst particle aggregation, OCV, impedance, and SEM surface measurements were carried out.

Fig. 3.9 shows the time dependence of the OCV drop for the 170℃ cell in the final period from 4,700 to 6,400h, together with the data for resistance overpotential and loss excluding resistance, which were already presented in Fig.3.7 (b). The OCV was found to decrease by approximately 25mV during this period, while the resistance overpotential increased by approximately 10mV. If the OCV reduction of 25mV is subtracted from the loss excluding resistance of 35mV, then the increased portion of the activation and diffusion overpotential is approximately 10mV. Thus, it can be concluded that the reduction in the OCV is the dominant factor involved in the cell voltage drop during the terminal period of cell life.

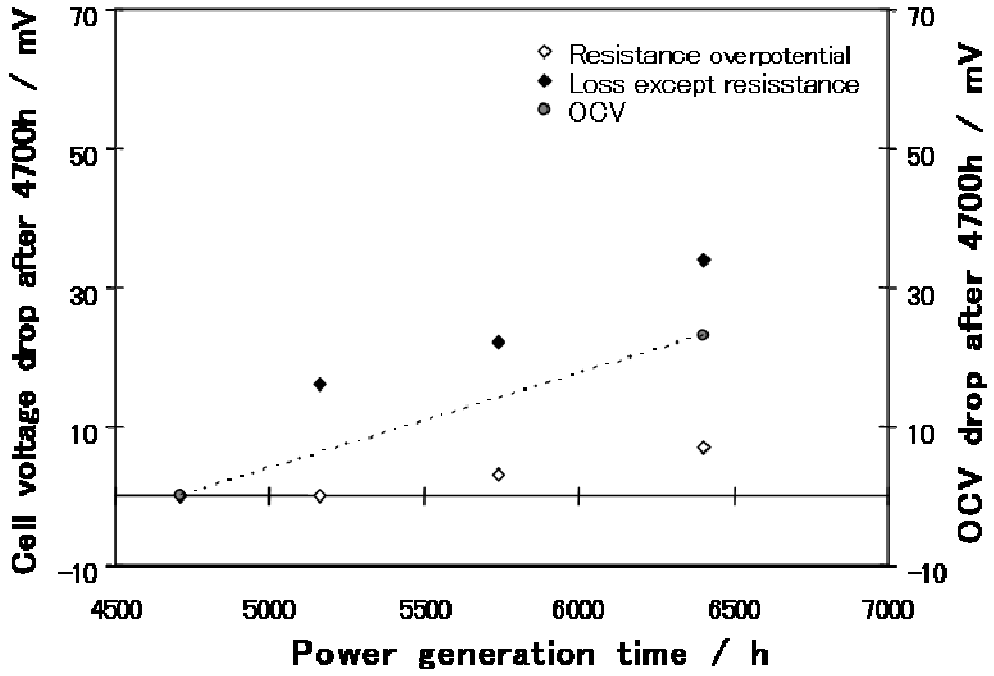

Fig.3.9 OCV and cell voltage drops of the cell operated at 170℃ from 4,700h.

Fig.3.10 (a) and (b) show SEM micrographs of the surface of the acid-doped PBI electrolyte membrane before and after power generation for 6,400 h at 170℃, respectively. In Fig.3.10 (b), some localized holes are seen in the cell membrane. It is thought that, in the final stages of cell life, H_2 crossover via such holes leads to the generation of HO・ and HO_2・ radicals that accelerate membrane deterioration, resulting in the reduction of OCV. There has been a report regarding such an attack on the electrolyte membrane by HO・ and HO_2・ radicals [3], and this has been suggested as being the main cause of termination of the cell life. In order to further investigate the cause of such damage to the membrane, impedance measurements were conducted on the 170℃ cell during the terminal period of its life.

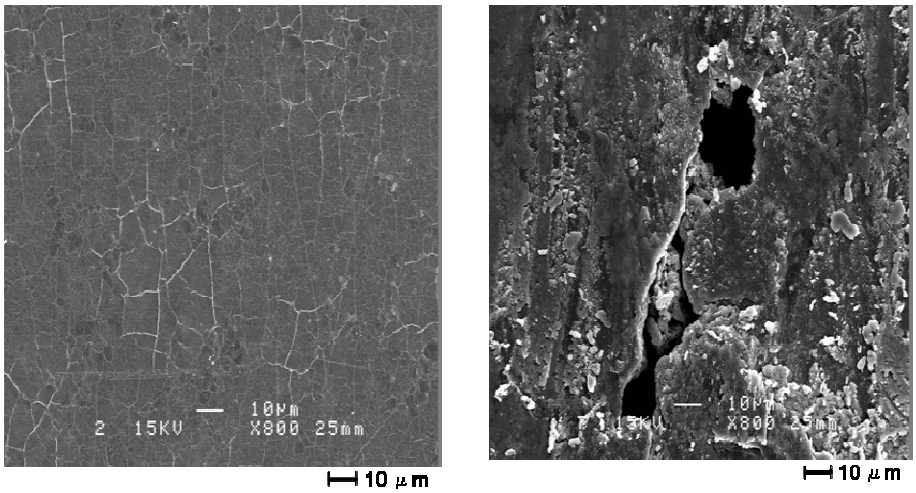

(a) Membrane after doping

(b) Membrane after power generation test at 170℃

Fig.3.10 SEM micrographs of electrolyte membranes after doping and after the power generation test at 170℃.

Fig.3.11 shows Cole-Cole plots of the 170℃ cell obtained by impedance measurements at 5,000h when the cell voltage started to decrease significantly, and at 6,400h when the power generation was terminated. Fig.3.12 shows the dependence of ohmic, charge transfer, and mass transport resistance on the operation time, taken from the data of Fig.3.11. Both figures show an increase in the ohmic and charge transfer resistance from 5,000 to 6,400h. In contrast, the mass transport resistance decreases, even at a low current density of $0.2Acm^{-2}$, as the gas diffusion rate improves. On the other hand, it was mentioned in the chapter2 that lower phosphoric acid doping, i.e., less phosphoric acid in the catalytic layer, increases both the ohmic and charge transfer resistances, and consequently

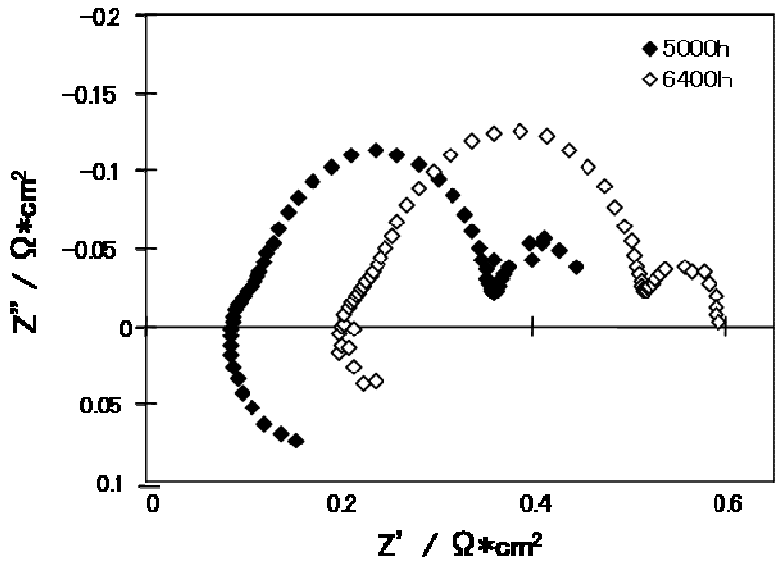

Fig.3.11 Cole–Cole plot for the cell operated at 170℃ for 5,000h and after power generation.

reduces the cell voltage [5]. On the basis of these results, it is considered likely that the phosphoric acid in the membrane and catalyst layers gradually evaporates and finally dries out during long-term operation, resulting in an increase in both the ohmic and charge transfer resistance, while concurrently enhancing gas diffusion and reducing the diffusion

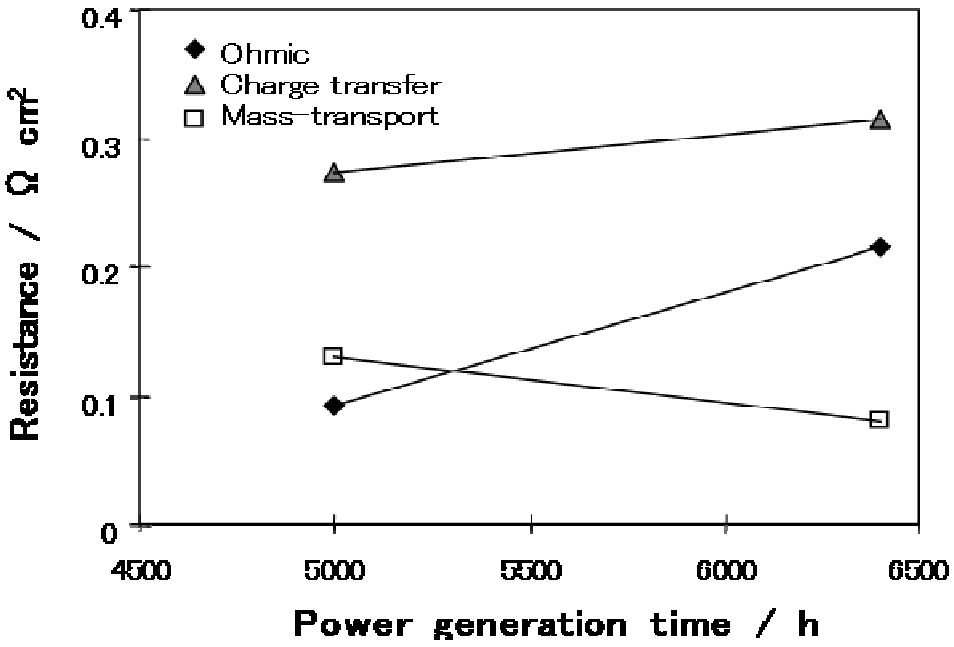

Fig.3.12 Time course of ohmic, charge transfer and mass transport resistance in the final stage of lifetime for the cell operated at 170℃.

resistance. Although it is as yet unclear whether radical attack on the membrane or the drying up of phosphoric acid acts as the trigger, it is obvious that the latter directly or indirectly determines the cell lifetime.

The effect of phosphoric acid reduction on cell performance has been investigated also for phosphoric acid-type fuel cells. Fig.3.13 shows the results of an evaluation by Okae et al. of the amount of phosphoric acid evaporation as a function of cell temperature in a phosphoric acid fuel cell (PAFC) [12]. The evaporation rates estimated from Fig. 3.13 are 0.6, 1.8, and 9μgm^{-2} s^{-1} for cell temperatures of 150, 170, and 190℃, respectively.

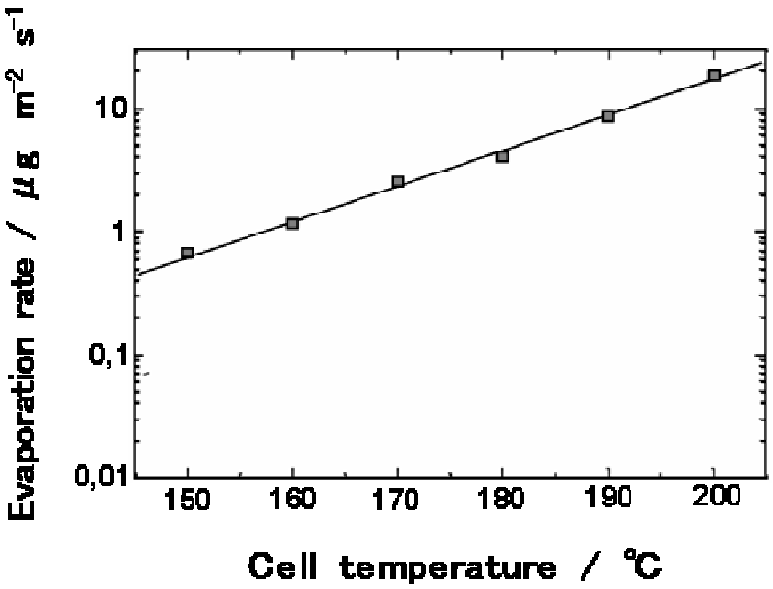

Fig.3.13 Phosphoric acid evaporation rate as a function of temperature, from Ref. [12].

Fig.3.14 shows the weight of evaporated acid per unit area as a function of time, calculated from the data of Fig.3.13, overlaid with the time dependence of the voltage drop at 0.2Acm^{-2}, based on the data of Fig.3.4. The cell voltages shown here represent those values that had dropped by 10% from the peak voltage. However, since the cell operating at 150℃ was still generating power, the plotted data corresponds to lower voltage drops. It can be seen that the phosphoric acid depletion rate and the cell voltage reduction rate are in good agreement, regardless of cell temperature. Thus, even though the initial reduction of cell voltage is thought to be caused by the increase in the catalyst particle size, the depletion of phosphoric acid has a substantial effect on the cell voltage over the entire lifetime of the cell. The fact the voltage drop in the 150℃ cell was still less than 7% after

16,000 h operation suggests that the cell remains functioning by use of its remaining volume of phosphoric acid.

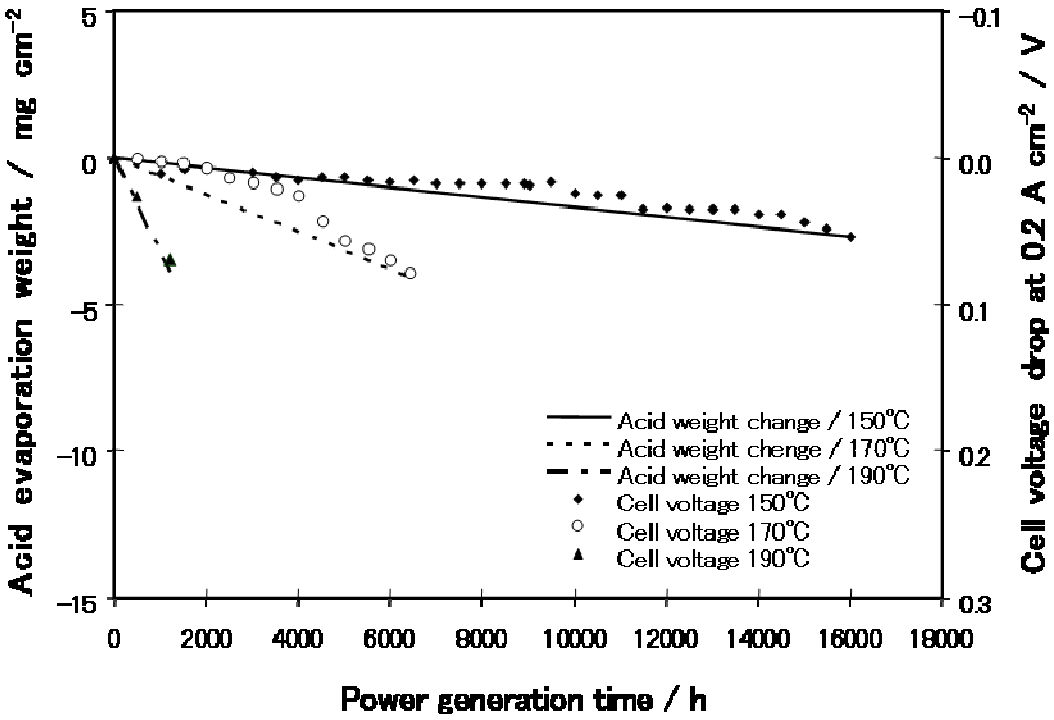

Fig.3.14 Relationship between the acid weight change by evaporation and the cell voltage drop. Solid, dotted, dot-dashed lines show the acid weight changes calculated for cell temperatures of 150, 170, and 190℃, respectively. Solid symbols (□, ○, ▲) indicate the cell voltage drops at 0.2cm^{-2}.

3.4 Conclusions

For HT-PEMFCs using PBI membranes doped with phosphoric acid, the effects of cell temperature on cell performance and durability were evaluated by long-term durability tests at cell temperatures of 150, 170, and 190℃. Consequently, it was clarified that a higher cell temperature results in a higher cell voltage, but a shorter cell life. The reduction in cell voltage of approximately 20mV during the long-term power generation tests was considered to be caused both by aggregation of the electrode catalyst particles in the early stages of operation, in addition to the effects of crossover due to the depletion of phosphoric acid in the terminal stage, the latter regardless of cell temperature. However, the cell operating at 150℃ was still generating power after 16,000h, and it is expected that enhanced long-term durability for practical applications can be achieved through effective management of phosphoric acid transfer.

References

[1] Y. Zhai, H. Zhang, G. Liu, J. Hu, B. Yi ; J. Electrochem. Soc. 154 (2007) B72.

[2] J. Hu, H. Zhang, G. Liu, B. Yi ; Hydrogen Energy 31 (2006) 1855.

[3] G. Liu, H. Zhang, J. Hu, Y. Zhai, D. Xu, Z. Shao ; J. Power Sources 162 (2006) 547.

[4] Y. Zhai, H. Zhang, D. Xing, Z.G. Shao ; J. Power Sources 164 (2007) 126.

[5] Y. Oono, A. Sounai, M. Hori, ;J. Power Sources 189 (2009) 943.

[6] J. Yu, Y. Yoshikawa, T. Matsuura, M.N. Islam, M. Hori ; Electrochem. Solid-State Lett. 8 (3) (2005) A152.

[7] J. Yu, T. Matsuura, Y. Yoshikawa, M.N. Islam, M. Hori ; Electrochem. Solid-State Lett. 8 (3) (2005) A156.

[8] J. Zhang, Y. Tang, C. Song, J. Zhang ;J. Power Sources 172 (2007) 163.

[9] N.H. Jalani, M. Ramani, K. Ohlsson, S. Buelte, G. Pacifico, R. Pollard, R. Staudt, R. Datta ; J. Power Sources 160 (2006) 1096.

[10] Z. Qi, S. Buelte, J. Power Sources 161 (2006) 1126.

[11] Y.L. Ma, J.S. Wainright, M.H. Litt, R.F. Savinell ; J. Electrochem. Soc. 151 (2004) A8.

[12] I. Okae, S. Kato, A. Seya, T. Kamonoshita ; The Chemical Society of Japan 67th Spring Meeting, 1990, p. 148.

Chapter 4

Evaluation for sintering of electrocatalysts and its effect on voltage drops in HT-PEMFC

4.1 Introduction

To date, reports have dealt with the relationship between operating temperature and cell durability for about 500h, including the catalyst stability at around 150℃ [1-6]. PEMFC is required to operate for over 5,000h for vehicular and 40,000-90,000h for stationary cogeneration systems. Therefore, it is essential for the reliability of the fuel cell system to evaluate quantitatively the performance degradation. Because it takes experimentally a lot of time to evaluate irreversible deterioration phenomena, it is after 40,000-90,000h that one can confirm whether the electrocatalysts can survive. In order to save the cost of long test times, theoretical evaluation schemes have been presented by now.

For example, numerical 1D non-isothermal models [7-9], 2D steady-state isothermal and transient nonisothermal models [10-12], and 3D steady and unsteady state models [13-16] for HT-PEMFC has been proposed. However, the main problem with all of these models is the assumption that proton conductivity is constant, which has shown to vary with both relative humidity and temperature [8,9,13]. While the previous HT-PEMFC models have been helpful to understand the effects of various operating conditions such as temperature and pressure on cell performance, none have focused on predicting theoretically the deterioration mechanisms. Through them the morphological properties of the aging CL where Pt sintering or phosphoric acid loss can be seen, which has the possibility of great impact on the gradual progress of oxygen reduction reactions (ORR) and gradual cell performance over time.

The other methodology is dealing with small areas by the ab initio method which forces one to develop a model composed of a few numbers of atoms due to the high computational demand. Temperature is hard to consider in the ab initio computation method, and the static Monte Carlo method lacks of the factor of time. Nevertheless, both are indispensable factors to discuss the phenomena of durability.

Therefore, quantitative estimation of the catalyst decay for longer time scale with considering the temperature and its effect on the performance

were theoretically investigated. The electrocatalysts for fuel cell must be designed with high durability in order to guarantee the required lifetime of the system. It is desirable to know the degree of deterioration of the catalysts prior to trial-and-error manufacturing of electrocatalysts and long-term experimental durability testing. Theoretical studies need not only to estimate before-and-after size or shapes of aging electrocatalysts, but also to explain the correlation between the deterioration progress in the catalyst and the influences on the cell performance with elapsed time. Practical theoretical studies enable to accelerate the development of electrocatalysts with reducing cost. For practical application as mentioned above, more long-term evaluation is needed.

Multi-scale modeling presented in this study allows barrier-free access to both the catalyst condition and to the fuel cell system. It enables us to investigate various phenomena in different scales, which are composed of atomic electrocatalysts model of much more than several square nm area, particle-based electrocatalysts of submicron area, and the catalyst layer (CL) in the fuel cell with 20μm-area. The phenomena in each area can be solved by different methods with considering temperatures. First, the Ultra Accelerated Quantum Chemical Molecular Dynamics (UA-QCMD) was applied to clarify the energetic or electronic structures of electrocatalysts. Secondly, the three-dimensional kinetic Monte Carlo (3D-KMC) method [17-19] was developed and applied to trace the progress the sintering of electrocatalysts over time. At third, in order to predict the impact of the morphological change over time inside of the CL on voltage loss, algorithms of polarization loss was developed and applied. Accordingly, the results of the catalytic morphological changes obtained by 3D-KMC could be reflected in the voltage calculation scheme, and the morphologically affected cell performance could be theoretically evaluated.

The influences of aging time and operating condition on the performance of HT-PEMFC were theoretically evaluated. It includes quantitative estimation of how much sintering of supported metals occurring in the CL of HT-PEMFC. The effects of temperature on sintering of nanoparticles of electrocatalysts, cell voltage, and durability were theoretically evaluated by executing long-term durability simulation of the fuel cells. Simulated results were compared with the measured results of experimental durability tests of HT-PEMFC using PBI-H_3PO_4 membranes for cell temperatures of 150˚C, 170˚C, and 190˚C [20]. The deterioration mechanism of the cells was also

theoretically investigated based on the time variations of cell voltage and internal cell resistance during the durability tests, and was confirmed by post analysis TEM observations.

4.2 Experimental and model development

4.2.1 Experimental

In most PEMFC, the gas diffusion layer (GDL) consists of two different domains: a 200-300μm thick carbon fiber-based macro-porous layer, and a 20-40μm thick carbon black-based microporous layer (MPL). In this study, a sheet of carbon paper with a thickness of 280μm , high porosity (78%) [21], and large pore size (around 20-40μm) [21,22] (Model No. TGP-H-090, Toray Industries, Inc.) was used as a GDL. Z. Fishman indicated that the pores in GDL were typically about 20μm in diameter, and occupied most of the GDL volume [21]. Flückiger indicated in the pore size distribution of TGP-H-060 which has very similar structural parameters to TGP-H-090 was about 20μm [22]. The structural parameters for the GDL are summarized in Table 4.1. A catalyst ink was then prepared by mixing polyvinylidene fluoride (PVDF; Kureha Corp., Japan) and 46.8 wt% Pt supported on Ketchen Black powder (carbon/metal:50/50, TKK Corp., Japan) [23]. After the electrode was prepared, the electrodes and H_3PO_4-doped PBI membrane were assembled in a unit cell assembly. Prior to use, the PBI membrane was immersed in 85% H_3PO_4 to obtain proton conductivity, and then the unit cell was installed in the fuel cell test platform. The cell was operated at 150, 170, and 190˚C, and 1.0atm pressure, and the current density was maintained at 0.2Acm^{-2} for long-durability tests. After the long-term power generation tests, TEM observations were carried out on both the as-prepared electrode catalysts and those following testing for about 1,000h at 150˚C and 190˚C for post-analysis. The rate of decrease in cell voltage was also measured for three different temperatures: 150˚C, 170˚C, and 190˚C.

Table 4.1 Structural parameters of the GDL of HT-PEMFC [21-23]

GDL structural data	Numerical values
Porosity ε [−]	0.78
Thickness, L_{GDL} [μm]	280
Mean pore diameter [μm]	20

4.2.2 Quantum chemical method

Since ab initio quantum chemical calculations are computationally intensive and very time consuming. Ab initio quantum chemical methodologies can evaluate electronic properties with only small cluster-sized molecules due to their heavy computational load; they cannot be applied to the large atomic scale or include thermal dynamics. This means that semi-empirical quantum chemical methods have to be employed. However, in order to achieve the required accuracy, it is necessary to use certain parameters, such as the exponent of a Slater-type atomic orbital (AO) in Eq. (4-7) and valence-state ionization potentials (VSIPs) in Eq. (48). By this technique, without heavy computational load, the Ultra Accelerated Quantum Chemical Molecular Dynamics (UAQCMD) can calculate the electronic configuration and investigate the affinity of Pt electrocatalysts on the surface of carbon support under three different temperatures, 150˚C, 170˚C, and 190˚C.

UA-QCMD has proven to be a very successful technique for providing a detailed understanding of diffusion or aggregation processes involving metal clusters, allowing us to explore cluster evolution and understand the behavior of supported and unsupported metal clusters at the atomic level by reflecting binding energies and charges based on quantum calculations. The electronic configurations of catalysts were calculated after UA-QCMD simulation by original Tight-Binding Quantum Chemical (TBQC) calculation.

Dynamics of the atoms were carried out using the following potential functions, which were employed to consider the ionic, covalent, and weak Vander Waals interactions among atoms.

$$U=\sum_i\sum_{j>1}\left[\frac{Z_iZ_je^2}{R_{ij}}+f_0(b_i+b_j)\exp\left(\frac{a_i+a_j-R_{ij}}{b_i+b_j}\right)\right] + \sum_i\sum_{j>1}D_{ij}\left[\exp\{-2\beta_{ij}(R_{ij}-R_0)\}-2\exp\{-\beta_{ij}(R_{ij}-R_0)\}\right] \quad (4\text{-}1)$$

The first term corresponds to the Coulomb potential, and the second term corresponds to the short-range exchange-repulsion potential (f_0 is the constant for unit adjustment, a is the size, and b is the stiffness), which gives a good account of the repulsive interactions arising from the overlap of electronic clouds. Z_i and Z_j are the charge of atoms, e is the elementary charge, and R_{ij} is the internuclear distance. The third term in Eq. (4-1)

corresponds to the Morse-type potential, which represents covalent interactions, where D_{ij} is the bond energy, β_{ij} is the form factor, and R_0 is the bond length at minimum energy. Using the described potentials, a classical molecular dynamics (MD) simulation [24] was performed. This system can solve the motion of equation for large sets of atoms. In this MD simulator, a Verlet algorithm [25] was employed to integrate equations of motion. Moreover, the temperature scaling method was implemented in the system, which is similar to the Woodcock algorithm [26]. MD simulations were carried out with 0.1 fs of integration time for the equations of motions.

This UA-QCMD method consisted of two parts. The first part was a TBQC calculation, and the second involved the classical MD simulator [24]. To reflect the Morse-type function and the atomic charges into during the MD simulation process, TBQC calculations were performed at the beginning, and again after UA-QCMD simulation. In this method, an electronic structure calculation was performed by solving the Schrödinger equation, $HC = \varepsilon SC$ (H, C, ε, and S refer to the Hamiltonian matrix, eigenvector, eigenvalues, and overlap integral matrix, respectively), with the diagonalization condition ($C^T SC = I$; I refers to the identity matrix). In order to determine the off-diagonal elements of H and H_{rs}, the corrected distance-dependent Wolfsberg-Helmholtz formula, Eq. (4-2) was used:

$$H_{rs} = \frac{K}{2} S_{rs} (H_{rr} + H_{ss}) \tag{4-2}$$

In the TBQC scheme, the total energy of a system, *E*, is expressed by using the following equation:

$$E = \sum_{k=1}^{occ} n_k \varepsilon_k \sum_i \sum_{j>1} \frac{Z_i Z_j e^2}{R_{ij}} + \sum_i \sum_{j>1} (b_i + b_j) \exp\left(\frac{a_i + a_j - r_{ij}}{b_i + b_j}\right) \tag{4-3}$$

Summing up the values of b_i, b_j and a_i, a_j, we can modify Eq. (4-3) as follows:

$$E = \sum_{k=1}^{occ} n_k \varepsilon_k + \sum_i \sum_{j>1} \frac{Z_i Z_j e^2}{R_{ij}} + \sum_i \sum_{j>1} b_{ij} \exp\left(\frac{a_{ij} - R_{ij}}{b_{ij}}\right) \tag{4-4}$$

where the first, second, and third terms on the right-hand side refer to the molecular orbital (MO) energy, Coulombic energy, and exchange-repulsion energy, respectively. The first term on the right-hand side of Eq. (4-4) is rewritten as follows:

$$\sum_{k=1}^{occ} n_k \varepsilon_k = \sum_{k=1}^{occ} \sum_{r} n_k (C_{kr})^2 H_{rr} + \sum_{k=1}^{occ} \sum_{r} \sum_{s} n_k C_{kr} C_{ks} H_{rs} \qquad (4\text{-}5)$$

where the first and second terms on the right-hand side refer to the one-electron contribution to the binding energy and the two-electrons contributions to the binding energy, respectively (n_k is the number of electrons occupied in the kth molecular orbital). A binding energy calculated from the second term of Eq. (4-5) is used for the determination of the D_{ij} parameter in Eq. (4-1).

In order to set the Hamiltonian matrix, *H*, and overlap the integral matrix, *S*, in the TBQC scheme, exponents of a Slater-type AO, denoted as ζ_r, and VSIPs for the valence shell of calculation atoms must be optimized. The former parameters are used to calculate the *S* matrix and H_{rs} in Eq. (4-2). The latter ones are used for the diagonal element of *H* (Hrr or Hss in Eq. (4-2)).

The relationship between H_{rr} and VSIP of the rth AO of the ith atom (I^i_r) is described as $H_{rr}=-I^i_r$. These two parameters in the TBQC scheme were represented by the polynomial functions of atomic charges. The ζ_r and H_{rr} terms were calculated by the polynomial functions of atomic charges described below by Eqs. (4-6) and (4-7), respectively.

$$\zeta_r = s_0 + s_1 Z_i \qquad (4\text{-}6)$$

$$H_{rr} = h_0 + h_1 Z_i \qquad (4\text{-}7)$$

In Eqs. (4-6) and (4-7), Z_i corresponds to the atomic charge on atom *i*. The parameters regarding ζ_r, i.e., s_0 and s_1 in Eq. (4-6), and those regarding H_{rr}, i.e., h_0 and h_1 in Eq. (4-7), were adjusted to reproduce the binding energies and electronic structures of each reactant obtained by first principle calculations; these are summarized in Tables 4.2 and 4.3, respectively.

Table 4.2 Coefficients of a single zeta parameters in a Slater-type atomic orbital in Eq.(4-6).

Element	AO	S_0	S_1	Coefficient
C	s	2.40	1.0	1.0
	p	2.20	1.0	1.0
Pt	s	2.30	1.0	1.0
	p	1.95	1.0	1.0
	d	2.90	1.0	1.0

Table4.3 Coefficients of the H_{rr} parameters in Eq.(4-7).

Element	AO	h_0	h_1
C	s	-10.80	-9.50
	p	-8.40	-9.00
Pt	s	-8.0054	-6.049
	p	-3.9076	-7.5238
	d	-9.500	-8.1900

4.2.3 Estimation of sintering of electrocatalysts by 3D kinetic Monte Carlo method

Since the conventional static Monte Carlo method cannot consider a real-time scale, the sinterability of supported nanoparticles, which might affect the voltage drop was simulated by a 3D kinetic Monte Carlo (3D-KMC) method. The 3D-KMC simulation proceeds by repeating a series of sintering events for a determined number of particles in the supports and supported Pt electrocatalysts for a determined number of steps. It considers both indispensable factors for the thermal durability of catalysts, “time” and “temperature”. The coordinates outputted by the system are then used to map the sintering processes of the supported Pt metal catalysts. This enables a comparison of the characteristics of the sintering process of supported precious metals with experimental results. Previous studies [17-19] show not only quantitative comparison in grain growth of metal oxide supports, alumina, zirconia and ceria, but also sintering degrees of supported Pt showed good agreement with experimental results by comparing particle distribution. During the simulation, a diffusion direction is randomly generated, while the diffusion length for one 3D-KMC step, l, is calculated as $l=(D(r)\Delta t)^{-0.5}$, where D(r) and Δt are the diffusion coefficient

given as a function of particle size and the real-scale diffusion time per one 3D-KMC step, respectively. At the initial stage of sintering, adatoms diffuse, meet, and nucleate into larger atomic islands.

$$D_M(r) = D_{M0}(2r_M)^{-n}\exp\left(-\frac{E_M}{RT}\right) \quad (4\text{-}8)$$

$$D_S(r) = D_{S0}(2r_S)^{-n}\exp\left(-\frac{E_S}{RT}\right) \quad (4\text{-}9)$$

T, *R*, and *n* denote the absolute temperature, the gas constant, and the particle size-dependent coefficient of diffusion of supported metals or supports, respectively. D_{M0} denotes the pre-factor of diffusion coefficient of supported metals.

The sintering dynamics simulator enables the reflection of atomic scale characteristics, such as the diffusivity of supported electrocatalysts. In fact, such atomic scale characteristics are significantly related to the macroscopic migration characteristics of supported metals. Therefore, the thermal diffusivity, as two Arrhenius equations (4-8) and (4-9), were calculated based on the TBQC calculation program. The activation energy for sintering of the supported metal diffusion, E_M, was calculated from intra metal-metal binding energies of supported metals. The nanoparticle size of electrocatalysts, r_M, and the support size, r_S, at a certain time were reflected into Eqs. (4-8) and (4-9). In Eq. (4-8), diffusion coefficients of electrocatalysts were determined based on the quantum chemical calculation using the self-diffusion coefficient of metals [27]. The diffusion coefficient of graphite carbon support in Eq. (4-9) was determined based on experimental data [28].

In the environment of phosphoric acid, the principal corrosion reaction of carbon is assumed a four-electron corrosion process as follows,

$$C + 2H_2O \rightarrow CO_2 + 4H^+ + 4e^-$$

In that case, the percent weight loss ΔW_t were calculated as follows by Antonucci et al. [29],

$$\Delta W_t = \frac{k}{1-n}t^{(1-n)} \times \frac{M_c}{4F} \times 100 \quad (4\text{-}10)$$

where M_c is the atomic mass of carbon and F is the Faraday's constant, 96,487 C mol^{-1}. Based on the result of electrochemical corrosion in the 85% phosphoric acid, the weight loss of the carbon are different depending on the specific surface area of the carbon. Corrosive model was reflected by taking the parameters, n=0.30, k=0.44$Ag^{-1}s^n$, when the surface area is around 60 m^2g^{-1} [29].

4.2.4 Modeling of the cathode catalyst layer

The membrane-electrode-assembly (MEA) is the heart of a fuel cell. This consists of several elements that are susceptible of being studied for optimization of a fuel cell's performance. One such element is the CL, in which the electrochemical reactions occur, and whose formulation must be optimized in order to improve the performance of the PEMFC. Ferreira et al. [30] demonstrated that the electrochemical surface area loss of Pt at the cathode was much larger than that at the anode. Pt coarsening occurred even at low temperature in PEMFC, and Pt nanoparticles in the cathodes were clearly much larger than those in the anodes [31]. In the case of the PEMFC, polarization losses on the anode side, or the hydrogen electrode, are negligibly small [32]. Choudhury also used the mathematical model of the CCL to investigate the potential drop in the case of phosphoric acid fuel cells (PAFC) [33].

Therefore, the 3D CCL model of the HT-PEMFC was constructed for the present study. The 3D CCL modeled structure contains three phases: the gas phase (pores), the H_3PO_4 thin electrolyte phase (hot phosphoric acid), and a phase consisting of a random distribution of carbon-supported nano-sized electrocatalysts (Pt/C), which were generated using a Monte Carlo method. In reality, there is an acid electrolyte thin film surrounding the catalyst particles, and mass transport through this phase is much slower than a porous media. Reactant gas dissolves in the electrolyte media and diffuses through this film to reach the catalyst sites [13]. The schematic modeling procedure and its algorithm with detailed schematic drawings were described in our previous studies [34-36]. In the modeling, the carbon support is considered as a particle; in fact, carbon supports usually constitute particle-like structures, and the H_3PO_4 thin film covers the surface of the carbon particles. Each of the nanoparticles of electrocatalysts was assumed to be supported on the surface of a carbon particle, with 50% of its volume buried. Hence, the other half of its volume was exposed and

had an active surface area only when it could successfully make contact with three kinds of mass flow: the proton through the electrolyte, the electron through the carbon, and the reactant O_2 gas through the pores. Active supported catalysts were determined by checking three-dimensionally whether the exposed catalysts made contact with the required protons, electrons, and reactant O_2 gas. Whether every nanoparticle among all supported electrocatalysts could be active or inactive was visually checked by marking with different colors. Active catalysts were colored gold, and inactive catalysts were colored wine red.

In the CCL, the dispersed catalyst (Pt/C) formed agglomerates with the electrolyte fill. These domains were surrounded by channels through which the reactant gases diffused. Therefore, the gas diffusion inside of the pores in the constructed CCL was taken into account.

The mass-balance in the CCL is expressed by the following equation

$$\varepsilon_H + \varepsilon_P + \varepsilon_C = 1 \tag{4-11}$$

where the sum of the H_3PO_4 volume fraction, ε_H, was assumed to be thin layer, the pore space volume, ε_p, was maintained at approximately 0.475 throughout the thickness of the CCL [37], and the volume fraction of electrocatalysts (Pt/C) dispersed carbon, ε_c was equal to 1. The average thickness of the CCL was set to be 20μm, which is consistent with the thickness of experimentally used CCL [23]. The electrocatalyst (Pt/C) dispersed carbon volume fraction, ε_C, was determined from Eq. (4-11) [38]:

$$\varepsilon_C = \frac{m_{Pt}}{L}\left\{\frac{1}{\rho_{Pt}} + \frac{1-(\%_{Pt})}{\rho_C(\%_{Pt})}\right\} \tag{4-12}$$

where ρ_{Pt} and ρ_C are the mass densities of the Pt electrocatalysts and carbon black, respectively. $\%_{Pt}$ represents the mass percentage of Pt electrocatalysts supported on the carbon surface. Pt nanoparticles were supported on the surface of carbon particles until they satisfied the loading of catalysts, 46.8wt% which is consistent with actual experimental loading value. Subsequently, the modeling simulator chose the largest particle among the remaining particles and randomly inserted the particle into the simulation cell. Lobato et al. measured the value of porosity (%) for different Pt percentages -20, 40, and 60% Pt/C in the CL- which ranged from 55.3,

57.9, and 60.1, respectively [37]. Therefore, the simulator repeated this process until it became close to the value of Lobato's experimentally measured porosity [37], 55% (as the structural parameters of the CCL given in Table 4.4). Overlaps between particles in the simulation cell were accepted up to a maximum overlap ratio given of 0.8. After determining the coordinates of the carbons and H_3PO_4, there were additional subroutines to search three-dimensionally the spatial distributions of active electrocatalysts that could promote ORR, and to calculate the active specific surface area inside of the microstructure of the constructed model. At that time, all nanocatalyst particles could be classified as either active or inactive by this routine. Here, "active" refers the nanoparticles of electrocatalysts that were supported on effective particles of carbon forming electron current paths, and were effectively covered by electrolyte, forming proton current paths. The subroutine regarded carbon particles that were interconnected from the GDL-MPL side, and electrolyte that was interconnected from the PBI-H_3PO_4 membrane side, as effective carbon particles and effective electrolyte, respectively. The GDL-MPL side and the PBI-H_3PO_4 membrane side were defined as the left and right planes of the constructed 3D model, respectively, as shown in Fig.4.1. On the left boundary, protons migrated into the CCL through free H_3PO_4 from the PBI-H_3PO_4 membrane, whereas at the right boundary, oxygen and electrons were transported into the layer through the GDL-MPL side.

Table 4.4 Structural parameters of the CCL of HT-PEMFC

CCL structural data	Numerical values
Porosity	0.48
Density of carbon	2.0 g cm^{-3}
Density of PBI-H_3PO_4	1.6 g cm^{-3}
Density of Pt	21.5 g cm^{-3}
Catalyst layer thickness, L_{CCL}[μm]	20.0[31]
Loading catalyst amount (pt)	46.8 wt%
Catalyst utilization (%)	22%

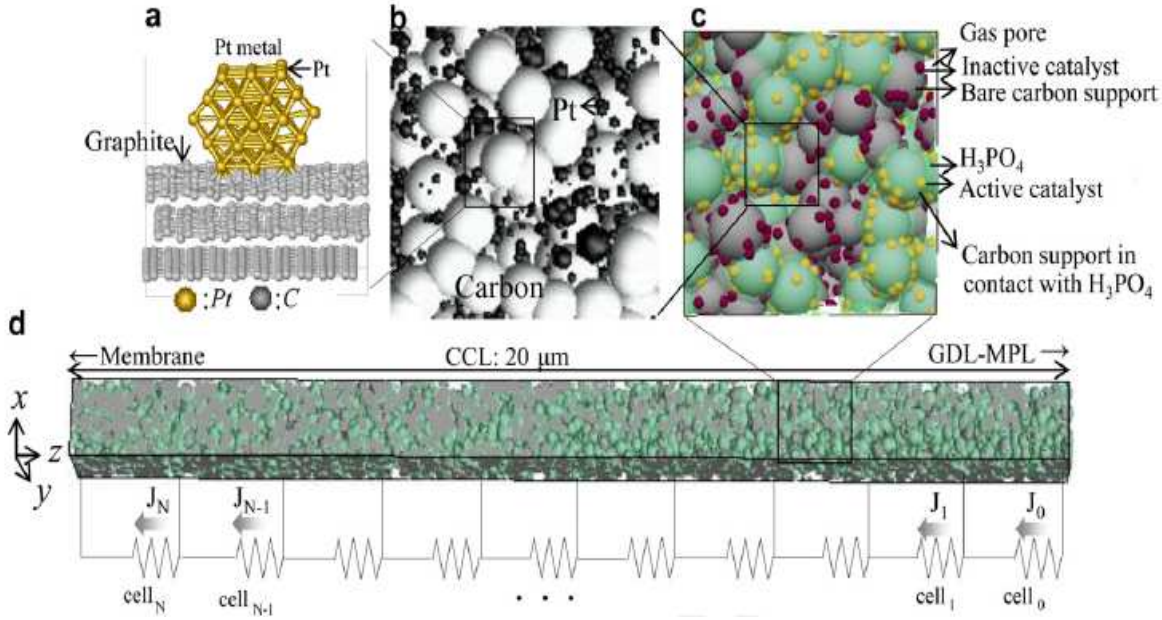

Fig.4.1 Application of multi-scale modeling to HT-PEMFC
(a) Microscopic model for investigating the affinity of electrocatalyst and support by UA-QCMD method. (b) Particle-based submicron model to investigate sintering characteristics by 3D-KMC method. (c) Carbons, pores, active and inactive electrocatalysts and thin film of H_3PO_4 [23] in the CL. (d) The thickness of the modeled CL is 20μm [33]. The CL was divided into 10 cells, numbered N =1-10 for solving ORR reaction.

4.2.5 Tortuosity of gas flow in the catalyst layer

The size of pores existed in porous materials are never straight and uniform. The average speed of the gas flow is greater on a straight pore shape than a curved one. On the contrary, the gas flow in a highly complex and twisted pore system will experience more resistance to flow and therefore move at a slower rate. This means the tortuosity factor. A pore system with internal blockage or discontinuity will not transport gas efficiently. Porous materials with small pores have a greater tortuosity. The tortuosity τ of a pore network in the porous CL is the result of the merging, branching, and curving of pores. The tortuosity value is dependent on composite properties such as the phase fractions, interfacial surface area, and geometric properties. Generally, the diffusivity and permeability decrease with increasing tortuosity [39]. In this study, the tortuosity value could be theoretically determined nondestructively by the 3D random walk simulation algorithm, which counted respective pore voxels that formed several tortuous paths in the modeled 3D CL [39]. Cut voxels are therefore shaped and arranged as a simple cubic lattice. The 3D pore connectivity was

examined in order to output a 3D image of tortuous paths in Fig.4.2 (a)-(c), and the numerical value of tortuosity. When a pore voxel was in full contact with another voxel, the two voxels were judged to be connected. Some pores in the porous media were three-dimensionally connected to form a single large percolation cluster responsible for the macroscopic transport of reactant gases; other pores were isolated and did not contribute to the macroscopic diffusion and the Darcy flow. The tortuosity value of a 3D pore network was computed in a unit cell. In the case where each unit cell size of a unit cell was 1.0×1.0×20.0μm, the constructed CCL model was finely cut into 100.0×100.0×2000.0 meshes in the x-, y-, and z-directions, respectively. Each cut voxel in the porous media was numbered and classified as a pore,

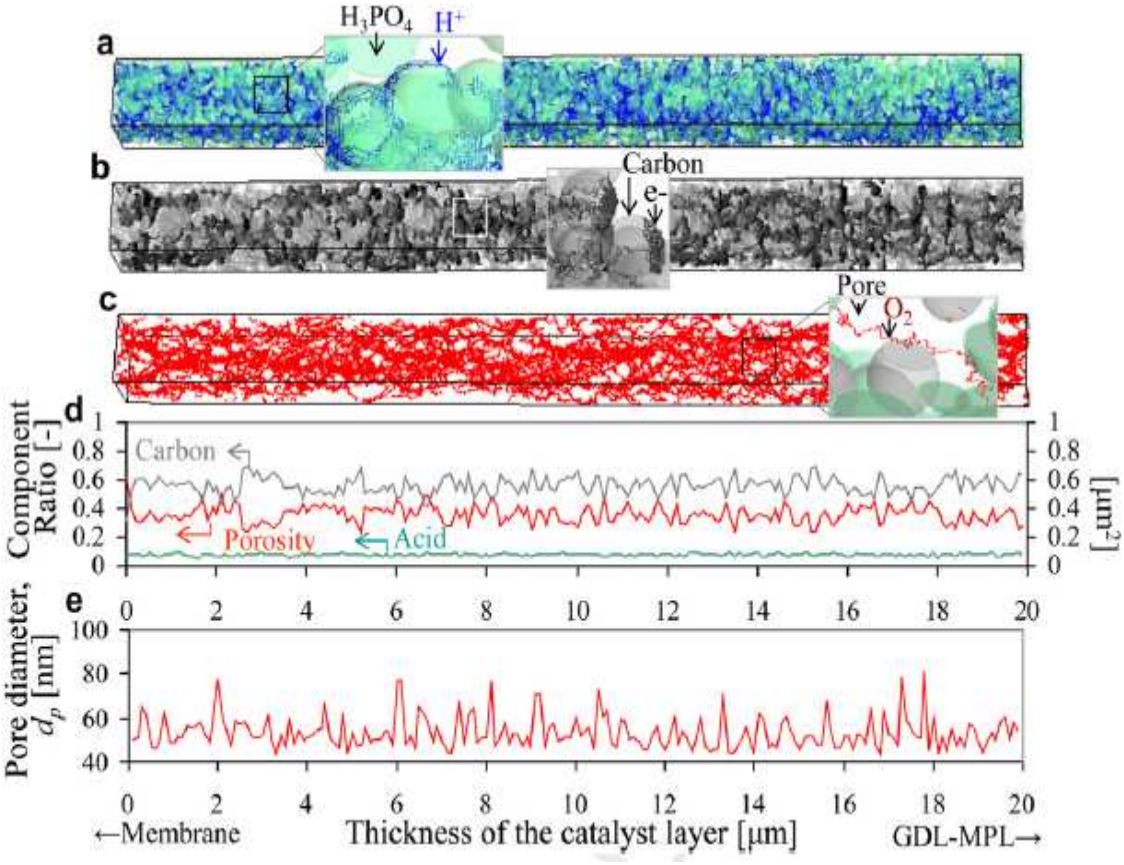

Fig.4.2 Application of multi-scale modeling to HT-PEMFC
(a) 3D view of tourtuous proton-conducting trajectories (blue lines) in connected electrolytes. (b) 3D view of electron-conducting trajectories (black lines) in electrically connected carbon medium. (c) 3D view of tortuous gas diffusion trajectories (red lines) in connected pores. (d) Component ratio of pore, carbon and acid in the CL [−] thorough in the catalyst layer. (e) Local mesopore diameter, d_p [μm] throughout the catalyst layer.

carbon, or phosphoric acid electrolyte by judging whether the center of the voxel was positioned in a pore, a carbon, or an electrolyte. The tortuosity value τ was roughly estimated to be 1.5 in most publications [48]. Tortuosity is defined as the ratio of the actual distance of the mass flow in the CL, L_c, to the gas flow in free space, L_f. Connected pores in the electrode form continuous paths for gas flow, and we measured the tortuosity value by calculating the following ratio:

$$\tau = L_c/L_f \left(\lim_{\varepsilon \to 1} \tau = 1, \quad \tau^2 \geq 1 \right) \tag{4-13}$$

Finally, $\tau \to \infty$ only if porosity, $\varepsilon \to 0$; i.e., the tortuosity is finite only if the pore space disappears. This means that the actual average path traversed by the species while diffusing in the interstitial mass flow in a porous medium is longer than in the absence of the solid. This implies that there is no hindrance to diffuse in the absence of an impermeable solid.

4.2.6 Gas diffusion in the catalyst layer

A series of mass transport and electrochemical equations were solved to obtain the polarization characteristics. The constructed model took into account the mass-transport phenomena caused by multicomponent gas diffusion through the CCL. The oxygen flux, N_{O2}, through the CL was assumed to be driven by a concentration gradient. It was thus determined by Fick's law for the diffusion of the gas component, which could be described as follows:

$$\frac{dc^{i}_{O_2}}{dx} = \frac{N_{O_2}}{D^{eff}_{O_2,i}} \tag{4-14}$$

Here, C_{O2} represents the oxygen concentration, which can be expressed as follows by considering molecular diffusion and Knudsen diffusion [41,42]. The effective oxygen gas diffusion coefficient, $D^{eff}_{O2,i}$ in the CCL, corrected for the porosity ε and tortuosity τ of the CCL, and is related to the Knudsen diffusion coefficients, $D_{kn,i}$ and D_{O2} . The values for the local factor ε / τ (direction and compression dependence) were taken from experimental electrochemical diffusometry measurements [30].

$$D^{eff}_{O_2,i} = \frac{\varepsilon}{\tau} \times \frac{1}{(1/D_{O_2} + 1/D_{kn,i})} \tag{4-15}$$

D_{O2} is the molecular diffusion coefficient (cm^2s^{-1}) of O_2 in the pores. D_{kn} is

the Knudsen diffusion coefficient (cm^2s^{-1}) for the porous structure. Because the Knudsen effect is dependent on the temperature and molecular weight, three kinds of temperatures, T =423K (150˚C), 443K (170˚C), and 465K (190˚C) were set as cell test conditions, and the oxygen molecular weight, M_{O2}=32$gmol^{-1}$ was also set. The value of d_p was the mean pore diameter in the CCL, but the value changed locally somewhat through CCL thickness from the PBI-H_3PO_4 membrane side to the MPL-GDL side. In fact, the local mesopore diameter size was calculated to introduce the value in Eq. (4-16) using a scanning technique, as shown in Fig.4-2(e). The values were reflected to compute mass flow through the thickness of the CCL. According to the IUPAC classification, macropores were defined as pores of more than 50nm, and mesopores as being from 2 to 50nm. Lobato et al. showed that the majority of pore ranges could be seen from 50 to 120nm by Hg-porosimetry of the electrodes with different Pt content on the carbon support, such as 20, 40, and 60% Pt/C [37]. Theoretically estimated average pore diameter was 53.3nm, and the range was from 42.9 to 97.8nm, which agreed with Lobato's experimental mesopore range, as mentioned above. Power generation characteristics were obtained by substituting local $d_{p,i}$ directly into Eq. (4-16), which expresses the Knudsen diffusion coefficient of cell i, D_{kn}.

$$D_{kn,i} = \frac{d_{p,i}}{3}\langle v \rangle = \frac{d_{p,i}}{3}\sqrt{\frac{8RT}{\pi M_{O_2}}} \qquad (4\text{-}16)$$

Oxygen utilization rate, U_{ox} in Table 4.5 was incorporated to determine the utilization rate of oxygen in total feed air from the inlet side to outlet side of the CL.

Table 4.5 Cell operating conditions of HT-PEMFC.

Operating condition	Numerical values
Relative humidity [-]	0.0
Atmospheric pressure [atm]	1.0
Pressure at the cathode gas inlet[atm]	1.0
Feed gas	Air
Nitrogen/oxygen mole fraction ratio of feed gas	0.79/0.21
Cell temperature [˚C]	150, 170, 190
Oxygen utilization [%]	27
The reference concentration of oxygen[$molm^{-3}$], C^{ref}_{O2}	0.107[11]

The GDL effective diffusivity was assumed to be isotropic and to follow the Bruggeman relation [48]:

$$\text{In GDL,} \quad D_{O_2}^{eff} = D_{O_2}\varepsilon_{GDL}^{1.5} \tag{4-17}$$

where the effective diffusion coefficient, D^{eff}_{O2}, was used to account for oxygen gas diffusion in the gas mixture through the pore region of the GDL, and as a correction factor to account for the non-diffusing space occupied by the solid fragments

4.2.7 ORR and dissolved O_2

Numerical simulations were carried out for the fuel cell operation with conventional flow field and gas flow. The ORR kinetics followed the electrochemical Butlere-Volmer equation, as shown in Eq. (4-18). Current distribution was calculated according to Eq. (4-18). The solution algorithm for obtaining current distribution and polarization loss of this study was similar to one proposed by Hu et al. [43].

$$i_{r,i} = a_{cat}^{eff} i_0 \left\{ \frac{C_{O_2}^{dissolved,\,H_3PO_4}}{C_{O_2}^{ref}} \exp\left(\alpha_c \frac{nF}{RT}\eta_i\right) - \exp\left((\alpha_c - 1)\frac{nF}{RT}\eta_i\right) \right\} \tag{4-18}$$

where a^{eff}_{cat} is the effective catalyst surface, which is identified by yellow nanoparticles in Fig.4.1. η_i is the electrode activation overpotential. They can make contact with the carbon and electrolyte phase and be determined three-dimensionally. For typical cathode electrode structures, the percentage of effective catalyst nanoparticles is about 50% [48]. C^{ref}_{O2} is the reference oxygen concentration [14], the value of which is shown in Table 4.5, and i_0 is the reference exchange current density. The transfer coefficient ac is dependent on temperature and phosphoric acid concentration. The coupled set of Eq.(4-18) was solved iteratively, and the solution was considered to be convergent when the relative error in each field between two consecutive iterations was less than 0.05.

Various Tafel slopes have been reported for ORR in concentrated phosphoric acid [45-50]. Clouser et al. [45] studied the effect of temperature on ORR in phosphoric acid and obtained Tafel slopes. Each experimental measurement of the cathode transfer coefficient ac increased with temperature: 0.66 at 150˚C, 0.75 at 206˚C, 0.76 at 207˚C, and 0.81 at 251˚C(slope of $0.0014K^{-1}$). Appleby [46] reported the variation of the transfer

coefficient ac with temperature; values were from 0.49 at 25˚C to 0.562 at 95.9˚C on oxidized Pt in 85wt% phosphoric acid. Similarly, O'Grady et al. [47] reported values from 0.53 at 25˚C to 0.68 at 70˚C in 85wt% phosphoric acid and ac varied linearly with temperature with a slope of $0.0034K^{-1}$. Huang et al.[48] reported values of ac to be 0.47, 0.61, and 0.67 at temperatures 25, 100, and 150˚C, with a slope of $0.0016K^{-1}$. The rate change of the transfer coefficient with temperature has been reported for the ORR in phosphoric acid: α_C=0.662 (25˚C)−0.90 (136˚C), with a slope of $0.002K^{-1}$ on oxide-free Pt [49], and α_C =0.559(25˚C)−0.66(136˚C), with a slope of $0.001K^{-1}$ on active Pt [50].

The dependency of the transfer coefficient on temperature was averagely expressed in Eq.(4-18) as the function of temperature in degrees Kelvin.

$$\alpha_c = 0.0027T - 0.3486 \tag{4-19}$$

The cathodic exchange current density was expressed in Eq. (4-20) as a function of temperature [51],

$$i_0 = 1.3150 \times 10^{-8} \exp\left[\frac{72400}{R}\left(\frac{1}{423.15} - \frac{1}{T}\right)\right] \tag{4-20}$$

The dissolved oxygen concentration at the gas/phosphoric acid concentration interface was determined from the solubility of oxygen using Henry's law. $C_{O2}^{\text{dissolved H3PO4}}$ is the dissolved oxygen gas concentration in hot phosphoric acid, as determined by Henry's law [52]. $H_{O_2}^{\text{hot } H_3PO_4}$ is Henry's constant for the oxygen gas dissolution in hot phosphoric acid. $D_{O_2}^{\text{hot } H_3PO_4}$ is the diffusion coefficient for oxygen in hot phosphoric acid, and the following Eqs.(4-21)-(4-23) can reproduce the experimental data [53] for diffusivity and solubility of oxygen gas in hot phosphoric acid.

$$D_{O_2}^{\text{hot } H_3PO_4}\left(cm^2 s^{-1}\right) = 1 \times 10^{-4}\left(-2 \times 10^{-6} w_{H_3PO_4} + 0.0002\right) \exp\left[\frac{4.184\left(21.187 - 0.1548 w_{H_3PO_4}\right)}{RT}\right] \tag{4-21}$$

$$C_{O_2}^{\text{dissolved } H_3PO_4}\left(\text{mol m}^{-3}\right) = 50.189 \exp\left(-0.0509 w_{H_3PO_4}\right) \exp\left[\frac{-4.184\left(-0.0025 w_{H_3PO_4}^2 + 0.1578 w_{H_3PO_4} + 7.8421\right)}{RT}\right] \tag{4-22}$$

$$H_{O_2}^{\text{hot } H_3PO_4}\left(\text{mol m}^{-3}\ \text{Pa}^{-1}\right) = 101,325 \exp\left[\left(\frac{-1.27 \times 10^4 w_{H_3PO_4}^3 + 1.23 \times 10^4}{T}\right) 35.2 w_{H_3PO_4} - 46.6\right] \tag{4-23}$$

Here, w_{H3PO4} is an 85% concentration of hot phosphoric acid.

For the electrochemical reaction shown in Eq.(4-24), the thermodynamic open-circuit voltage (OCV) can be described by Eq.(4-25).Consequently, the thermodynamic OCV decreases with increasing temperature, especially above 100˚C, due to the increase of P_{H2O} [54]:

$$O_2+2H_2 \Leftrightarrow 2H_2O \quad (4\text{-}24)$$

$$OCV = E^0_{rev} + \left(\frac{\Delta S}{nF}\right)_P (T-298) + \frac{RT}{2F} \ln \frac{P_{H_2} P_{O_2}^{1/2}}{P_{H_2O}} \quad (4\text{-}25)$$

The temperature-dependent thermodynamic open-circuit voltage for the overall reaction (4-24) can be estimated using the relation shown by Eq. (4-26) [54,40]:

$$OCV = 1.23 - 0.9 \times 10^{-3}(T-298) + 2.3\frac{RT}{4F} \log \frac{P_{H_2}^2 P_{O_2}}{P_{H_2O}^2} \quad (4\text{-}26)$$

The cell voltage is given by Eq. (4-27):

$$E_{cell}=OCV-\eta_{ORR} \quad (4\text{-}27)$$

The saturation pressure of water, P_{sat}(Pa), can be expressed in the temperature range between 100 and 200˚C(the operating temperature range of HT-PEMFC) [52,53].

$$P_{sat}(Pa) = 0.68737\,T(K)^3 - 732.39\,T(K)^2 + 263,390\,T(K) - 31,970,000 \quad (4\text{-}28)$$

where the units of P_{sat} and T are Pa and K, respectively.

4.2.8 Proton conductivity

Since a series of the tests were conducted under dry conditions and used a PBI-H_3PO_4 membrane MEA, the proton conduction does not depend on water. In such a case, water content, expressed as the mole fraction of water/phosphoric acid for the dry conditions, can be regarded to be zero in the temperature range of 100˚C to 180˚C [55]. This is quite different from Nafion, which must be used below 100˚C. In that case, the numerical values of water content, expressed as moles of H_2O/moles of SO^{3-}, are higher than when a PBI membrane is used. Therefore, proton conductivity is not

dependent on water content, and the value in hot phosphoric acid is expressed by Eq. (4-29) [56]:

$$\sigma_{H_3PO_4}(S/cm) = 1.01365 - 1.21548 \times 10^{-2} W - (1.5447 \times 10^{-3} - 6.42463 \times 10^{-5} W)t \quad (^{\circ}C) \tag{4-29}$$

Here,W is the concentration of hot H_3PO_4, 84e94 wt%, and t is temperature in ˚C In the CL, the phosphoric acid is responsible for its proton conductivity. The proton is transported through the free phosphoric acid that comes from the membrane. The computation scheme of gas tortuosity, as shown in Eq. (12) was applied to estimate the tortuosity of a proton path in order to calculate the effective proton conductivity. The effective proton conductivity in the composites with a mixed conductive phase follows Eq. (4-30) [57], which was corrected by the tortuosity factor and the fraction of phosphoric acid in the CL:

$$\sigma^{eff}_{H^+,i} = \sigma_{H_3PO_4} \varepsilon^{\gamma}_{H,i} \tag{4-30}$$

where σ_{H3PO4} is the proton conductivity of phosphoric acid, ε_{H3PO4} is the fraction of phosphoric acid in the CL, and γ is the Bruggeman factor for proton path in the phosphoric acid and dependent on the amount of phosphoric acid. The proton current is governed by Ohm's law [58]:

$$i_2 = -\sigma \frac{d\Phi_2}{dx} \tag{4-31}$$

Where i_2 is the proton current density, Φ_2 is the electrolyte phase potential, σ is the proton conductivity, and x is the distance from the current collector.

4.2.9 Solving the electrochemical reaction scheme

The following assumptions were made in the development of the model to solve the electrochemical reaction scheme:

1. The system is isothermal and isobaric throughout the electrode.
2. The system is a steady-state operation.
3. Diffusion of O_2 in hot H_3PO_4 and pores was considered.
4. Gas component (O_2 and H_2O) sorption in the pores was considered.
5. The electrochemical reaction in the CCL occurred on the active catalyst

surface area.

6. The ORR generated only liquid-phase water.
7. Reactant gases and vapor were assumed to behave as ideal gases.
8. The gas permeability through the membrane was assumed to be negligibly small, such that gas cross-over could be neglected.
9. Because the electrode was very thin and its electronic conductivity was sufficiently high, the electronic phase potential was assumed to be uniform [59].

4. 3 Result and discussion

4.3.1 Model of cathode catalyst layer and electrocatalysts

Fig.4.1 shows a multi-scale modeling application to HTPEMFC. Fig.4.1 (a) shows a microscopic model to investigate quantum chemical characteristics of the catalyst itself, as well as the affinity of the supported catalyst and carbon support. Fig.4.1 (b) shows a particle-based submicron model used to investigate sintering characteristics by a 3D-KMC method. Fig.4.1 (c) shows the inactive electrocatalysts, bare carbon support, pores, active electrocatalysts, carbon supports in contact with H_3PO_4 and thin film electrolyte of H_3PO_4 [10,16,52] in the CL. Fig.4.1 (d) shows the modeled 3D cathode catalyst layer of the thickness of 20μm [23]. The modeling direction was shown as x-, y-, and z-directions. The size of each cell of the constructed model was 1.0(x-direction)×1.0(y-direction)×20.0(z-direction)μm, and the thickness of a CCL was 20.0μm. The constructed CCL model was finely divided into 100.0×100.0×2000.0 meshes in the x-, y- and z-directions, respectively. The constructed 3D model contained electrocatalysts on carbon supports in the CL, with the assumption of a thin film of H_3PO_4 as the electrolyte film. As noted by Horn [31], conventional PEMFC catalysts typically consist of Pt nanoparticles are dispersed on the surface of primary carbon particles of 20-50nm, which can form carbon particle aggregates of 100-300nm in diameter with electrically connected in 3D. Therefore, the size of primary particles was modeled by assuming around 40nm, which is mean value of the experimentally suggested value as mentioned above, and the specific surface area was $60 m^2 g^{-1}$. The phosphoric acid in the CL was ununiformly distributed to cover carbon particles in the model. The thickness of phosphoric acid was ranged from 7nm to 10nm. Simulated tortuosity in the phosphoric acid, 1.8, which matched with the value 1.8,

presented by Liu et al. [60]. Liu et al. presented the tortuosity in the polymer electrolyte, and a value of 1.8 gives a linear fitting of the Bruggeman relation to the diffusion results.

Evaluation of polarization loss and mass flow dynamics of HT-PEMFC can be solved by each cell division. The CCL was divided into 10 cells in this study, from the cell numbered N=0 in the membrane side to the cell numbered N=10 in the GDL-MPL side. The effective Knudsen diffusion coefficient of the CL of the HT-PEMFC was successfully calculated by substituting tortuosity values of both pores in Eq. (4-13). Current distributions were calculated in divisions by solving Butlere-Volmer equations, where N=1-10, for this calculation. Various local properties inside of the CL, such as mass transport, gas diffusion, tortuosity, porosity, and pore diameter were also calculated in each division. Sectional component ratios, surface areas of electrocatalyst, O_2 gas distribution, and percolation of both the electrolyte and carbons were analyzed as mentioned later.

Loaded electrocatalysts was Pt 46.8wt% in the 3D CCL model. Pt is the most active noble metal that catalyzes and promotes the ORR that takes place in HT-PEMFC. Since it is the catalyst surface area that matters, and not weight, it is important to have small Pt particles with large surface areas finely dispersed on the catalyst support surface, which is typically carbon. The structural parameters for the GDL are summarized in Table 4.1 In addition, the structural parameters for the CCL including the calculated tortuosity values of the pores in the CCL are summarized in Table 4.4. The performance of the cell voltage was calculated at three kinds of temperatures, 150˚C, 170˚C and 190˚C. The cell was assumed to be fed by air(C^{N2}_{in} / C^{O2}_{in}=0:79/0:21) as an oxidant on the cathode side, and as a total pressure was assumed to be 1 atm. The cell operating conditions are concluded in Table4.5.

Fig.4.2 (a) shows a 3D view of computed all possible tortuous proton-conducting trajectories (blue lines) in the connected H_3PO_4 electrolytes. Fig.4.2 (b) shows a 3D view of computed all possible tortuous electron-conducting trajectories (black lines) in electrically connected carbon medium. Fig.4.2 (c) shows a 3D view of computed all possible tortuous gas diffusion trajectories (red lines) in connected pores. In fact, the computed tortuosity value of gas, 1.3, was used for solving for mass transport of the CCL. Fig.4.2(d) shows the distribution of the component ratio of mesopore, carbon, and acid in the CL. Fig.4.2(e) shows the distribution of mesopore

diameter, d_p (nm) in the CL. The value of the tortuosity was difficult to obtain experimentally. However, theoretical tortuosity-porosity relations that do not contain adjustable parameters have been presented as $\tau^2=2-\varepsilon$, by Rayleigh(1892), $\tau^2=1-1/2\ln\varepsilon$, Strieder(1986) and $\tau^2=\varepsilon^{-1/2}$, by Bruggemann(1935) [60,61]. Fig.4.3 shows simulated effective relative diffusivity ε/τ in Eq.(4-15), and compared with presented these formula. Simulated results for effective relative diffusivity ε ε/τ, showed good agreement with currently presented formula by Bruggemann (1935), Strieder (1986), and Rayleigh (1892) [61,62]. Especially for Bruggemann formula, it has been referred in many theoretical models of PEMFC.

Passalacqua [63] and Wei [64] introduced a percolation model to explain both ionic and electronic conductions. Actually, as shown in Fig.4.2 (a)-(c), three tortuous percolating paths of the electrons in carbon, protons in electrolyte, and O_2 gas in pores could be successfully visualized (even when the assumption of thin electrolyte film satisfies proton percolation completely) from the PBI-H_3PO_4 membrane to the MPL-GDL side. Therefore, the loaded electrocatalyst could maintain electrochemically active surface area from the PBI-H_3PO_4 membrane side to the MPL-GDL side. At that time, catalyst utilization in the CL was counted as 22%, which is close to the experimental value of 20% [65].

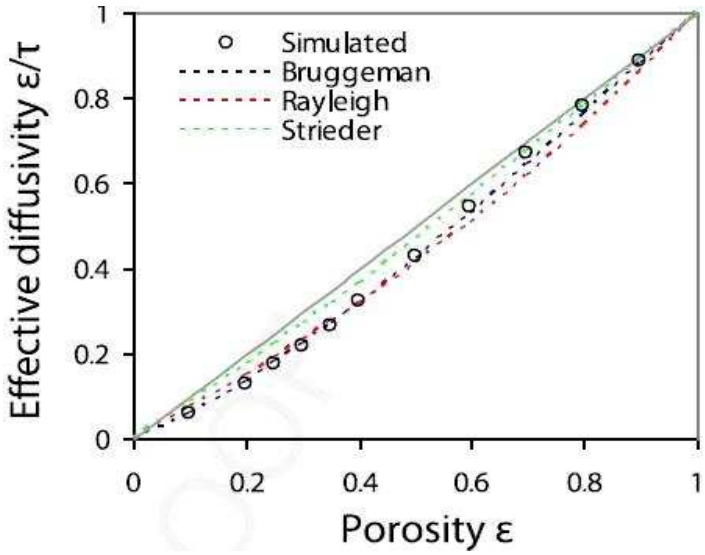

Fig.4.3 Simulated effective relative diffusivity ε/τ, and compared with presented formula.

4.3.2 Quantum chemical analysis of electrocatalysts on carbon support

The catalyst loaded on the carbon support in CL of HT-PEMFC was mainly composed of 46.8 wt% of the noble metal Pt ($5d^9 6s$). The microscopic morphological condition was reflected to model a quantum chemical investigation. The Pt catalyst composed 55 atoms of Pt crystal on the carbon support was modeled as having a Pt (111) facet in themselves by referring to the TEM images [31]. Fig.4.4 shows the atomic model of a Pt55 catalyst cluster on the graphite carbon support (001) facet and its electron density, obtained by UA-QCMD simulation at 150˚C. The UA-QCMD simulations were performed totally 2000 fs (10,000 steps) with 0.2fs/step under the NPT ensemble, and one quantum chemical calculation by TBQC was inserted per 100 steps. At the same time, electronic distribution was also obtained as shown in section. Before checking the affinity between catalysts and support, Pt55 and carbon support were, respectively, investigated and compared energetically with experimental results as shown in Table 4.6. The Pt-Pt distance of metallic Pt is 2.75 Å [66, 67], and Pt-C bond distance is around 2.0 Å [67]. As concluded in Table 6, the sums of the binding energies of Pt55 and graphite carbon support were -7510.24 and -5552.16kcal/mol. These calculated energies were agreed well with $\Delta_f H^0$, the standard molar enthalpy of formation at 298 K [68], with a high concordance rate of more than 95.5% for both case. The interactions between supported metals and graphite carbon for Pt/C were investigated independently. Binding energies of Pt55 and the carbon supports were estimated by the quantum chemical

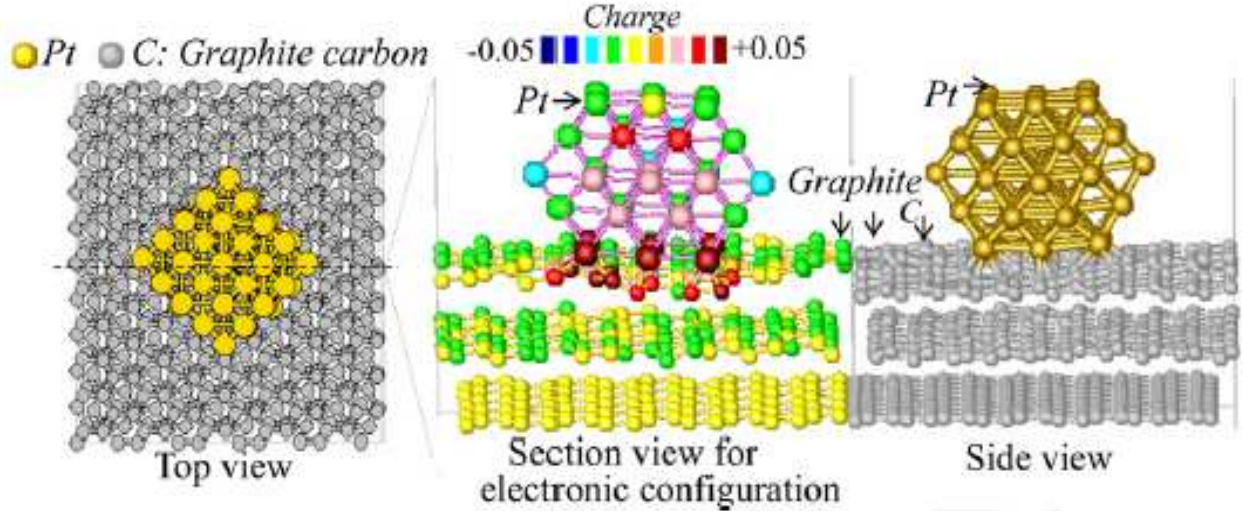

Fig.4.4 Electronic configuration of platinum,Pt55 on graphite carbon support at 150℃.

calculation program TBQC [17-19]. The binding energy of Pt-C when Pt55 was supported on carbon was approximately 50kcal/mol at 300K. The affinity of Pt with carbon in the Pt55/ graphite (001) system found to be via Pt5d-C2p hybridization by the analysis of electronic structure. This Pt5d-C2p hybridization between both Pt orbital and neighboring C orbital make the Pt more cationic than free Pt. As shown in Table 4.7, the binding energies between Pt electrocatalysts and the graphite carbon support found to be gradually smaller, -49.51kcal/mol at 150˚C, -48.87kcal/mol at 170˚C, and -46.24kcal/mol at 190˚C. It indicated the affinity of electrocatalysts with the support became weaker, and the electrocatalysts become susceptible to migrate easily as temperature increased.

Table4.6 Bond energies of the support (graphite carbon) and supported catalysts, Pt55 compared with experimental lattice energies.

Catalysts/ support	Each bond Energy [kcal/mol]	Sum of Bonding energy [kcal/mol]	$\Delta_f H^0$ [kcal/mol]
Pt55 Pt-Pt	-32.86	-7510.24	-7431.05
Graphite carbon C-C	-115.67	-5552.16	-5780.03

$\Delta_f H^0$ Standard molar enthalpy(heat)of formation at 298.15 K [kcal/mol] [67]

Table4.7 Binding energies and bond distances of Pt-C and Pt-Pt_{55}/graphite carbon system.

Temperature	Pt-C binding energies [kcal/mol]	Pt-Pt binding energies [kcal/mol]
150˚C	-49.51(2.0 Å)	-30.58(2.8 Å)
170˚C	-48.87(2.0 Å)	-30.58(2.8 Å)
190˚C	-46.24(2.0 Å)	-30.26(2.8 Å)

4.3.3 Durability of electrocatalysts

Shao-Horn [31] who referred to the experiments by Bett [68] estimated the diffusion order of Pt particles on carbon support as $10^{-21} m^2 s^{-1}$, at 600˚C. The metals that were expected to behave as catalysts on support were on the nm scale, and at such an atomic scale condition, their thermal mobility is affected by metal self-diffusion. The pre-exponential factors, D_{M0} and the activation enthalpies, E_M of metals and alloys are typically in the range of $10^{-6} m^2 s^{-1} \leq D_{M0} \leq 10^{-3} m^2 s^{-1}$ and $50 kJmol^{-1} \leq E_M \leq 600 kJmol^{-1}$ [27]. In case of Pt, these were measured as $D_{M0}=0.05\times10^{-4} m^2 s^{-1}$ and $E_M=257.6 kJ/mol$ [27].

According to Eq. (4-8), the diffusion coefficient of the Pt metal, D_M was estimated as $D_M=2.0\times10^{-21}m^2s^{-1}$ at the certain temperature, 600˚C. This was good agreement with the experimentally observed Pt diffusivity as mentioned above.

The numerical values of diffusion parameters, D_{M0} and E_M were introduced as input parameters in the 3D-KMC model. Since these two parameters are universal to the temperature under the Arrhenius equation (4-8), it could be applied to different three temperatures, 150˚C, 170˚C and 190˚C in this study. A series of 3D-KMC simulations for different temperatures, 150˚C, 170˚C and 190˚C could be successfully conducted. As a result, the theoretically evaluated particle size distributions and the mean diameters of the Pt nanoparticles compared with TEM images of electrode catalysts were obtained as shown in Fig.4.5. Fig.4.5 (a) corresponds to the image just prior to sintering, and showed that the carbon particle was modeled as spherical in shape in order to reproduce its real structure by reflecting the TEM micrograph of the CL [20]. As seen in Fig.4.5 (a), the mean particle diameter of the catalyst at the fresh condition was modeled to 3.78nm. It agrees with experimentally observed average diameter of fresh condition found to be 3.8nm. These catalysts were dispersed on the surface of primary carbon particles to maximize the surface area of Pt per unit Pt mass [31]. The mean diameter of agglomerated particle size of electrocatalysts was theoretically evaluated by the 3D-KMC simulation at constant temperature, 150˚C. was 4.4nm after 1,000h, which was close to the measured mean particle diameter, 4.1nm after 1,029h as shown in Fig. 4.5 (b) In the case of 190˚C, the simulated sintered particle size after 1,250h was 6.2nm, which was very close to the measured mean diameter, 6.0nm after the same aging time, 1,250 h [20] as shown in Fig.4.5 (c) In both cases, the theoretical predictions of sintering were in good agreement with the experimental data. In the case of 170˚C, the theoretically evaluated agglomerated size was assumed to be 4.56nm at the same time of aging, about 1,000h. As seen in electrocatalysts in simulated snapshots continuously from the fresh condition in Fig.4.5 (a) to the both aged condition at 150˚C (Fig.4.5 (b)) and 190˚C (Fig.4.5 (c)), the size of electrocatalysts grew increasingly similarly to the TEM micrographs.

In previous studies, it was also reported that the size of Pt electrocatalyst particles grew during power generation in a relatively short period of approximately 500h at 150˚C [1-6]. Especially, Zhai showed that Pt

aggregation occurred by increasing its size from 4.0 to 8.3nm in the early stage of power generation during the first about 300 h [1], and increasing its size from 4.02 to 8.88nm during 550h [2] at 150˚C. Hu and Liu also reported the Pt agglomeration from 3.8nm to 6.9nm during 500h [3, 4] and from

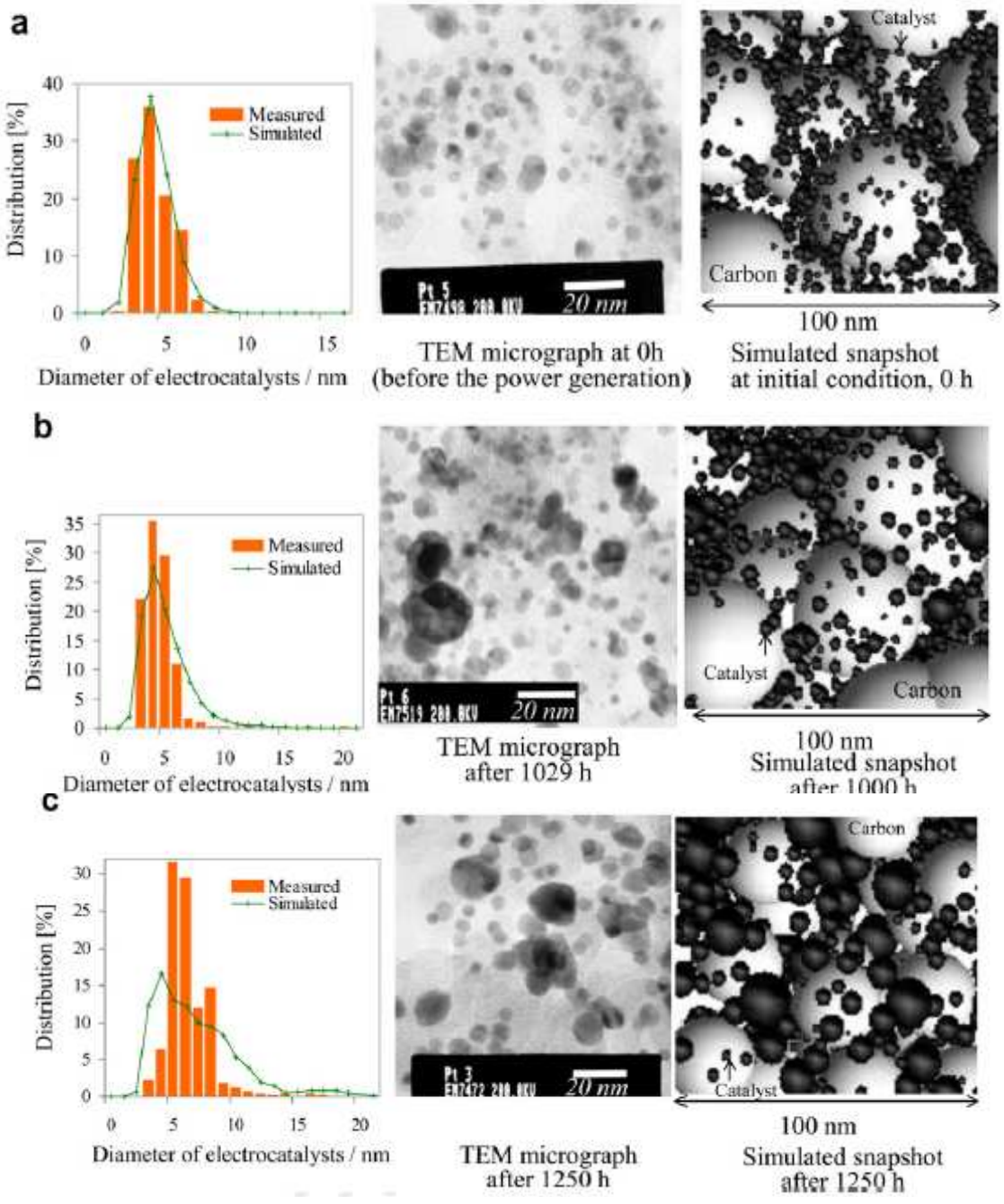

Fig.4.5 (a) Fresh condition (0 h) (b) After about 1,000h at 150˚C (c) After about 1,250h at 190˚C. Snapshots and distribution of the nanoparticles of electrocatalysts theoretically obtained by the results of 3D-KMC method were compared with experimentally measured data.

3.72nm to 8.39nm during 600h at 150˚C [5].

From this point of view, Fig.4.6 shows the time course of electrochemical active surface area and its loss percentage at 150˚C, 170˚C, and 190˚C. The data were obtained by the 3D-KMC method at 150˚C, 170 ˚C and 190˚C. The loss of electrochemical active surface area for initial 1,000h were -15.2% at 150˚C, -16.6% at 170˚C and -34.5% at 190˚C. Overall loss during long-term power generation were -21.4% for 15,500h at 150˚C, -30.8% for 6,300h at 170˚C and -39.6% for 1,250h at 190˚C. The decrease rate in electrochemical active surface area of the electrodes found to become higher as temperature increased. Losses of cell performance due to decreasing electrochemical active surface area can be estimated by the following equation [6].

$$\Delta V = b \log\left(\frac{EAS_1}{EAS_2}\right) \tag{4-32}$$

where ΔV is the voltage drop, b is the Tafel slope, EAS_1 and EAS_2 are the electrochemical active surface areas before and after, respectively. According to the value reported by Liu et al. [60] for b (100mVdec^{-1}), the voltage loss coming from losses of catalytic active surface area is approximately 7.2mV at 150˚C and 18 mV at 190˚C for initial 1,000h. These estimated voltage drops derived from decreasing electrochemical active surface area found to be close to experimentally measured voltage drops, 8.4mV at 150˚C and 16.6mV at 190˚C.

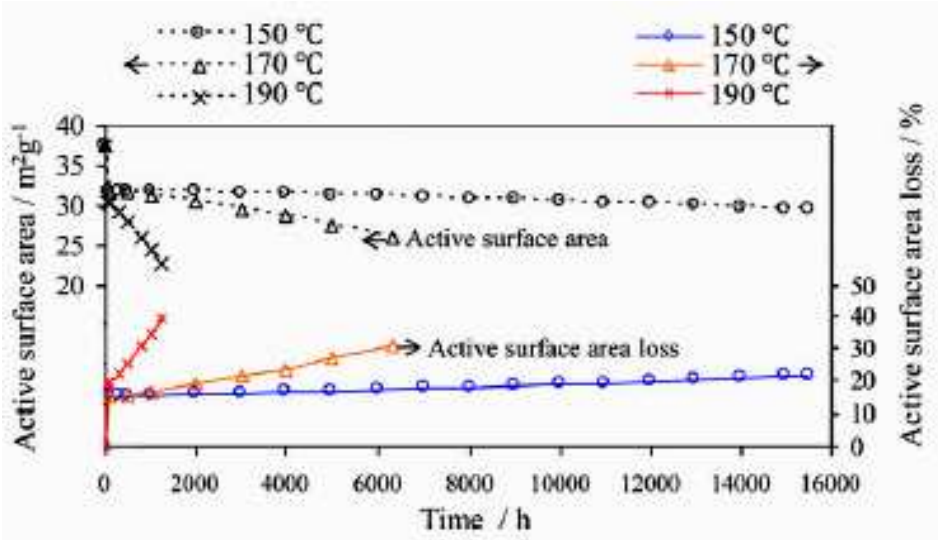

Fig.4.6 Time course of electrochemical active surface area and its loss percentages at 150˚C, 170˚C, and 190˚C.

4.3.4 Long-term characteristics of voltage drops

Changes in the average diameter (Fig.4.5) and the electrochemically active surface area (Fig.4.6) due to progressing in agglomeration of Pt electrocatalysts could be estimated by 3DKMC method. Such agglomerated catalyst conditions at a certain time were reflected in the modeling of 3D CCL to express the aged catalysts in order to simulate the degree of deterioration and how much voltages changed from the fresh condition at temperatures, 150˚C, 170˚C and 190˚C.

Not only catalyst deterioration, but also acid evaporation can be occurred in the HT-PEMFC. In order to investigate factors other than catalyst particle aggregation, the case for evaporation of acid were additionally investigated. Under dry condition, phosphoric acids dehydrate to loose water by dimerization and pyrophosphoric acids ($H_4P_2O_7$) can be started by the following stage [70]:

First stage: $2H_3PO_4 \Leftrightarrow H_4P_2O_7 + H_2O\uparrow$

It is possible further dehydration to triphosphoric acid at a higher temperature and very dry condition as the second stage [73].

Second stage: $H_4P_2O_7 + H_3PO_4 \Leftrightarrow H_5P_3O_{10} + H_2O\uparrow$

Under dry and higher temperature condition in this study, loss of water and the formation of pyrophosphoric acid ($H_4P_2O_7$) have great potential for causing to decrease the proton conductivity [73]. Lobato compared the weight loss of PBI-H_3PO_4 membrane with time and found that the higher the temperature, the more rapid the dehydration process is, and it correlates well with the rate of performance decay at 175˚C was greater than at 150˚C[6]. Moreover, Okae et al. investigated the effect of phosphoric acid reduction on cell performance for PAFC [71]. The estimated evaporation rates were 0.6, 1.8 and 9$\mu gm^{-2}s^{-1}$ for cell temperatures at 150, 170 and 190˚C, respectively. After acid was evaporated, the remaining volume of phosphoric acid assumed to became thinner. Since the evaporation amount of hot phosphoric acid per hour could be calculated as above, the remaining volume of phosphoric acid was mounted to model aged CCL structure. Evaporation of acid from the CCL made the protons less able to reach the ORR site. In fact, the proton paths in the CCL become more

tortuous. The active surface area of catalysts was also decreased due to depletion of protons, as shown in Fig.4.6.

Fig.4.7 shows the decrease rate of proton conductivity in the CL at (a) 150 ˚C, (b) 170˚C and (c) 190˚C. The calculated values of tortuosity factors τ according to Eq. (4-30) were 1.88 for fresh conditions, and more than 2.0 for aged conditions for 150˚C, 170˚C and 190˚C. Initial tortuosity value for the proton paths is 1.88, and gradually increased depending on the temperature, 2.01 at 15,500h 150˚C, 2.09 at 6,300 h at 170˚C, 2.02 at 1,250h at 190˚C due to depletion of phosphoric acid. Therefore, the total decrease rate of proton conductivity over time were about 35% for 15,500h at 150˚C, 45% for 6,300h at 170˚C, and 33% for 1,250h at 190˚C. Because this decrease rate was compared by different hours, the decreasing rate of proton conductivity for same time interval, initial 1,000h was also investigated. As a result, the decrease rate of the theoretically estimated proton conductivity for initial 1,000h, were about 4.0% at 150˚C, 14.6% at 170˚C, and 20.5% at 190˚C, averagely. As the amount of evaporation of acid increased, the proton path became more tortuous. As increasing of temperature, calculated trajectories of protons became more tortuous to conduct themselves in the search of depleted acid electrolyte after aging. As the amount of acid decreased and the tortuosity value of proton path increased with elevating temperature, the proton conductivity decreased according to Eq. (4-30).

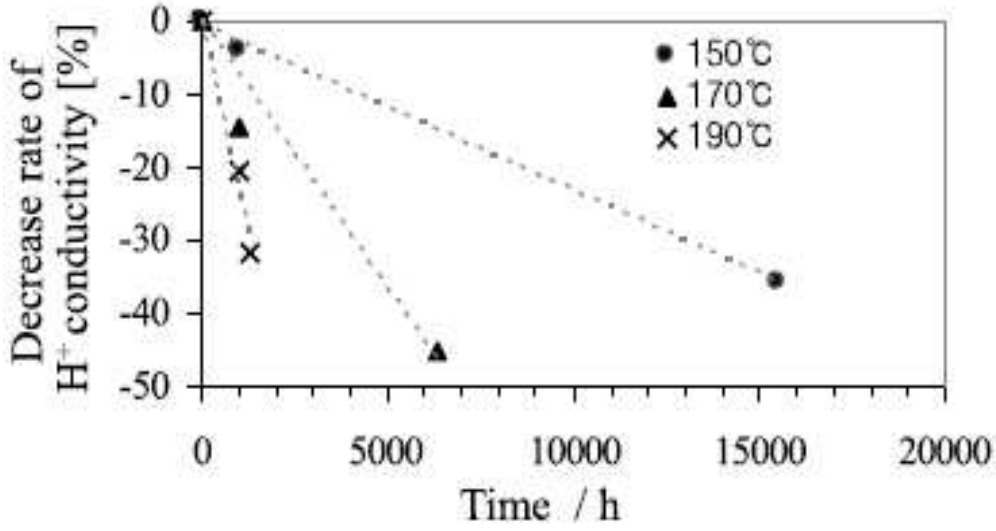

Fig.4.7 Decrease rate of proton conductivity with time at (a) 150˚C, (b) 170˚C and (c) 190˚C.

The changes in cell voltage over time were simulated as shown in Fig.4.8 (a) for 150˚C, Fig.4.8 (b) for 170˚C, and Fig.4.8 (c) for 190˚C. In these

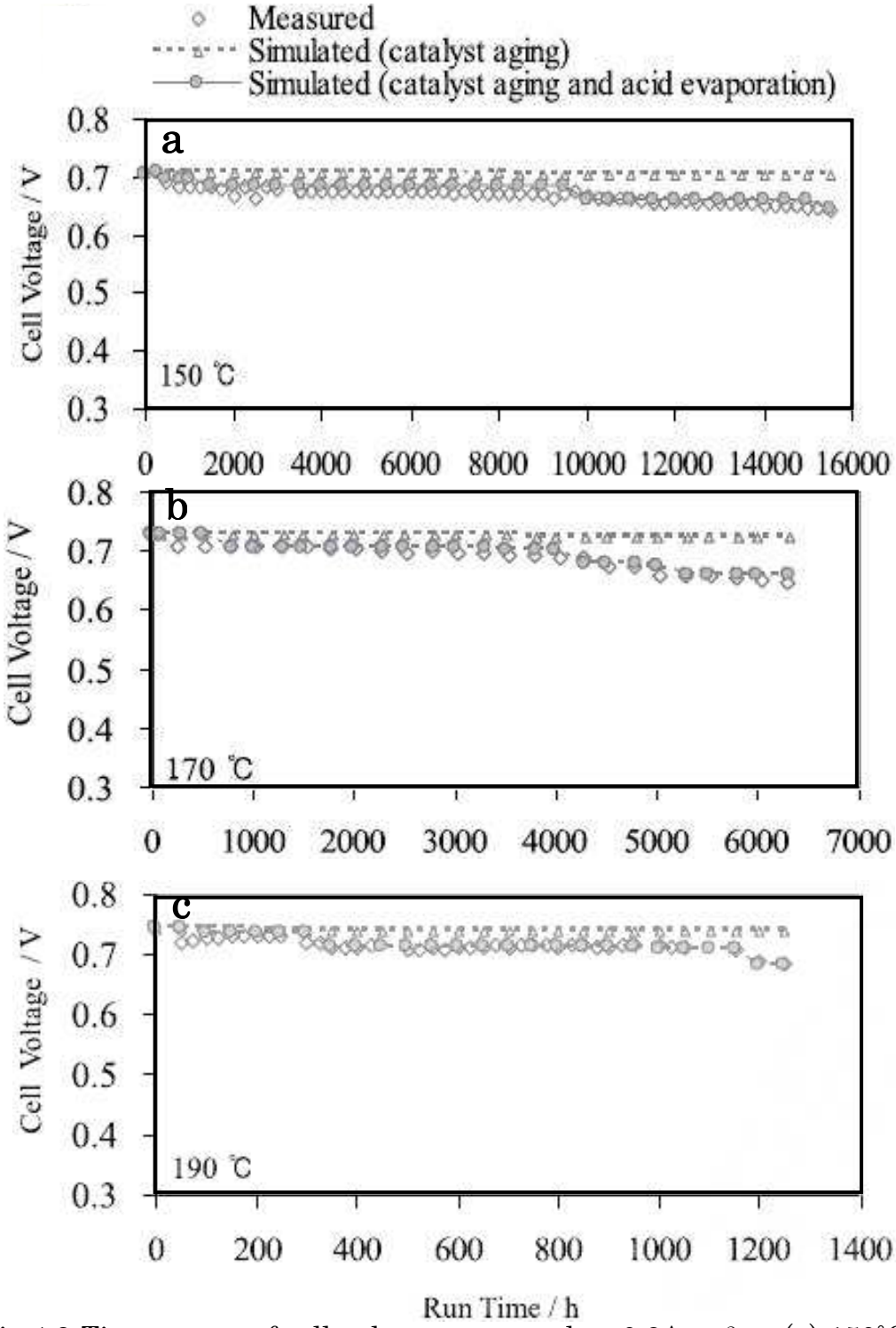

Fig.4.8 Time course of cell voltages operated at 0.2Acm^{-2} at (a) 150˚C (b) 170˚C (c)190˚C. The simulated results were compared with the cell voltages, shown in Fig.3.4, experimentally measured by durability tests of the section 3.

tests, the current density was constant at 0.2A cm^{-2}. Simulated results were two cases. One is the case reflected by catalyst aging only. The other case is reflected catalyst aging together with evaporation of acid. Experimentally measured voltage showed that the cell voltage declined very gradually from the beginning of power generation to the experimental data show in any temperature cases in Fig.4.8 (a)-(c). The simulated voltage drops in initial several hundreds of hours in the durability tests were 10-20mV. The evaporation of acid has high potential to cause the voltage drops more severely for the latter stage. It was clearly found that from both results showing in Figs.4.7 and 4.8, decrease of the proton conductivity correlates well with the voltage drops as temperature increased.

Especially at 170˚C, the experimentally measured cell voltage remained constant for a long time after its initial drop of 20mV, as shown in Fig.4.8 (b). After square root of time √t =70h (t=4,900h) something changed, and a new mechanism dominated the cell internal resistance shown in Fig.3.4 (b). It is believed that some other factor was responsible for the final drop in cell voltage and increase of cell internal resistance. When the cell internal resistance is plotted over time (Fig.4.9), the plot fits a parabolic curve. Fuel cell degradation can be described in several ways [72, 73]. It is known that many types of fuel cell degradation obey a parabolic law with time [74, 75]. The underlying mechanism of such parabolic degradation includes a variety of degradation phenomena, including loss of porosity in electrodes, growth of corrosion layers, growth of non-conductive phases between electrodes and electrolyte, increase in polarization overpotential, etc. Most fuel cells have these types of parabolic degradation. For the present work, this is part of an

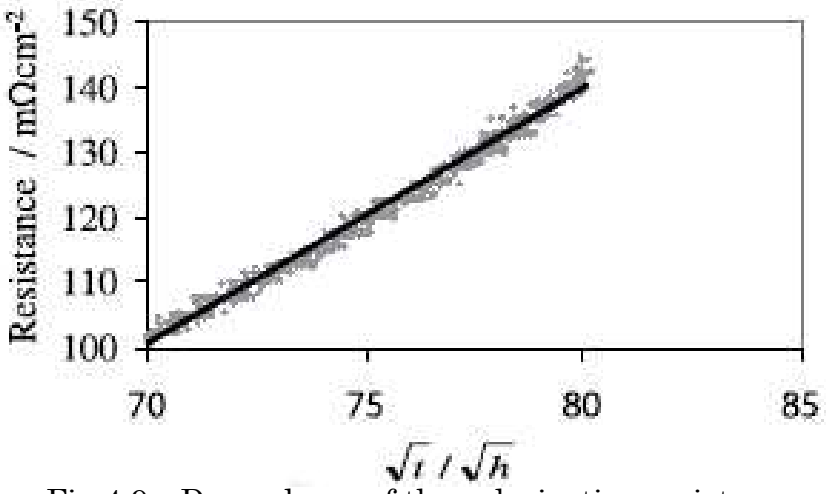

Fig.4.9 Dependence of the polarization resistance.

on-going investigation for a particular operating temperature.

Fig.4.10 shows the relationship of initial cell voltage to cell temperature operated at 0.2Acm^{-2} at 150˚C, 170˚C, and 190˚C, which is confirmed by both experimentally measured and simulated results. Simulated initial cell voltages were gradually increased as temperature increased, 0.70V at 150˚C, 0.72V at 170˚C, and 0.74V at 190˚C. Experimentally, 0.69V at 150˚C, 0.71V at 170˚C, and 0.73V at 190˚C. This tendency shows correct trends of increasing in initial voltage as cell temperature increased.

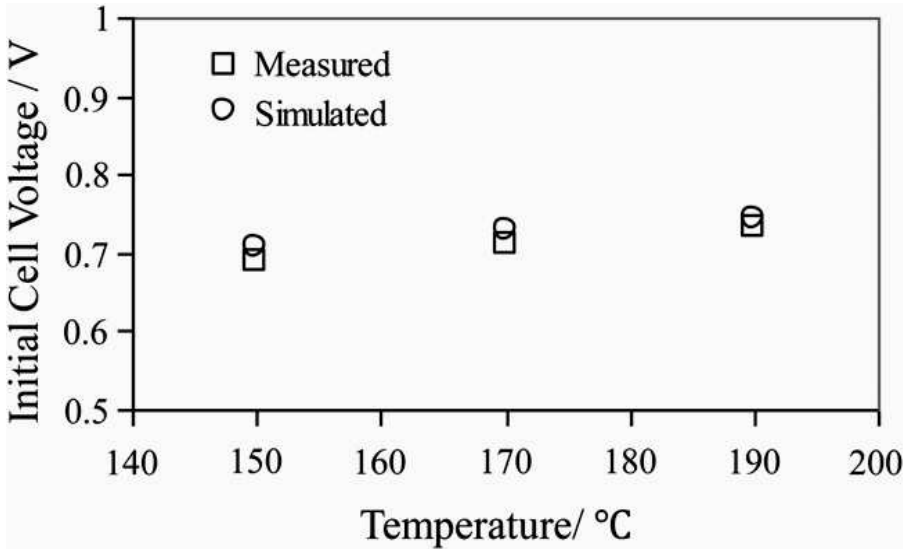

Fig.4.10 Relationship of initial cell voltage to cell temperature operated on 0.2Acm^{-2} at 150˚C, 170˚C and 190˚C. The simulated results were compared with experimentally measured voltages.

Fig.4.11 shows the relationship between cell voltage decline rate and cell temperature over long-term power generation. The cell voltage deterioration rate of the cell voltage from its peak values over time was strongly dependent on temperature. The theoretical prediction estimated the correct trend in voltage deterioration rate with temperature. The deterioration rates of the voltage increased with a rise in the cell temperature. Experimentally, overall voltage declines were 3.16, 10.09, and 44.01mV/h at 150˚C, 170˚C and 190˚C, respectively. Theoretical predictions could estimate the breakdown of overall voltage decline. At first, the partial voltage drops caused by loss of active surface area of the Pt electrocatalyst were computed approximately 0.20, 0.74, and 5.02mV/h at 150˚C, 170˚C and 190˚C, respectively. Secondly, the overall voltage drops caused by loss of acid and active surface area of the Pt electrocatalysts in the CCL were approximately 3.97, 11.73, and 47.78mV/h at 150˚C, 170˚C and 190˚C,

respectively. This tendency shows better agreement with the experiment than considering only loss of active surface area of the electrocatalyst. Theoretical results clearly show that long-term durability for practical applications requires inhibition of catalyst aging, as well as controlling the evaporation of acid.

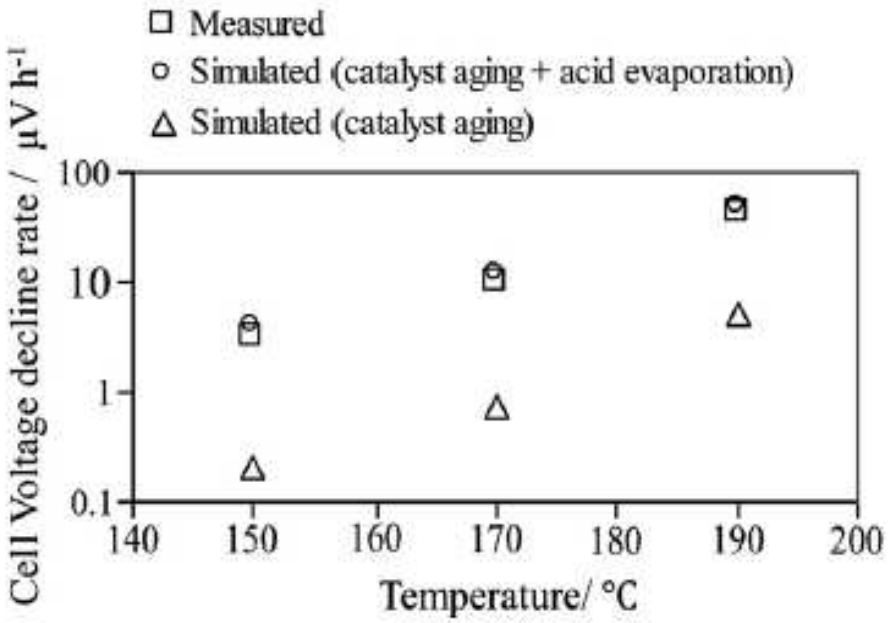

Fig.4.11 Relationship of cell voltage decline rate to cell temperature over long-term power generation operated on 0.2 A cm^{-2} at 150˚C, 170˚C, and 190˚C. The simulated results were compared with experimentally measured voltages.

4.4 Conclusions

The correlation of operating cell temperature in HT-PEMFC with the deterioration of electrocatalysts and voltage drops were theoretically estimated by using the 3D-KMC method and the evaluation algorithm of polarization loss at different temperatures. Diameters of agglomerated electrocatalysts were theoretically estimated, and the values were 4.4, 5.5, and 6.2nm after aging about 1,000h at 150˚C, 170˚C, and 190˚C, respectively. Theoretically estimated agglomerated particle sizes showed good agreement with experimental TEM data, which found to be 4.4nm after 1,029h and 6.2nm after approximately same time. This fact was exemplified by UA-QCMD method that shows the affinity of Pt electrocatalysts with the support surface gradually decreases as increasing

temperature.

The particle-based 3D CCL structure was modeled to contain Pt/carbon with a thin layer of H_3PO_4 electrolyte film content. Modeled CCL microstructure was verified to investigate connectivity of pores where oxygen as a reactant gas pass through from MPL-GDL side inside of the CCL, and conductivities of protons and electrons. In addition, the tortuosity values of pores, protons, and electrons inside of the constructed CCL microstructure model were calculated three dimensionally to introduce them into the evaluation algorithm of polarization loss as the diffusion parameters. Consequently, it was clarified that a higher cell temperature resulted in a higher initial cell voltage and higher voltage drops.

The measured voltage drops during overall experimental durability examination were found to be 3.16mV/h for 150˚C, 10.09mV/h for 170˚C, and 44.01mV/h for 190˚C, respectively. Experimentally measured results show that raising the operating temperature in order to increase the cell voltage and improve efficiency leads to be difficult sustain long-term durability. Conversely, lowering the temperature improves durability but remain to be lower cell voltages. Theoretically evaluated overall voltage drops reflected only loss of electrochemical active surface area were approximately 0.20mV/h for 150˚C, 0.74mV/h for 170˚C, and 5.02mV/h for 190˚C, respectively. On the other hand, the other overall voltage drops, which were theoretically evaluated by reflecting loss of both acid and electrochemical active surface area in the CL were 3.97mV/h for 150˚C, 11.73mV/h for 170˚C, and 47.78mV/h for 190˚C, respectively. As a result, experimentally measured overall voltage drops quantitatively agreed well with theoretically evaluated voltage drops which were reflected both acid and electrochemical active surface area, rather than considering only loss of electrochemical active surface area. The reduction in measured cell voltage during the long-term experimental cell operation of three cells was considered to be caused both by aggregation of the electrode catalyst particles and evaporation of acids. Theoretical results clearly showed that long-term practical application in high-temperature operation requires to make electrocatalysts durable as well as controlling evaporation of acid to keep proton conductivity. Because the amount of voltage loss caused by the depletion of specific surface area of electrocatalyst was smaller than that caused by both sintering of electrocatalysts and the evaporation of acid, theoretical study successfully explains that sufficient controlling of the

evaporation of acid is the key to achieving long-term power generation of HT-PEMFC for practical application.

Appendix. List of symbols

a_{cat} Electrocatalytic surface area, m^2g^{-1}

$C_{O_2}^{ref}$ The reference O_2 concentration, $molcm^{-3}atm^{-1}$

$C_{O_2}^{Ref,\ i}$ The dissolved O_2 concentration of cell *i* in the electrolyte, mol cm^{-3}

d_p The local mesopore diameter in the catalyst layer, nm

D_{O2} The molecular diffusion coefficient of O_2, cm^2s^{-1}

$D_{kn,i}$ The Knudsen diffusion coefficient of O_2 in cell i, cm^2s^{-1}

$D_{O_2\,i}^{Ref,}$ The effective O_2 diffusion coefficient in cell i, cm^2s^{-1}

P_{O2} The O_2 partial pressure, atm

P_{H2} The H_2 partial pressure, atm

P_{H2O} The H_2O partial pressure, atm

x The length in the direction of the thickness of the catalyst layer of each cell, μm

F Farday's constant, 96487, $Cmol^{-1}$

i The cell number, —

$i_{r,i}$ The reaction current density in cell i, Acm^{-2}

i_0 The exchange current density in cell, Acm^{-2}

$H_{O_2}^{hot\ H_3PO_4}$ Henry's constant for oxygen dissolution in polymer electrolyte

L_{CCL} The thickness of the cathode catalyst layer (CCL), μm

L_{GDL} The thickness of the gas diffusion layer (GDL), μm

m_{Pt} The catalyst mass loading per unit area of the cathode, g m^{-2}

M_{O2} O_2 molecular weight, 32 $gmol^{-1}$

n The number of electrons transferred in the cathode reaction per O_2 molecule, 4, —

N_{O2} The O_2 flux into cell I, mol $cm^{-2}s^{-1}$

$\%_P$ The mass percentage of Pt electrocatalyst supported

(v) The mean thermal velocity of molecules, ms^{-1}

R Gas constant, 8.314, $JK^{-1}mol^{-1}$

RH Relative humidity, %

T The cell temperature, K

t The cell temperature, ◦C

Greek symbols

τ The tortuosity factor, —

α_c The cathode transfer coefficient, —

ε Porosity of the cathode catalyst layer (CCL), —

ε_H The H_3PO_4 volume faction, —

ε_p The pore space volume, —

ε_c The volume faction of electrocatalysts (Pt/C) dispersed carbon, —

ε Volume fraction of phosphoric acid in cell i, —

ε_{GDL} Porosity of the GDL, —

γ The Bruggeman factor, —

η_i The activation overpotential, V

ρ_{el} The density of the electrolyte(PBI/H_3PO_4), 1.6 g cm^{-3}[63]

ρ_{Pt} The density of Pt, 21.5 g cm^{-3}[75]

ρ_C The density of carbon, 2.0 g cm^{-3}

σ The conductivity, S cm^{-1}

References

[1] Y. Zhai, H. Zhang, D.Xing, Z.G. Shao ; J. Power Sources 164 (2007) 126.
[2] Y. Zhai, H.Zhang, G.Lu, J. Hu, B. Yi ; J. Electrochem. Soc. 15(1) (2007) B72.
[3] J.Hu, H.Zhang, Y.Zhai, G.Liu, B.Yi. ; Int. J. Hydrogen Energy 31 (2006) 1855.
[4] J. Hu, H. Zhang, Y. Zhai, G. Liu, J. Hu, B. Yi ; Electrochim. Acta 52(2) (2006) 394.
[5] G. Liu, H. Zhang, J. Hu, Y. Zhai, D. Xu, Z. Shao ; J. Power Sources, 162-1 (2006) 547.
[6] J. Lobato, P.Canizares, M.A.Rodrigo, J.J.Linares ; Electrochim. Acta, 52(2) (2007) 3910.
[7] D.Cheddie, N.Munroe ; Energy Convers Manage 47 (2006) 1490.
[8] D.Cheddie, N.Munroe ; J. Power Sources 156 (2006) 414.
[9] D.Cheddie, N.Munroe ; J. Power Sources 160 (2006) 215.
[10] T.Sousa, M.Mamlouk, K.Scott ; Chem. Eng. Sci. 65 (2010) 2513.
[11] T.Sousa, M.Mamlouk, K.Scott ; Int. J. Hydrogen Energy 35 (2010) 12065.
[12] K.Jiao, X.Li ; Fuel Cells 10 (2010) 351.
[13] E.U.Ubong, Z.Shi, X.Wang ; J. Electrochem. Soc., 156 (2009) B1276.
[14] J.Peng, S.J.Lee ; J. Power Sources, 162 (2006) 1182.
[15] J.Peng, J.Y.Shin, T.W.Song ; J. Power Sources, 179 (2008) 220.
[16] K.Jiao, I.E.Alaefour, X.Li ; Fuel 90-2 (2011) 568.
[17] A.Suzuki, K.Nakamura, R.Sato, K.Okushi, R.Miura, R.Nagumo, et al. ;Top Catal, 52 (2009) 1852.
[18] A.Suzuki, K.Nakamura, R.Sato, K.Okushi, R.Miura, R.Nagumo, et al.; Surf. Sci. 603 (2009) 3049.
[19] A.Suzuki, K.Nakamura, R.Sato, K.Okushi, R.Miura, R.Nagumo, et al.; SAE Int. J. Fuels Lubricants, 2-2 (2010) 337.
[20] Y.Oono, T.Fukuda, A.Sounai, M.Hori ; J. Power Sources 195 (2010) 1007.
[21] Z.Fishman, J.Hinebaugh, A.Bazylak ; J. Electrochem. Soc. 157(11) (2010) B1643.
[22] R.Flückiger, S.A.Freunberger, D.Kramer, A.Wokaun, G.G.Scherer ; Electrochim. Acta 54 (2008) 551.
[23] Y.Oono, A.Sounai, M.Hori ; J. Power Sources 189 (2009) 943.
[24] P.Selvam, H.Tsuboi, M.Koyama, A.Endou, H.Takaba, M.Kubo, et al., Rev. Chem. Eng. 22 (2006) 377.
[25] L.Verlet ; Phys. Rev. 159 (1967) 98.
[26] L.V. Woodcock ; Chem. Phys. Lett. 10 (1971) 257.
[27] H.Mehrer ; LandöIteBornstein, III26, diffusion in solid metals and alloys (1990).
[28] M.A.Kanter ; Phys. Rev. 107(3) (1957) 655.

[29] P.L.Antonucci, F.Romeo, M.Minutoli, E.Alderucci, N.Giordano ; Carbon 26(2) (1988) 197.
[30] P.J.Ferreira, G.J.La O', Y.Shao-Horn, D.Morgan, R.Makharia, S.Kocha, et al. ; J. Electrochem. Soc. 152(11) (2005) 2256.
[31] Y.S.Horn, W.C.Sheng, S.Chen, P.J.Ferreira, E.F.Holby, D.Morgan ; Top Catal 46 (2007) 285.
[32] C.Marr, X.Li ; J. Power Sources, 77 (1999) 17.
[33] S.R.Choudhury, R.Rengaswamy ; J. Power Sources 161 (2006) 971.
[34] T.Hattori, A.Suzuki, R.Sahnoun, M.Koyama, H.Tsuboi, N.Hatakeyama, et al. ; Appl. Surf. Sci. 254 (2008) 7929.
[35] A.Suzuki, U.Sen, T.Hattori, R.Miura, R.Nagumo, H.Tsuboi, et al. ; Int. J. Electrochem. Sci. 5 (2010) 1948.
[36] A.Suzuki, U.Sen, T.Hattori, R.Miura, R.Nagumo, H.Tsuboi, et al. ; Int. J. Hydrogen Energy 36 (2011) 2221.
[37] J.Lobato, P.Canizares, M.A.Rodrigo, J.J.Linares ; Fuel Cells 10(2) (2010) 312.
[38] C.Y.Du, T.Yang, P.F.Shi, G.P.Yin, X.Q.Cheng ; Electrochim. Acta 51 (2006) 4934.
[39] Y.Nakashima, S.Kamiya ; J. Nucl. Sci. Tech ; 44(9) (2007) 1233.
[40] D.M.Bernardi, M.W.Verbrugge ; J. Electrochem. Soc. 139(9) (1992) 2477.
[41] W.Sun, B.A. Peppley, K.Karan ; Electrochim. Acta 50 (2005) 3359.
[42] D.Song, Q.Wang, Z.Liu, T.Navessin, M.Eikerling, S.Holdcrot ; J. Power Sources 126 (2004) 104.
[43] J.Hu, H.Zhang, J.Hu, Y.Zhai, B.Yi ; J. Power Sources 160 (2006) 1026.
[44] F.Barbier ; PEM fuel cells: theory and Practice, Oxford Academic (2005)
[45] S.J.Clouser, J.C.Huang, E.Yeager ; J. Appl. Electrochem. 23(6) (1993) 597.
[46] A.J.Appleby ; J. Electroanal. Chem. Interfacial Electrochem. 24(1) (1970) 97.
[47] W.E. O'Grady, E.J.Taylor, S.Srinivasan ; J. Electroanal. Chem. 132(25) (1982) 137.
[48] J.C. Huang, R.K. Sen, E.Yeager ; J. Electrochem. Soc. 126 (1979) 786.
[49] A.J.Appleby ; J. Electrochem. Soc. 117(3) (1970) 328.
[50] A.J. Appleby ; J. Electrochem. Soc. 117(3) (1970) 641.
[51] P.O.Olapade, J.P.Meyers, R.L. Borup, R. Mukundan ; J. Electrochem. Soc. 158(6) (2011) B639.
[52] K.Klinedist, J.A.S.Bett, J.Macdonald, P.Stonehart ; J. Electroanal. Chem. 57(3) (1974) 281.
[53] A.Bergmann, D.Gerteisen, T.Kurz ; Fuel Cells 10(2) (2010) 278.
[54] J.Zhang, Z.Xiea, J.Zhanga, Y.Tanga, C.Songa, T.Navessina, et al. ; J. Power Sources 160 (2006) 872.
[55] T.Gu, S.Shimpalee, J.W.Van Zee, C.Y.Chen ; J. Power Sources 195 (2010) 8194.
[56] D.I.McDonald, J.R.Boyack ; J. Chem. Eng. Data 14(3) (1969) 380.

[57] C.Boyer, S.Gamburzev, O.Velev, S.Srinivasan, A.J.Appleby ; Electrochim. Acta 43 (1998) 3703.
[58] M.L.Perry, J.Newman, E.J.Cairns ; J. Electrochem. Soc. 145(1) (1998) 5.
[59] G.Wang, P.P.Mukherjee, C-Y Wang ; Electrochim. Acta 51 (2006) 3139.
[60] Z.Liu, J.S.Wainright, M.H.Litt, R.F.Savinell ; Electrochim. Acta 51 (2006) 3914.
[61] B.P.Boudreau ; Geochim. Cosmochim. Acta 60(16) (1996) 3139.
[62] L.Shen, Z.Chen ; Chem. Eng. Sci. 62 (2007) 3748.
[63] E.Passalacqua, F.Lufrano, G.Squadrito, A.Patti, L.Giorgi ; Electrochim. Acta 46 (2001) 799.
[64] Z.D.Wei, H.B.Ran, X.A.Liu, Y.Liu, C.X.Sun, S.H.Chan, et al. ; Electrochim. Acta 51 (2006) 3091.
[65] S.Litser, G.McLean ; J. Power Sources 130 (2004) 61.
[66] R.E.Benfield, A.Filipponi, N.Morgante, G.Schmid ; J. Organomet. Chem. 573 (1999) 299.
[67] A.T.Shuvaeu, PhM Ovsyannikov, T.A.Lyubeznova ; Physica B 208-209 (1995) 571.
[68] W.M.Haynes ; CRC Handbook of chemistry and physics. 91st ed. Boca Raton: CRC Press (2010).
[69] J.A.Bett, K.Kinoshita, P.Stonehart ; J. Catal., 35 (1974) 307.
[70] Y.L.Ma, J.S.Wainright, M.H.Litt, R.F.Savinell ; J. Electrochem. Soc. 151(1) (2004) A8.
[71] I.Okae, S.Kato, A.Seya, T.Kamonoshita ; The chemical society of Japan 67th spring meeting; (1990) 148.
[72] M.Williams, A.Suzuki, A.Miyamoto ; ECS Trans. Anal. Model 30(1) (2010) 207.
[73] R.S.Gemmen, M.C.Williams, K.Gerdes ; J. Power Sources 184 (2008) 251.
[74] D.Bronin, B.Kuzin, D.Osinkin, I.Yaroslavtsev ; Proceedings of the 8th European SOFC Conference. Oberrohrdorf, Switzerland: Lucerne, EFCF (2008) B1001.
[75] R.Gemmen, M.Williams, G.Richards ; Process Perform 35(1) (2011) 621.

Chapter 5
Long-term cell degradation mechanism in HT-PEMFC

5.1 Introduction

As mentioned in the chapter 1, several studies have reported the results of the long-term power generation tests conducted on HT-PEMFC [1–5]. Zhang et al. reported that higher cell performance was achieved as the operating temperature approached 200℃ [5]. In addition, lifetimes exceeding 10,000h have been reported by research groups at BASF and Samsung [6, 7], and these PEMFCs are considered to be closest to commercial viability. However, there have been very few reports on the mechanism underlying the deterioration of such cells. Although some studies have been carried out on the reduction in durability during 500h of operation at 150℃ [4], nothing has been reported concerning the causes of cell deterioration over longer periods.

In the present study, in order to clarify the causes of long-term cell deterioration, five identical cells were tested for periods of up to 17,860h, and their membrane electrode assemblies (MEAs) were then removed and subjected to microstructural analysis. The cells used PBI membranes doped with phosphoric acid. The deterioration mechanism was investigated based on chronological changes in the cell voltage and internal cell resistance, chronocoulometry (CC) measurements of the hydrogen crossover, and post-analysis using transmission electron microscopy (TEM) and electron probe micro-analysis (EPMA).

5.2 Experimental

5.2.1 Preparation of PBI electrolyte membrane

PBI membranes (5.5cm × 5.5cm, ca. 40μm thick) provided by the joint research institute were immersed in an 85% phosphoric acid solution and heated to 40℃ for 40min to dope the membranes [8]. All of the membranes used in the present study were subjected to exactly the same doping procedure. The doping level was determined by measuring the weights of the membranes before and after doping using a precision electronic balance (AUW120D, Shimadzu Corp., Japan); this was characterized by the ratio of the weight of phosphoric acid doped into the membrane to the weight of the

membrane after doping with phosphoric acid.

5.2.2 Production of electrodes

A sheet of carbon paper with a thickness of 280μm (TGP-H090, Toray Corp., Japan) was used as the gas diffusion layer. A mixed powder of Ketchen Black(EC-600JD,Akzo Nobel Corp.,UK)and polytetrafluoroethylene (PTFE, DuPont) in a weight ratio of 65:35 was applied to the carbon paper using a dry coating device [8–11] until it formed a coating with a density of 2mgcm^{-2}. This was then heated at 350℃ in an atmospheric oven, and the surface was leveled using a roller press [8–11] to produce a filled carbon layer.

A catalyst ink was then prepared by mixing polyvinylidene fluoride (PVDF, Kureha Corp., Japan), Pt-supported and PtCo-supported on Ketchen Black powder (carbon/metal: 50/50, TKK Corp., Japan) [8] and N-methyl pyrrolidone (NMP, Sigma-Aldrich Corp., USA) with agitation for 60h. To produce the electrode, the catalyst ink was applied using a wet-coating method onto carbon paper coated with a mixed powder of carbon and PTFE prepared using a dry-coating method. The resulting structure was then dried for 1h at 80℃ in air, and finally held in a vacuum oven at 160℃ for 25h to remove the NMP [8]. The amount of supported Pt was approximately 0.8mgcm^{-2} for both the anode and cathode electrodes.

5.2.3 Single cell assembly

The electrolyte membrane doped with phosphoric acid was sandwiched between two electrodes prepared as described in Section 5.2.2 to produce the MEA. This was in turn sandwiched between current collector and bi-polar plates made of carbon, on which a serpentine flow pattern was machined. The flow pattern was designed by the Japan Automobile Research Institute and had a reaction area of 5cm×5cm. This assembly was further sandwiched between a pair of stainless steel end plates with a rubber heater attached to their outermost surfaces and tightened using eight M6 bolts to produce a single cell [8]. Five single cells were prepared, and these are referred to as Cells A, B, C, D and E.

5.2.4 Long-term power generation durability tests

The five single cells described in Section 5.2.3 were mounted on a fuel cell station (Kofloc Corp., Japan) equipped with mass flow controllers, an

electronic loading device (Kikusui Electronics Corp., Japan) for controlling the electric current, an AC milliohm tester (Model 3566, Tsuruga Electric Corp., Japan) with a constant frequency of 1kHz, and a personal computer for equipment monitoring and data output. Fig.5.1 shows a schematic diagram of the fuel cell station used in this study.

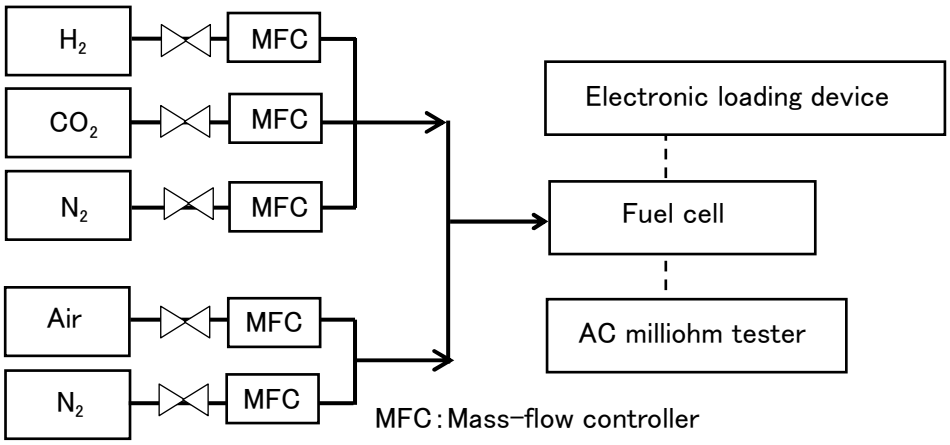

Fig.5.1 Schematic diagram of the fuel cell station used in this study.

Table 5.1 shows the test conditions of Cells A, B, C, D and E. Cell A was used as a reference and did not undergo power generation. It was heated to 150℃ and was kept at that temperature for 5h while supplying 130mL min^{-1} (stoich: 3.7) of nitrogen to both the anode and cathode sides. It was then cooled down and its MEA was removed for analysis. Such a stoichiometry was decided by the lowest flow rate limit of the fuel cell station.

For Cells B, C, D and E, power generation tests were conducted at a cell temperature of 150℃ and a current density of 0.2Acm^{-2}, controlled using an electronic loading device while supplying 130mLin^{-1} (stoich: 3.7) of pure hydrogen and 310m$Lmin^{-1}$ (stoich: 3.7) of air to the anode and cathode sides, respectively. Neither of the reaction gases were humidified [8]. All power generation tests were conducted under atmospheric conditions. For Cells B, C and D, long-term durability tests were conducted for 2,000, 12,000, and 15,000h, respectively, after which power generation was terminated. For Cell E, the long-term durability test was not terminated until the cell voltage had dropped by 10% from its peak value.

During the long-term tests, chronological changes of the cell voltage, internal cell resistance and leak current were monitored. The internal resistance was measured using the abovementioned AC milliohm tester at a

constant frequency of 1kHz. A potentiostat-galvanostat (HZ-5000 HAG-3001, Hokuto Denko Corp., Japan), was used for CC measurements of the hydrogen crossover rate through the PBI membrane [10].

During the measurements, the cells were operated at 150℃ while providing pure hydrogen to the anode and nitrogen to the cathode. A voltage of 0.2V was applied across the cell so that hydrogen crossing the membrane was electrochemically oxidized. To measure the hydrogen crossover rate, the hydrogen and nitrogen flow rates were controlled at 300 and 500mLmin^{-1}, respectively.

Table5.1 Test conditions of Cells A, B, C, D and E. Cell

	Cell A	Cell B	Cell C	Cell D	Cell E
Cell temperature	150℃				
Anode	Nitrogen 130mLmin-1	Hydrogen 130mLmin-1			
Cathode	Nitrogen 130mLmin-1	Air 310mLmin-1			
Current density	-	0.2 Acm^{-2}			
Power generation time(h)	To be kept for 5h at 150℃	2000	12,000	15,000	17,800

5.2.5 Post-analysis

TEM (JEM-2010DM, JEOL Ltd. Japan) observations were conducted on the electrode catalysts from both the anode and cathode of Cells A and E, following the tests described in Section 5.2.4. Cross sections of the MEAs, consisting of the catalyst layer (CL), gas diffusion layer (GDL) and the intermediate microporous layer (MPL) were investigated using EPMA (EPMA-1610, Shimadzu, Japan).

5.3. Results

5.3.1 Long-term durability test

Fig.5.2 shows the chronological change in the cell voltage and internal resistance during the power generation test conducted on Cell E As described earlier, this test was carried out until the cell voltage decreased by 10% from its peak value, which occurred following 17,860h of operation. As seen in the figure, the cell voltage initially increased and reached a peak after about 500h of operation. It then declined very gradually over a period of about 14,000h with three temporarily drops and recoveries due to emergency stops. It subsequently dropped more rapidly, with a corresponding increase in internal resistance.

In order to investigate the mechanism behind the gradual decrease in performance up to 14,000h and the subsequent more rapid degradation, power generation tests were carried out on Cells B, C and D for 2,000, 12,000, and 15,000h, respectively. The results are described in the next section.

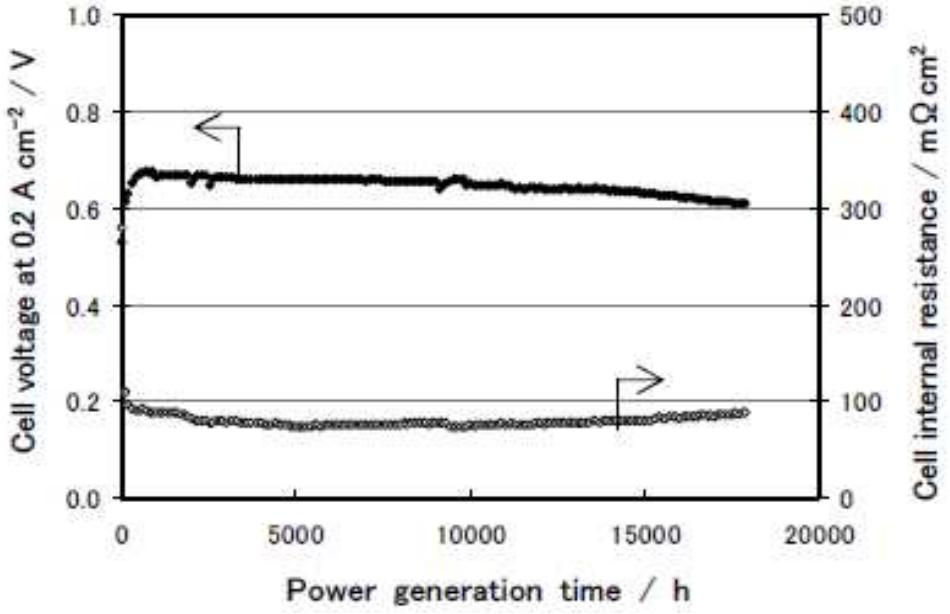

Fig.5.2 Long-term power generation test results for Cell E operated until its cell voltage dropped by 10% from it peak value (17,860h).

5.3.2 Investigation of degradation mechanism

Fig. 5.3 shows the chronological changes in cell voltage for Cells B, C, D and E. As can be seen, all cells showed a similar drop in voltage until the end of their testing period. In the figure, the solid line represents the loss of

phosphoric acid per unit area, calculated based on the amount of evaporation at 150℃, as described in a previous report [11,12]. The rates of phosphoric acid depletion and cell voltage reduction are in good agreement until around 14,000h. However, for periods longer than this, a faster drop off in voltage is seen.

Thus, although it cannot be denied that the depletion of phosphoric acid has a substantial effect on reducing the cell voltage over the entire cell lifetime, another contribution is thought to be an increase in the size of the catalyst particles [4]. To verify this, the MEAs were removed from Cells A and E and the catalysts were analyzed using TEM.

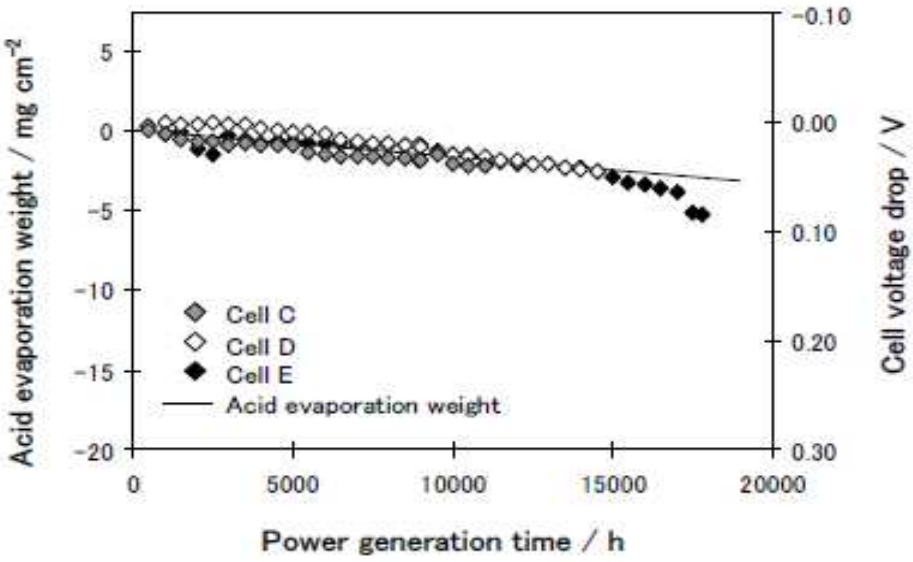

Fig.5.3 Long-term power generation test results for Cells B, C, D, and E, operated for 2000, 12,000, 15,000, and 17,860 h, respectively

5.3.3 TEM observations of electrode catalysts

Fig. 5.4(a) and (b) shows TEM images of the catalysts from the anodes of Cells A and E, respectively, and Fig.5.4(c) shows the Pt particle size distributions obtained from these images including Cells C and D. The distributions are seen to be very similar, indicating that very little particle growth occurred in the catalyst of Cell E during 17,860h of power generation, although there is a slight decrease in the number of small particles.

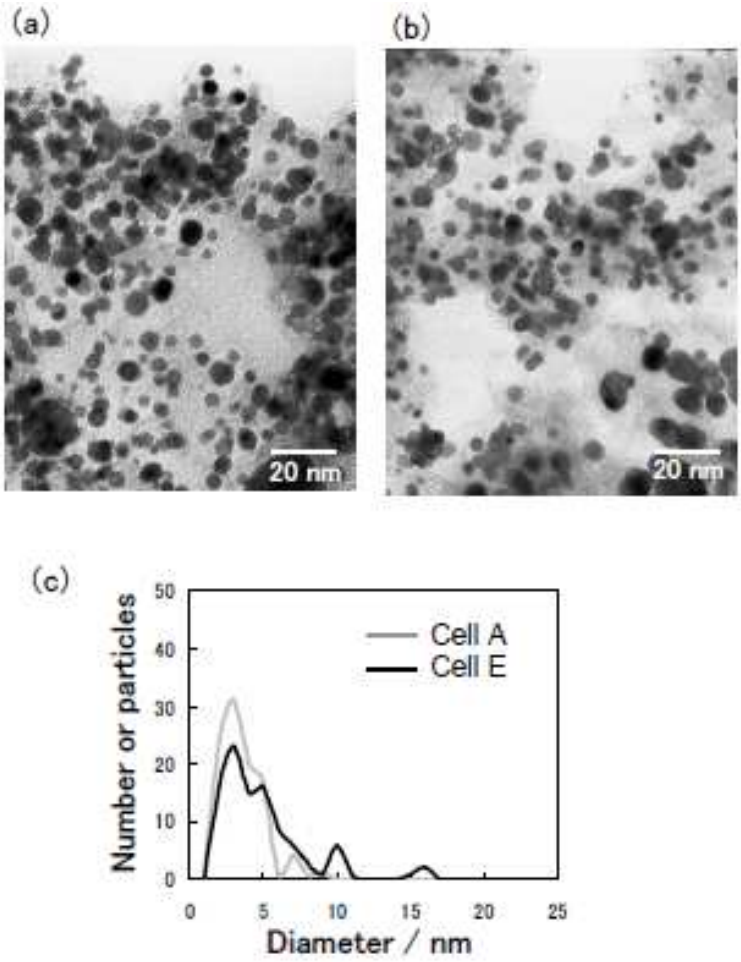

Fig.5.4 Comparison of anode catalysts. (a) TEM image of anode catalyst of Cell A (0 h), (b) TEM image of anode catalyst of Cell E (17860 h), and (c) size distributions of anode Pt catalyst particles.

Fig.5.5 (a-1) and (b-1) shows TEM images of the catalysts from the cathodes of Cells A and E, respectively, and Fig.5.5 (c) shows the corresponding particle size distribution. In this case, a significant increase in particle size appears to have occurred in Cell E; the average particle diameters for Cells A and E are 4.6 and 7.9nm, respectively. In particular, a large decrease in the number of small particles is apparent following 17,860h of power generation.

Fig.5.5 (a-2) and (b-2) shows higher magnification TEM images of the regions indicated in Fig.5.5 (a-1) and (b-1), respectively. In Cell A, the carbon support for the Pt catalyst had a layered graphite-like structure with a lattice spacing of 0.34nm. However, in Cell E, it appeared to have become amorphous during the long-term test, possibly due to oxidation of the carbon.

In order to determine whether there is any direct correlation among the growth of Pt particles, oxidation of the carbon support and the decline in the cell voltage, EPMA observations were conducted on cross sections of the MEAs from Cells A, C, D and E.

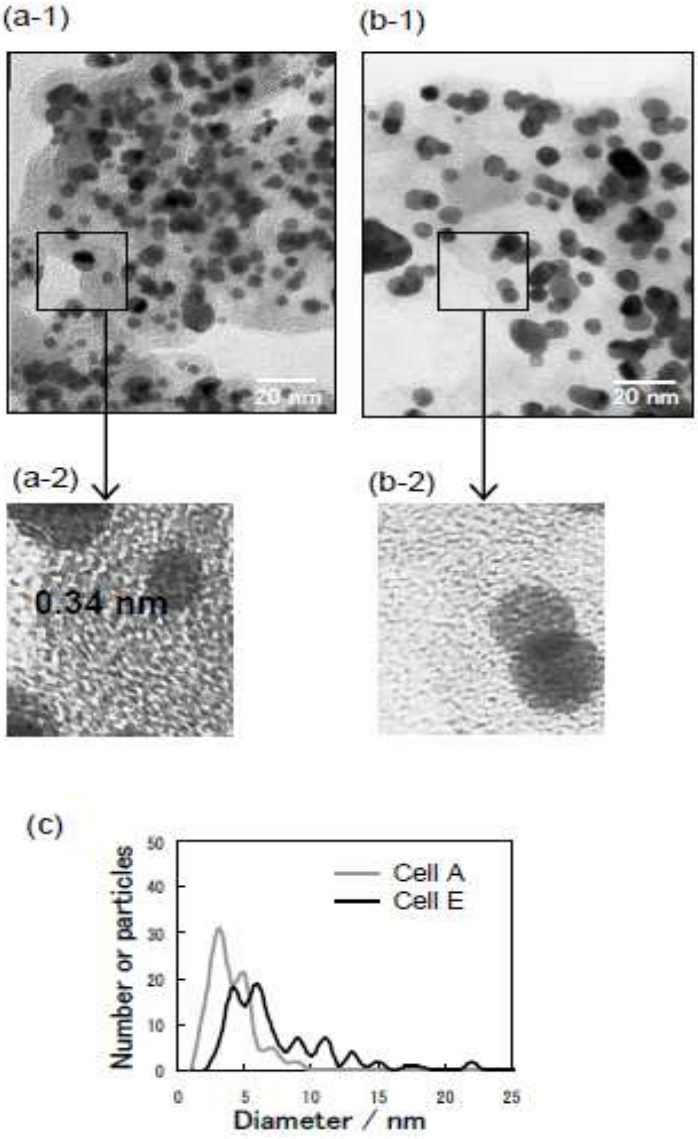

Fig.5.5 Comparison of cathode catalysts. (a-1) TEM image of cathode catalyst of Cell A (0h), (a-2) magnified image of (a-1), (b-1) TEM image of cathode catalyst of Cell E (17,860h), (b-2) magnified image of (b-1), and (c) size distributions of cathode Pt catalyst particles.

5.3.4 EPMA observation of MEA cross sections

Figs.5.6(a), 5.5(b), 5.6(c) and (d) show the Pt distributions determined by EPMA for cross sections of MEAs from Cells A, C, D and E, respectively.

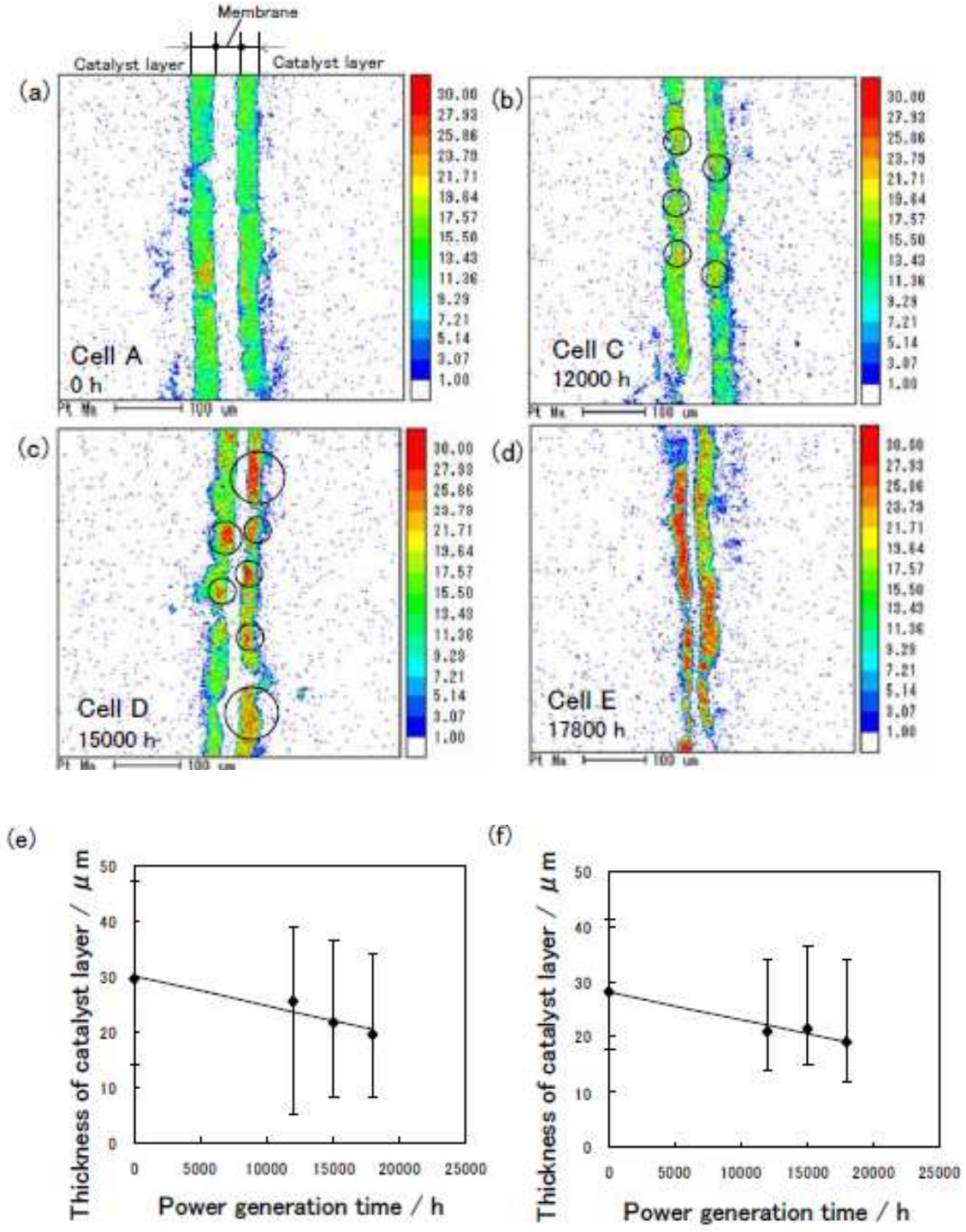

Fig.5.6 EPMA Pt concentration analysis for cross sections of MEAs. (a) Pt concentration distribution in Cell A (0 h), (b) Pt concentration distribution in Cell C (12,000 h), (c) Pt concentration distribution in Cell D (15,000 h), (d) Pt concentration distribution in Cell E (17,860 h), (e) change in anode catalyst layer thickness with time, and (f) change in cathode catalyst layer thickness with time.

As shown in Fig.5.6 (a), the Pt concentration was initially highly uniform in

both the anode and cathode catalyst layers. However, as shown in Fig.5.6 (b), following 12,000h of operation, the Pt concentration in the circled areas became slightly higher than that in other areas. Furthermore, as shown in Figs.5.6(c) and (d), this trend continued as the power generation time increased. Particularly high localized Pt concentrations were observed in both catalyst layers in Cell E following 17,860h of operation. In addition, the catalyst layers, as a whole, became thinner with increasing power generation time. Fig.5.6 (e) and (f) shows the change in the thickness of the anode and cathode catalyst layers, respectively, as a function of testing time. The data points correspond to an average of fifty thickness measurements, and the errors bars represent the range of variations among the measurements. It can be seen that for both catalyst layers, the average thickness decreases, which correspond to the whole thickness reductions, roughly linearly with time.

Fig.5.7 (a)-(d) shows SEM images of cross sections of the MEAs from Cells A, C, D and E, respectively. It can be seen that the membrane thicknesses also decreases with increasing power generation time. This change in thickness is plotted in Fig.5.7(e), where the data points are again averaged over fifty measurements and the range of variations is shown as error bars. The membrane thickness is seen to decrease very gradually over a period of about 14,000h, after which it decreases more dramatically. These results are in good agreement with the decrease in cell voltage during the long-term power tests, as seen in Figs.5.2 and 5.3.

Fig. 5.8(a)-(d) shows the phosphorus distributions determined by EPMA for cross sections of MEAs from Cells A, C, D and E, respectively. It is thought that these correspond to the phosphoric acid distributions. As seen Fig.5.8(a), the initial phosphorus concentration was very low in both catalyst layers in Cell A. However, Fig.5.8(b) shows that following 12,000h of power generation, it increased substantially, indicating that migration of phosphoric acid from the membrane occurred. The phosphoric acid appears to be uniformly distributed in both catalyst layers. Following 15,000h of operation, as shown in Fig.5.8(c), this distribution became non-uniform and regions depleted of phosphoric acid began to appear in both catalyst layers. Such depletion of phosphoric acid would lead to a reduction in the active area of the Pt catalysts, and corresponds to the period following 14,000h of

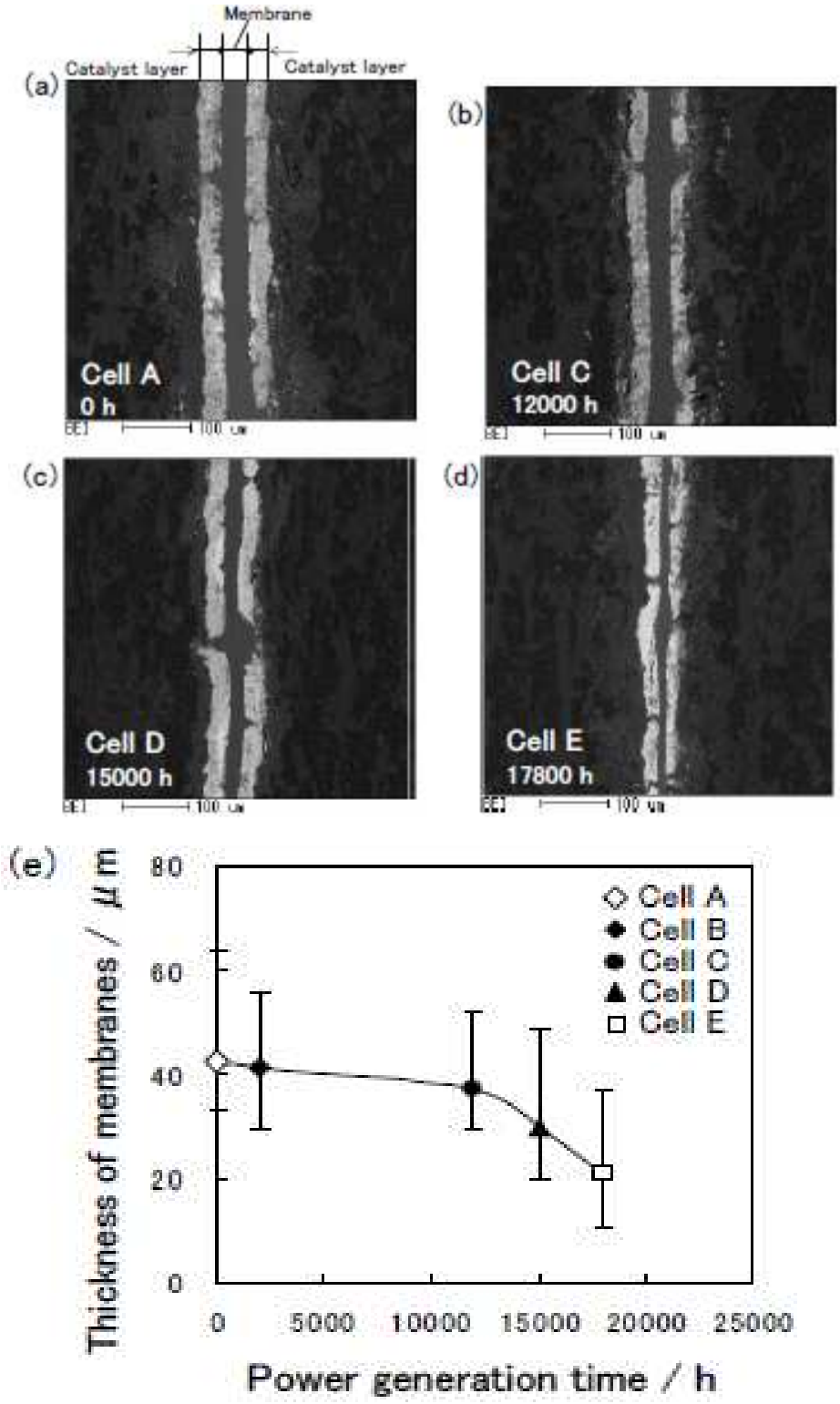

Fig.5.7 EPMA of cross sections of MEAs. (a) SEM image of Cell A (0h), (b) SEM image of Cell C (12,000h), (c) SEM image of Cell D (15,000h), (d) SEM image of Cell E (17,860h), and (e) change in membrane thickness with time.

operation when an accelerated decrease in the cell voltage occurs. Finally,

as indicated by the circles in Fig.5.8(d), following 17,860h of power generation, a further increase in the number of depleted regions occurred, accompanied by rapid thinning of the membrane. In order to evaluate the impact of membrane thinning and phosphoric acid migration on the cross leakage, leakage currents were measured for Cells C, D and E.

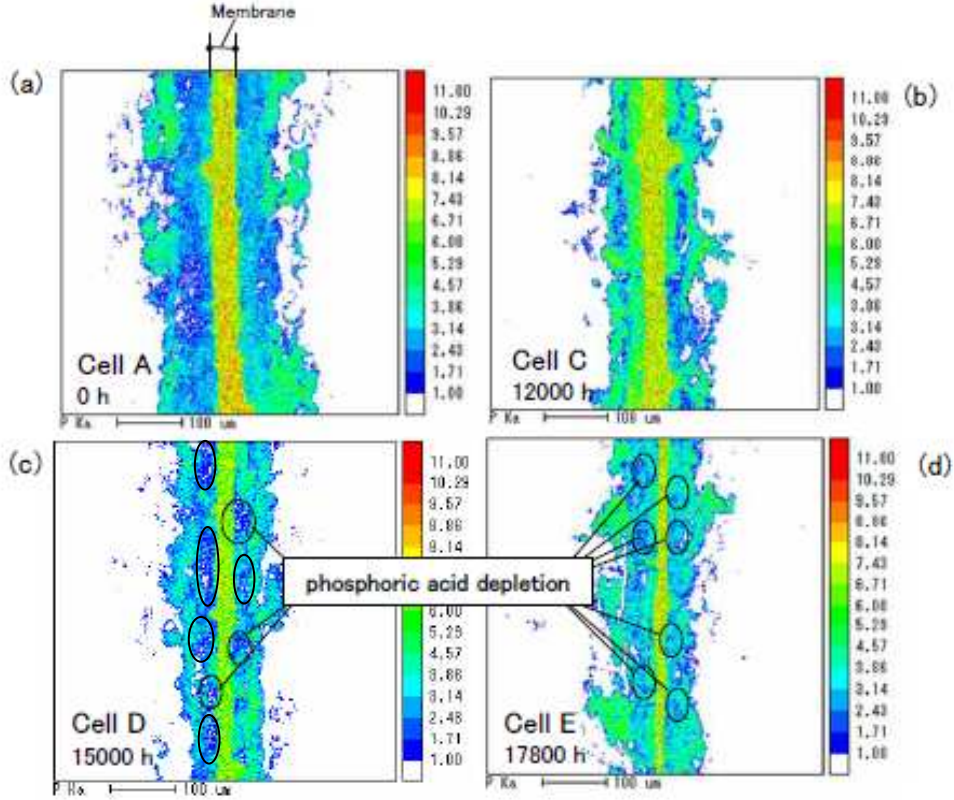

Fig.5.8 EPMA phosphorus concentration analysis for cross sections of MEAs. (a) EPMA image of Cell A (0h). The concentration of phosphoric acid is very low in both catalyst layers; (b) EPMA image of Cell C (12,000h). A large amount of phosphoric acid is distributed uniformly in the catalyst layers; (c) EPMA image of Cell D (15,000h). Depletion of phosphoric acid is observed in the catalyst layers; (d) EPMA image of Cell E (17,860h). Increased number of phosphoric acid depleted regions observed in addition to membrane thinning.

5.3.5 Measurement of leakage current

Fig.5.9 shows the increase in the leakage current with time for Cells C, D and E. The relationship is seen to be logarithmic, with a very large leakage current occurring after 17,860 h of operation.

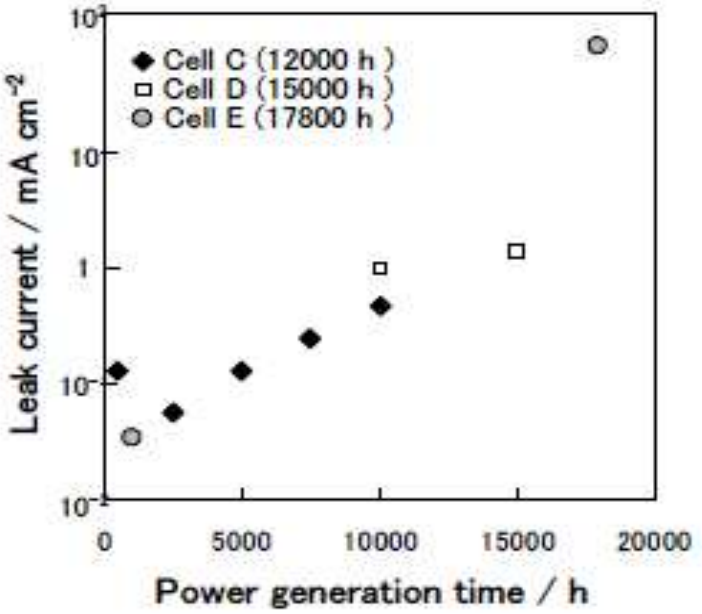

Fig.5.9 Change in leakage current with time for Cells C, D and E.

5.4 Discussion

5.4.1 Influence of Pt catalyst and carbon support degradation on cell voltage drop

From in Fig.5.5(a-2) and (b-2), following 17,860h of operation, it seems that the carbon support changed from having a layered graphite-like structure to an amorphous structure. Furthermore, the EPMA results shown in Fig.5.6 indicate that both the anode and cathode catalyst layers became thinner as a linear function of power generation time, and their Pt particles became agglomerated. These results suggest that a large amount of the carbon support became oxidized and was removed as carbon dioxide. However, taking into account the linear dependence of the catalyst layer thinning on the power generation time, it is unlikely that carbon oxidization was responsible for the enhanced drop in the cell voltage that was observed from about 14,000h.

On the other hand, since smaller catalyst particles are likely to agglomerate more easily, particle growth is expected to be more rapid in the early stages of power generation. This makes it unlikely that such particle growth was responsible for the enhanced drop in the cell voltage in the later stages of operation. In fact, growth of Pt catalyst particles during power generation at 150℃ has been reported within a relatively short period of

approximately 500h [11]. In addition, Zhai et al. reported that Pt aggregation occurs in the early stages of power generation and reduces the cell performance due to a reduction in the specific surface area of the Pt particles and an increase in the reaction resistance [4]. Considering these results, the reduction in cell voltage of approximately 20mV in the initial stage of the durability test is considered to be caused by Pt particle growth [11].

5.4.2 Influence of membrane degradation on cell voltage drop

As shown in Fig.5.7, the membrane thickness decreased very gradually up to about 14,000h, and thereafter more rapidly, which is similar to the behavior of the cell voltage. As a result, the leakage current also increased, which is thought to have accelerated the degradation process. Furthermore, as shown in Fig.5.9, local depletion of phosphoric acid occurred in both the anode and cathode catalyst layers, resulting in a reduction in the active areas of the catalyst layers.

In order to verify the correlation between membrane thinning and phosphoric acid depletion, the distributions of phosphorus and nitrogen were determined using EPMA. The phosphorus is associated with phosphoric acid whereas nitrogen is a constituent element of the PBI membrane, and its presence in the catalyst layers would therefore indicate dissolution of the membrane.

Fig.5.10 (a) and (b) shows the distributions of phosphorus and nitrogen, respectively, in the MEA from Cell E. The circles indicate regions where the concentrations of both phosphorus and nitrogen in the catalyst layers are high. This suggests that large regions of the membrane were dissolved during power generation and, together with the phosphoric acid, migrated into the catalyst layers. The migration led to large areas of the catalyst layers being depleted of phosphoric acid, resulting in a reduction in the active area. This is thought to be the reason for the accelerated drop in the cell voltage following 14,000h of operation.

The membrane used in this study was not chemically bridged, which is thought to lead to the dissolution of membrane and finally its fragmented moieties. Higher durability is expected by using a bridged membrane.

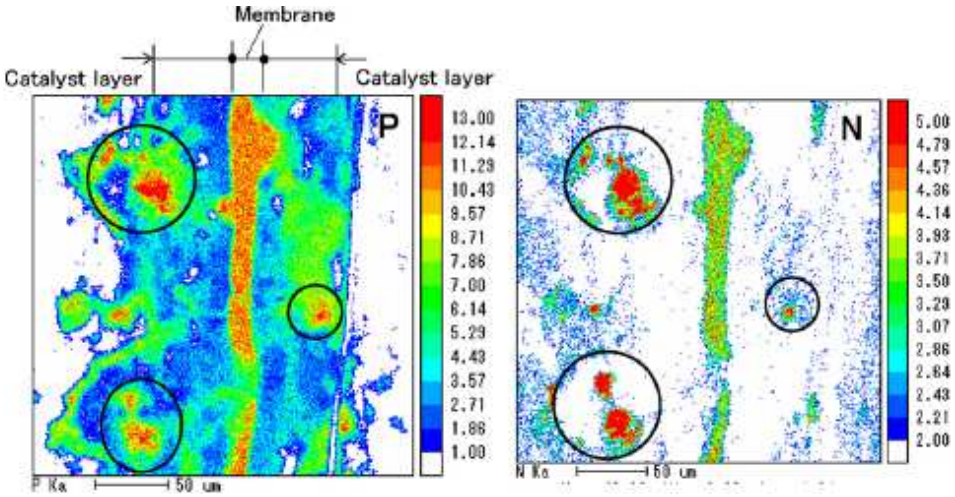

Fig.5.10 EPMA of cross sections of MEAs from Cell E (17,860 h). (a) Phosphorus distribution, (b) Nitrogen distribution.

5.5. Conclusions

For HT-PEMFCs using PBI membranes doped with phosphoric acid, five identical single cells were prepared and long-term power generation tests were conducted at a temperature of 150℃ and a current density of 0.2Acm^{-2} for periods of up to 17,860h. Following the tests, the MEAs from the cells were analyzed using TEM and EPMA.

The results indicated that the cell voltage declined very gradually until 14,000h, after which a more rapid decrease occurred. The former was guessed to be caused by the active area decrease due to catalyst agglomeration and so on. And the latter was found to correlate well with decreases in the membrane thickness. It was also found that parts of the membrane became dissolved and migrated together with the phosphoric acid into the catalyst layers. Regions of the catalyst layers that were depleted of phosphoric acid were identified, which resulted in a reduction in the active area, which is thought to be the cause of the accelerated drop in the cell voltage after about 14,000h of operation.

References

[1] Q.Li, J.O.Jensen, R.F.Savinell, N.J.Bjerrum ; Prog. Polym. Sci. 34 (2009) 449.

[2] J.Parrondo, F.Mijangos, B.Rambabu ; J.Power Sources 195 (2010) 3977.

[3] J.Lobato, P.Canizares, M.A.Rodrigo ,F.J.Pinar, D.Ubeda ; J.Power Sources 196 (2011) 196.

[4] Y.Zhai, H.Zhang, D.Xing, Z.G.Shao ; J.Power Sources 164 (2007) 126.

[5] J.Zhang, Y.Tang, C.Song, J.Zhang ; J.Power Sources 172(2007)163.

[6] A.Sounai, K.Sakai ; Prog. of the 13th Fuel Cell FCDIC Symposium, (2006) 125.

[7] J.Baurmeister, T.Kohno ; Prog. of the 13th Fuel Cell FCDIC Symposium (2006) 122.

[8] Y. Oono, A. Sounai, M. Hori ; J. Power Sources 189 (2009) 943.

[9] J.Yu, Y.Yoshikawa, T.Matsuura, M.N.Islam, M.Hori ; Electrochem. Solid-State Lett.8(3) (2005) A152.

[10] J.Yu, T.Matsuura, Y.Yoshikawa, M.N.Islam, M.Hori ; Electrochem. Solid-State Lett. 8(3) (2005) A156.

[11] Y.Oono, T.Fukuda, A.Sounai, M.Hori ; J. Power Sources 195 (2010)1007.

[12] I.Okae, S.Kato, A.Seya, T.Kamonoshita ; The Chemical Society of Japan 67th Spring Meeting (1990) 148.

Chapter 6
Study on Prolongation of Cell Life of HT-PEMFCs

6.1 Introduction

Investigations have been carried out on HT-PEMFCs based on phosphoric-acid-doped chemically cross-linked poly (2.5-benzimidazole) (AB-PBI) and PBI membranes, from and the viewpoint of not only the membrane conductivity and heat resistance [1, 2]. However, there have been very few reports on the mechanism underlying the deterioration of such cells using PBI and AB-PBI membranes [1]. Although one study has been carried out on the reduction in performance during 500h of operation at 150℃ [3], very little has been reported concerning the causes of cell deterioration over longer periods. Based on long-term power generation tests exceeding two years, the present authors clarified the deterioration mechanism in HT-PEMFCs and showed that lifetimes exceeding 20,000h can be achieved by improving the stability of the electrolyte membrane [4].

In the present study, as part of a series of investigations on the durability of HT-PEMFCs [4, 5], long-term power generation tests were carried out on cells using ABPBI membranes rather than the PBI membranes used in a previous study [4]. The AB-PBI membranes were pre-doped with phosphoric acid [1, 6, 7] and were expected to be more stable than PBI membranes due to the presence of cross-linking. The purpose of this study was thus to investigate whether the stability of the membrane itself is the main factor influencing cell deterioration for operation times up to 20,000h. Two such AB-PBI membranes were used in HT-PEMFCs and operated for 1,000 and 17,500h. The membrane electrode assembly (MEA) was then removed from the cells and evaluated using electron probe microanalysis (EPMA). To clarify the effect of the membrane on cell deterioration, the electrical and EPMA results for the AB-PBI containing cell tested for 17,500h in the present study were compared with those for the PBI-based cell tested for 17,800h in a previous study [4].

6.2 Experimental

6.2.1 Acid-doping

Eight AB-PBI membranes with an area of 2×2cm^2 and a thickness of

approximately 40μm were prepared, and their weights and dimensions were measured using a high-precision balance (AUW120D Shimadzu Corp., Japan) and micrometer, respectively [8]. Of these membranes, three were immersed in 75%, 85% and 95% phosphoric acid solutions at 60°C for 60min. Five others were immersed in an 85% phosphoric acid solution for 100 min at 40°C, 10min at 60°C, and 5min at 80, 100 and 120°C. In order to avoid condensation due to evaporation during heating, the phosphoric acid was kept in a covered container in a water bath at the given temperature. The membranes were removed from the container at intervals, their surfaces were wiped, and their weights and dimensions were measured. In this study, the acid-doping level was defined as the ratio of the "weight of phosphoric acid doped into the membrane" to the "weight of the membrane after doping with phosphoric acid."

6.2.2 Preparation of AB-PBI Electrolyte Membrane

AB-PBI membranes with dimensions of 5.5×5.5cm^2 and a thickness of 40μm (FuMA-Tech GmbH, Germany) were prepared. For power generation tests to evaluate the initial cell performance, three electrolyte AB-PBI membranes with phosphoric acid doping levels of 68%, 72% and 76% were produced by immersion in an 85% phosphoric acid solution and heating to 40°C for approximately 6, 8, and 12min, respectively. For power generation tests to evaluate the long-term durability, two membranes with phosphoric acid doping levels of 78% were produced by immersion in an 85% phosphoric acid solution and heating to 40°C for approximately 20min.

6.2.3 Production of Electrodes

A sheet of carbon paper with a thickness of 280μm (TGP-H-090, Toray Corp., Japan) was used as the gas diffusion layer. A mixed powder of Ketchen Black (EC-600JD, Akzo Nobel Corp., UK) and polytetrafluoroethylene (PTFE; DuPont) in a weight ratio of 65:35 was applied to the carbon paper using a dry coating device [8-10] until a 2$mgcm^{-2}$ coat was formed. This was then heated at 350℃ in an atmospheric oven, and the surface was leveled by a roller press [8-10] to produce a filled carbon layer.

A catalyst ink was then prepared by mixing polyvinylidene fluoride (PVDF; Kureha Corp., Japan), Pt- and PtCo-supporting Ketchen Black powder (carbon/metal: 50/50, TKK Corp., Japan) [4, 5, 8] and N-methyl

pyrrolidone (NMP; Sigma-Aldrich Corp., USA) with agitation for 60h. To prepare the electrode, the catalyst ink was applied using a wet-coating method onto carbon paper coated with a mixed powder of carbon and PTFE prepared using a dry-coating method, dried for 1h at 80°C in air, and then finally held in a vacuum oven at 160°C for 25h to remove the NMP [4, 5, 8]. The amount of supported Pt was approximately 0.8mgcm^{-2} for both the anode and cathode electrodes.

6.2.4 Single Cell Assembly

To fabricate the MEA, an AB-PBI electrolyte membrane doped with phosphoric acid was sandwiched between the two electrodes prepared according to the method described in Section 6.2.3. This was then sandwiched between a pair of bipolar plates made of carbon, on which a serpentine flow pattern had been machined. The flow pattern was designed by Japan Automobile Research Institute (JARI) and had a reaction area of 5×5cm^2. This assembly was in turn sandwiched between current collector plates and stainless steel end plates, fitted with a rubber heater on the outermost surface, and tightened using eight M6 bolts to produce a single cell [4, 5, 8]. A total of five single cells were prepared, and were spilt into two groups of three and two, to evaluate the initial cell performance and long-term durability, respectively, during power generation tests. The cells in the latter group were labeled Cells F and G.

6.2.5 Single Cell Power Generation Tests

These five single cells were mounted on a fuel cell test stand (Kofloc Corp., Japan) equipped with mass flow controllers, an electronic loading device (Kikusui Electronics Corp., Japan) for controlling the electric current, an AC milliohm tester (Model 3566, Tsuruga Electric Corp., Japan) operating at a constant frequency of 1kHz, and a personal computer for equipment monitoring and data output. During all power generation tests, 130mLmin^{-1} (stoich: 3.7) of pure hydrogen and 310mLmin^{-1} (stoich: 3.7) of air were supplied to the anode and cathode sides, respectively, with none of the reaction gases being humidified [4, 5, 8]. All power generation processes were conducted under atmospheric conditions. Fig.6.1 shows a schematic diagram of the fuel cell station used in this study.

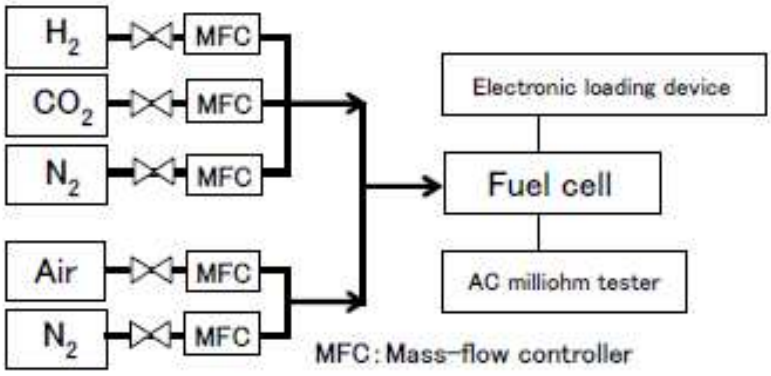

Fig.6.1 Schematic diagram of the fuel cell station used in this study.

To evaluate the dependence of the initial cell performance on the phosphoric acid doping level, power generation tests were conducted on three single cells with phosphoric acid doping levels of 68%, 72% and 76% at a cell temperature of 150°C and a current density of 0.2Acm^{-2} for 1,400 to 1,500h until the cell voltage reached its peak value and stabilized.

To evaluate the long-term durability of the cells with AB-PBI membranes, power generation tests were conducted on Cell F and G with a phosphoric acid doping level of 78% at a cell temperature of 150°C and a current density of 0.2Acm^{-2} for 1,000 and 17,500h, respectively. In this case, the rate of decrease in the cell voltage was calculated based on the difference between the peak cell voltage and that measured during long-term power generation. Table 6.1 shows the test conditions for Cells F and G together with those for Cells A, B, C, D and E used in the chapter 5..

Table6.1 Membrane and test conditions of Cell A, B, C, D and E used in the chapter 5 and Cell F and G used in this chapter.

	Cell A	Cell B	Cell C	Cell D	Cell E	Cell F	Cell G
Membrane	PBI					Chemically cross-linked AB-PBI	
Cell temp.	150℃						
Anode	N_2, 130mLmin^{-1}	H_2, 130mLmin^{-1}					
Cathode	N_2, 130mLmin^{-1}	Air, 310mLmin^{-1}					
Current density	—	0.2 Acm^{-2}					
Generation Time(h)	To be kept for 5h at 150℃	2,000	12,000	15,000	17,800	1,000	17,500
Remarks	Chapter 3, 5					Chapter 6	

6.2.6 Post Analyses

As a post analysis of long-term operated MEA, EPMA (EPMA-1610, Shimadzu, Japan) observations were carried out on a cross section of Cell G consisting of the catalyst layer (CL), the gas diffusion layer (GDL) and the microporous layer (MPL) between them.

6.3 Results

6.3.1 Acid-doping Level

As a preliminary to investigating the influence of the acid-doping level of the AB-PBI membranes on the cell voltage, measurements were carried out to verify that the acid-doping level was in fact controllable. Fig.6.2 show the change in the acid-doping level in 2×2cm^2 ABPBI membranes with immersion time in 75%, 85% and 95% phosphoric acid solutions at 60°C. As can be seen, the levels became almost saturated following immersion for 5 to 10min in any of the solutions, although the saturation level increased with concentration.

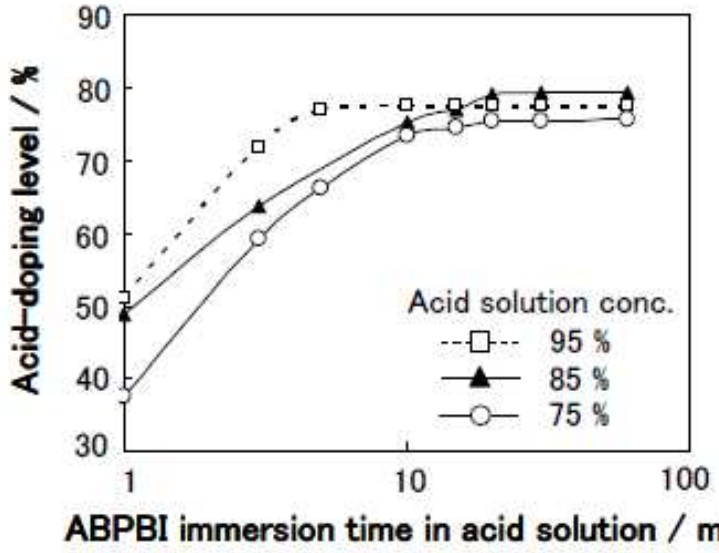

Fig.6.2 Influence of phosphoric acid solution concentration and immersion time on the acid-doping level of AB-PBI at fixing an acid solution temperature at 60℃

Fig.6.3 shows the change in the acid-doping level with immersion time in 85% phosphoric acid solutions at 40, 60, 80, 100 and 120°C. It can be clearly seen that, although the acid-doping level saturates at about 78% for all of the samples, the time for saturation to occur increases considerably at

lower temperatures. A similar trend was found for PBI in a previous study [8].

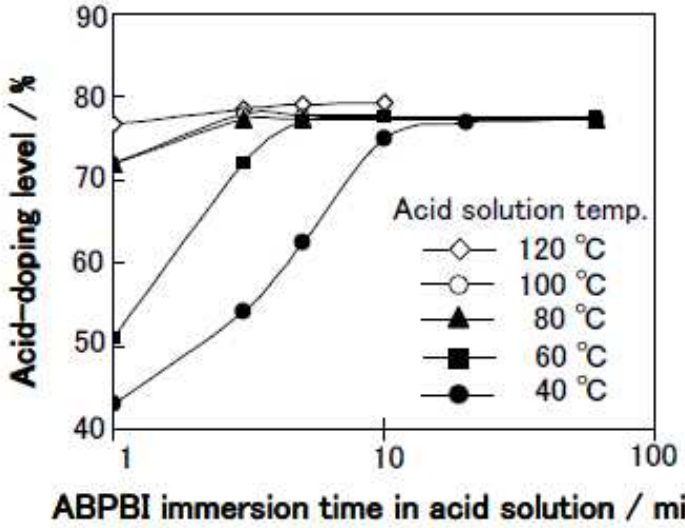

Fig.6.3 Influence of phosphoric acid solution temperature and immersion time on the acid-doping level of AB-PBI for fixing solution concentration at 85 %.

6.3.2 Evaluation of Initial Cell Performance

Figs.6.4 and 6.5 respectively show the change in the cell voltage and internal resistance with time for cells using ABPBI membranes with acid-doping levels of 68%, 72% and 76%, as seen in Fig.6.4, the cell voltages increased noticeably during the first few hundreds hours of power generation and then slowly began to saturate. The period of increase is

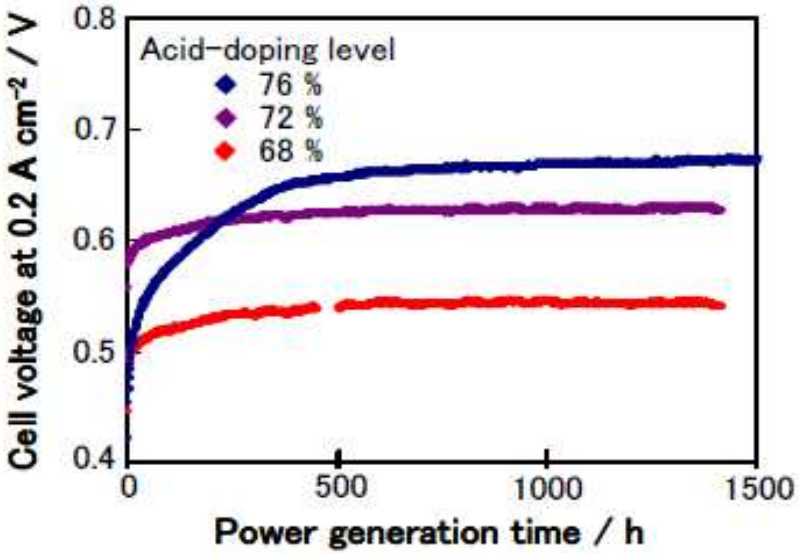

Fig.6.4 Change in cell voltage with time for cells with acid-doping levels of 68%, 72% and 76% at 0.2Acm^{-2} at 150℃.

thought to be the time required for evaporation of the solvent in the AB-PBI membrane and the CL. As the solvent evaporates, phosphoric acid flows slowly into the resulting pores and the proton conductivity gradually improves.

On the other hand, as shown in Fig.6.5, the cell internal resistance initially decreased with time before showing signs of saturation, which is also consistent with solvent evaporation.

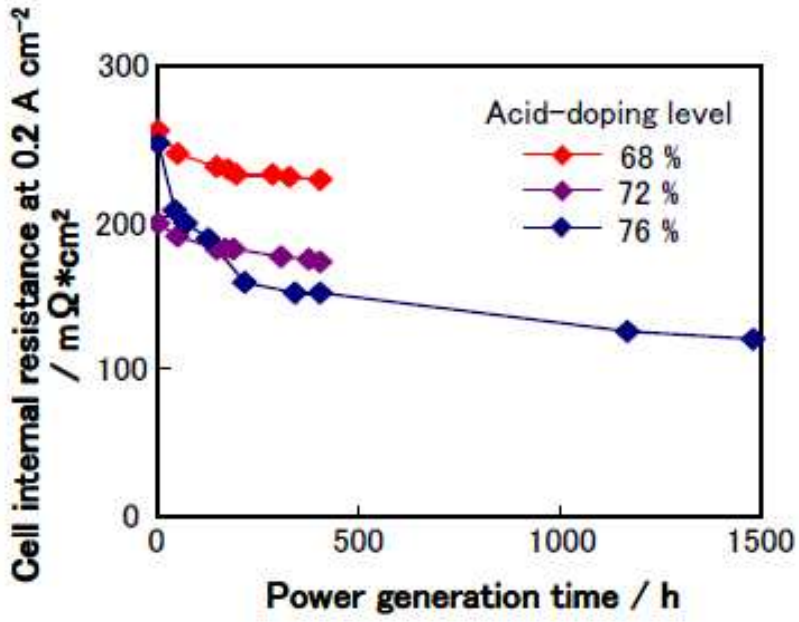

Fig.6.5 Change in cell internal resistance with time for cells with acid-doping levels of 68%, 72% and 76% at 0.2Acm^{-2} at 150℃.

6.3.3 Long-term Test of Evaluating Durability

Fig.6.6 shows the change in the voltage of Cell G with time during the long-term power generation test. The previously obtained results for Cell E with a PBI membrane are also shown for comparison. Although Cell G had not yet exhibited a 10% drop in cell voltage from its peak value, the power generation test was terminated at 17,500h, which is almost the same testing period as for Cell E. In the case of Cell E, the total voltage drop was 68mV, which represents a decrease of 10% relative to the peak cell voltage of 680mV. In contrast, for Cell G, a voltage drop of 32mV occurred, corresponding to a decrease of only 4.4%. In addition, the majority of this decrease was associated with accidental shutdowns of the test station during the testing period, rather than true degradation of the cell.

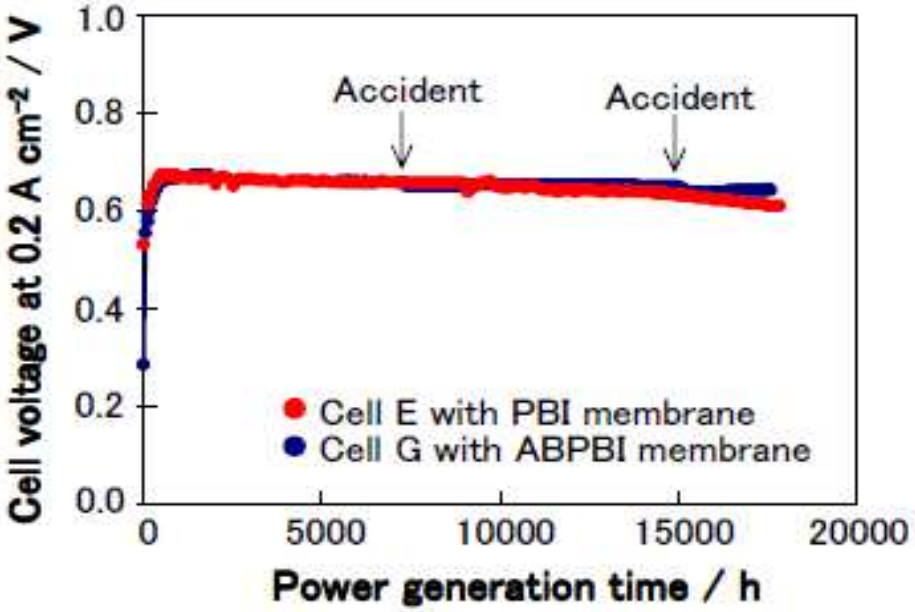

Fig.6.6 Change in cell voltage with time during long-term power generation tests on Cell G with AB-PBI membrane and Cell E with PBI membrane.

6.4 Discussion

6.4.1 Choice of Acid-doping Conditions

Fig.6.7 shows the relationship between the saturated acid-doping level of ABPBI membranes and the concentration of a 60℃ acid solution. The saturation values are obtained from Fig.6.2 for an immersion time of 60min. For the commonly used immersion treatment of 60min at 60℃ in an 85% phosphoric acid solution, the AB-PPI acid-doping level is about 78%.

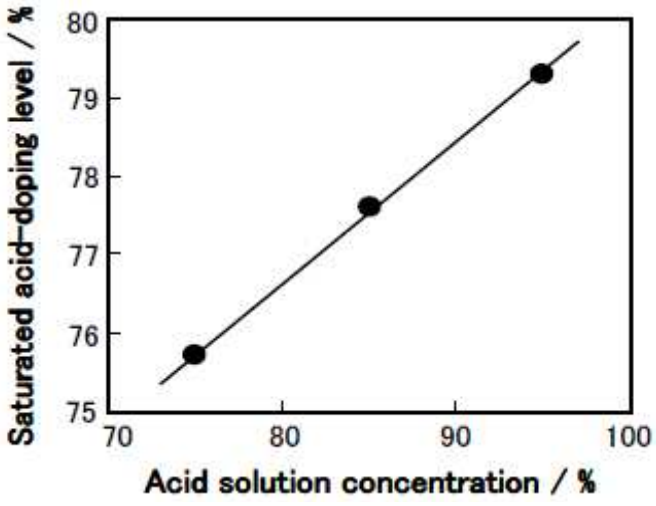

Fig.6.7 Relationship between AB-PBI saturated acid-doping level and acid solution concentration for immersion at 60℃

6.4.2 Influence of Acid-doping Levels on Cell Performances

Fig.6.8 shows the relationship between the cell voltage following 1,200h of operation at 0.2Acm^{-2} and the acid-doping level for three cells with ABPBI membranes. The cell voltage data was taken from Figs.6.4 and 6.6. It can be seen that the cell voltage generally increases with acid-doping level, although the increase becomes more gradual at higher doping levels. Judging from the trend in Fig.6.8, an acid-doping level of at least 76% is required to achieve a high cell voltage.

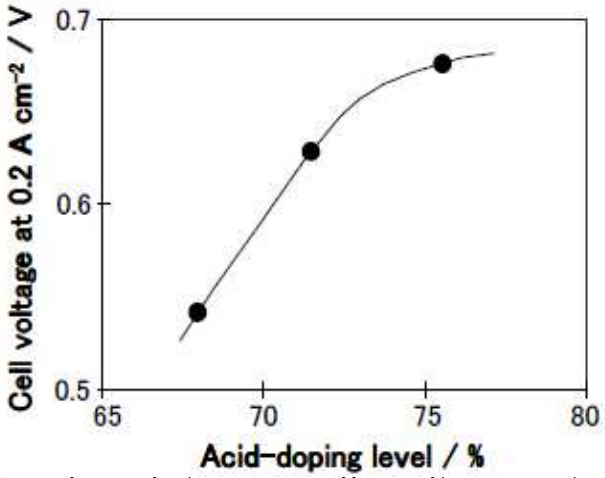

Fig.6.8 Relationship between cell voltages at 0.2Acm^{-2} and acid-doping level for AB-PBI membrane.

Fig.6.9 shows the corresponding results for the cell internal resistance following 500h of operation, where the data for the three cells is taken from Fig.6.5. The trend is seen to be opposite to that for the cell voltage.

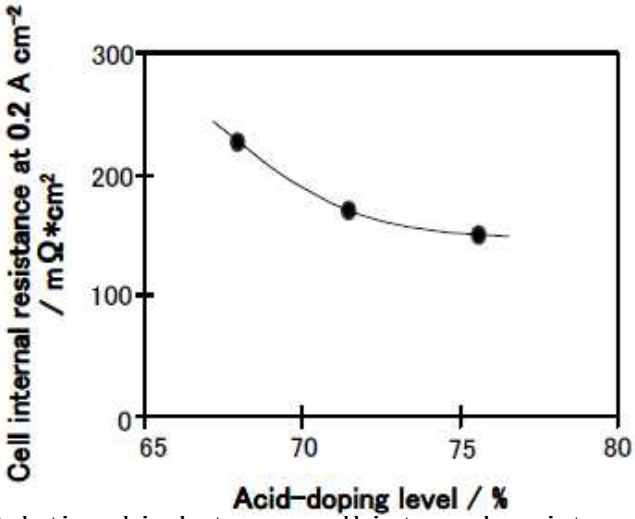

Fig.6.9 Relationship between cell internal resistance at 0.2Acm^{-2} and acid-doping level for ABPBI membrane.

6.4.3 Influence of Membrane Thinning on Cell Voltage Decline

In a previous study [4], it was shown that the drop in voltage for a cell with a PBI membrane during 14,000h of operation (see Fig6.10) was mainly caused by phosphoric acid depletion due to evaporation. In addition, it was found that the PBI electrolyte membrane was decomposed. The majority of the dissolved PBI had migrated to the catalyst layers, together with a large amount of the phosphoric acid that had been present in the membrane. This decomposition led to a thinning of the PBI membrane, which resulted in cross-leakage of hydrogen and air, and this was thought to cause a faster drop in voltage for operation periods longer than 14,000h.

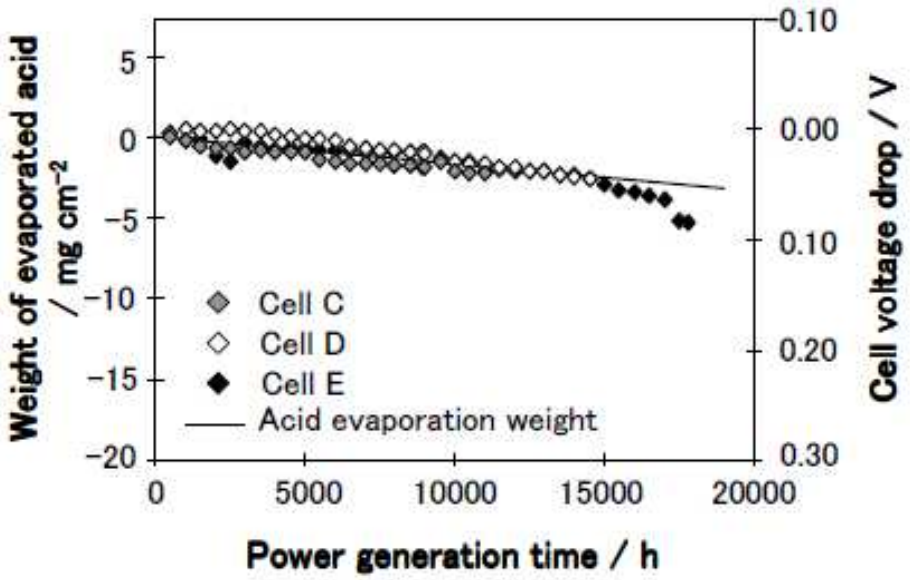

Fig.6.10 Long-term power generation test results for Cells C, D and E with PBI membrane operated for 12,000, 15,000 and 17,800h, respectively

In addition, the results of the same study indicated that this accelerated voltage drop was not strongly influenced by an increase in the electrocatalyst particle size [3]. In fact, as shown in Fig.6.6, although the voltage of Cell E with the PBI membrane decreased by 10% during 17800h of operation, that of Cell G with the ABPBI membrane decreased by only 4.4% during 17,500h of operation, and this was mainly due to two accidental shutdowns of the test station that caused phosphoric acid to leak from the cell as its temperature decreased to room temperature. Since the difference between Cell E and Cell G was the type of membrane used, these results also support the idea that the accelerated voltage drop was caused by

degradation of the PBI membrane rather than an increase in the electrocatalyst particle size.

To confirm this, an EPMA post-analysis was carried out on cross sections of MEAs removed from Cell F and G, following operation for 1,000 and 17,500h, respectively. The results were then compared with those previously obtained for Cell A and Cell E with PBI membranes, following operation for 0 and 17,800h, respectively [4].

Figs.6.11 (a), (b), (c) and (d) show cross-sectional SEM images of MEAs from Cells A, E, F and G, respectively, following the power generation tests. It can be seen that for the cells with the PBI membranes, a large decrease in the membrane thickness occurred between 0 and 17,800h of operation. However, this is not the case for the cells with the AB-PBI membranes, for which almost no change in membrane thickness is observed between 1,000 and 17,500h of operation. These results verify that decomposition and

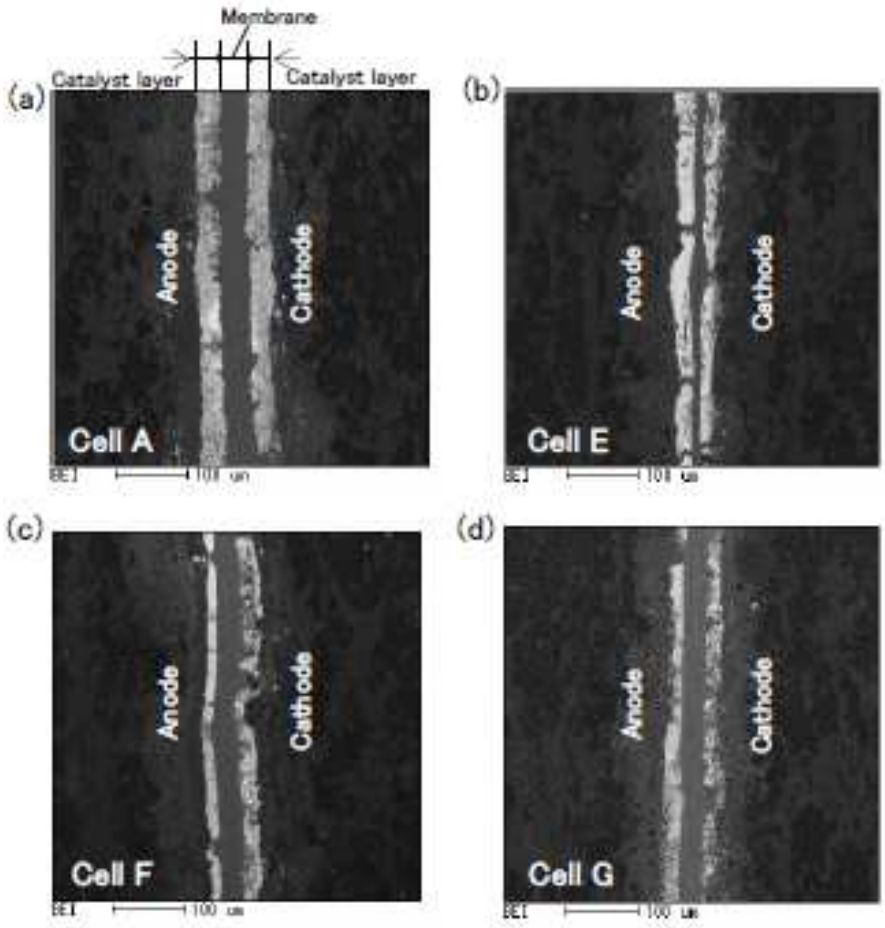

Fig.6.11 Cross-sectional SEM images of MEAs from the cell. (a) Cell A with PBI membrane non-operated, (b) Cell E with PBI membrane operated for 17,800h, (c) Cell F with AB-PBI membrane operated for 1,000h, and (d) Cell G with ABPBI membrane operated for 17,500h.

thinning can be suppressed by chemical cross-linking.

Fig.6.12 shows the change in membrane thickness as a function of final operation time for Cells A to E and Cells F to G. Each point represents an average of fifty measurements of the membrane thickness from the SEM images, with the spread in values being represented by the error bars. It can be seen that for the PBI membranes, the thinning process begins to accelerate at about 14,000h. On the other hand, for the AB-PBI membranes, almost no thinning is observed over the entire test period.

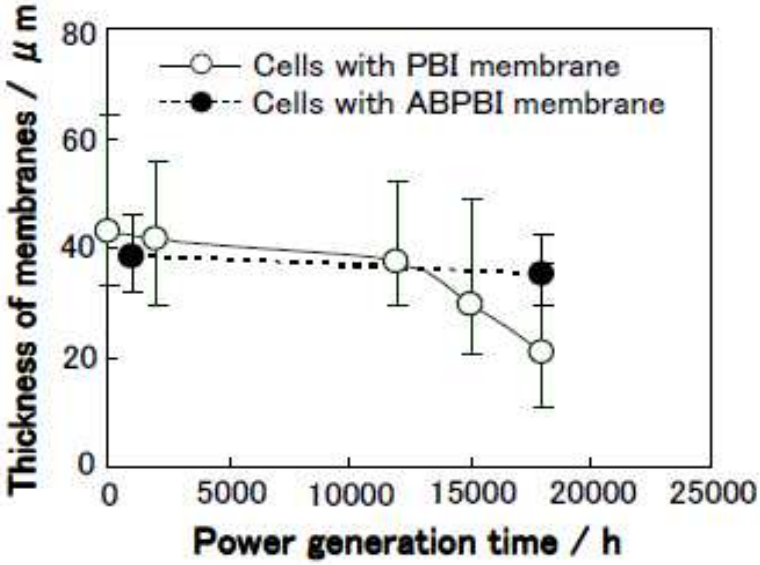

Fig.6.12 Changes in membrane thickness with operation time for cells with PBI and AB-PBI membranes.

Figs.6.13 (a) and (b) show cross-sectional EPMA elemental mapping

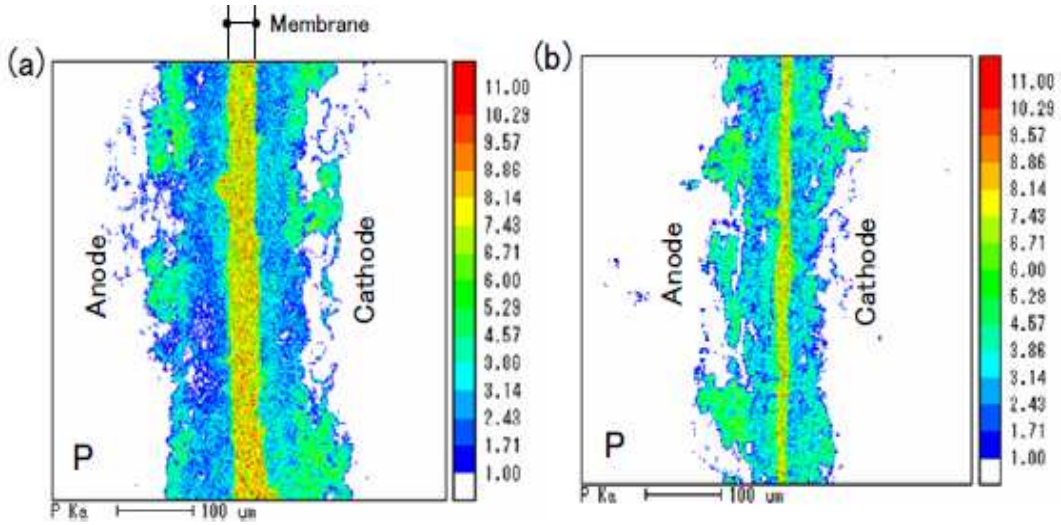

Fig.6.13 Cross-sectional EPMA color mapping images for phosphorous in MEAs from cells with PBI membranes. (a) Cell A non-operated, (b) Cell E operated for 17,800h [4].

images for phosphorous in MEAs from Cells A and E, respectively. Again, clear membrane thinning is apparent after 17,800h of operation, and a decrease in phosphoric acid concentration has occurred not only in the catalyst layers but also in both gas diffusion layers.

Figs.6.14 (a) and (b) show cross-sectional EPMA color mapping images for phosphorous and platinum, respectively, in the MEA from Cell F following 1000 h of operation. Figs.6.15 (a) and (b) show the corresponding images for Cell G following 17,500h of operation. Comparing Fig.6.14 (a) and Fig.6.15 (a), it is clear that the thickness of the AB-PBI membrane has not changed and the phosphoric acid concentration has remained high in the

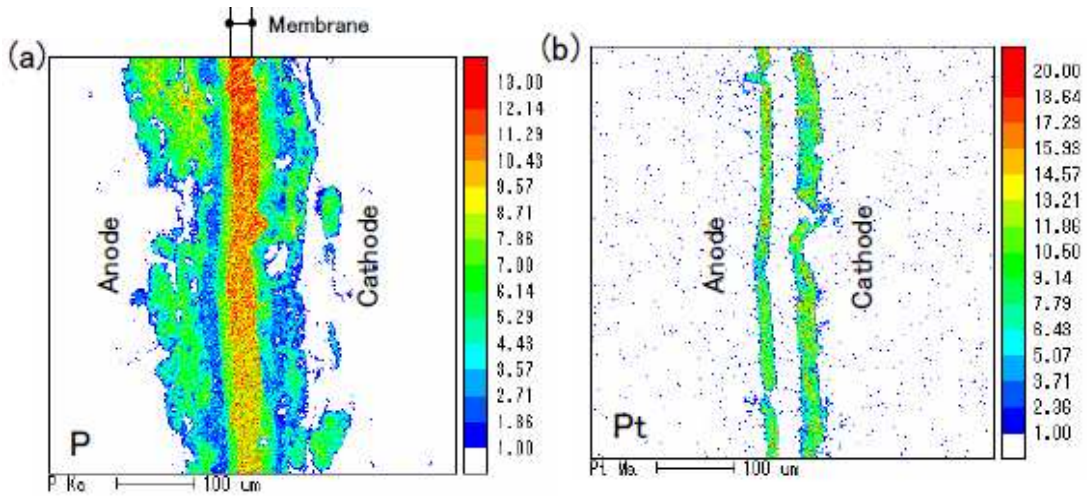

Fig.6.14 Cross-sectional EPMA of MEA from Cell F with AB-PBI membrane, operated for 1,000h. (a) Color mapping for phosphorous, (b) Color mapping for platinum

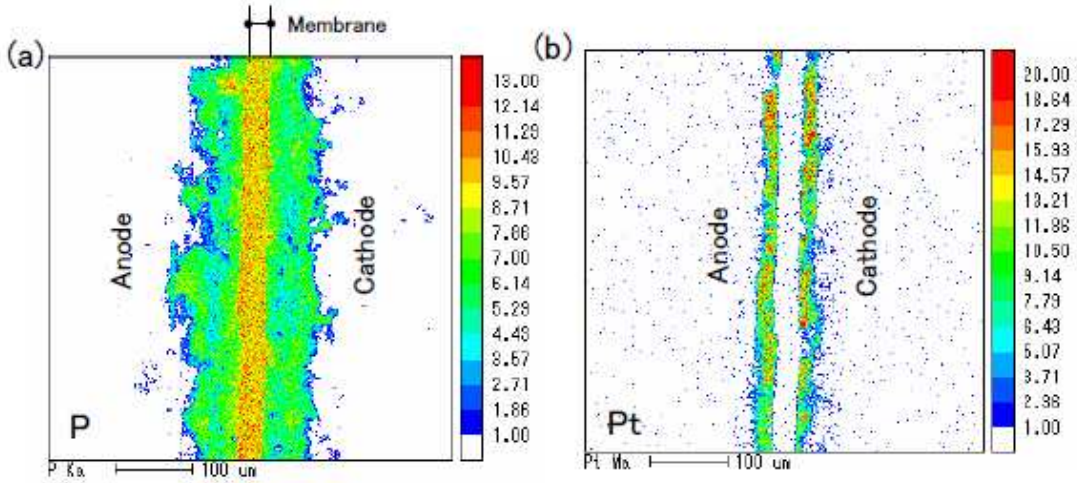

Fig.6.15 Cross-sectional EPMA of MEA from Cell G with AB-PBI membrane, operated for 17,500h. (a) Color mapping for phosphorous, (b) Color mapping for platinum

catalyst and gas diffusion layers. Furthermore, a comparison of Fig.6.14 (b) and Fig.6.15 (b) shows that the platinum content in the electrocatalysts has remained relatively constant during operation.

6.5 Conclusions

Power generation tests were carried out on HT-PEMFCs with ABPBI membranes doped with phosphoric acid to levels of 62%, 72% and 76% in order to evaluate the influence of the acid-doping level on cell performance. Tests were also carried out on two cells with an acid-doping level of 78% at a current density of 0.2Acm^{-2} for 1,000 and 17,500h in order to verify that the stability of the electrolyte membrane has the main influence on the durability of HT-PEMFCs up to around 20,000h. The latter cells were post-analyzed using SEM and EPMA. The results were compared with those for cells with PBI membranes, allowing the mechanism of cell performance reduction in HT-PEMFCs to be clarified.

The long-term test results showed although a voltage decrease of 10% occurred for the cell with the PBI membrane, the decrease was only 4.4% for the cell with the AB-PBI membrane, and this was mainly due to accidental shutdowns of the test station during the testing period.

The results of the post-analysis indicated that, following cell operation for 17,500h, the AB-PBI membrane maintained its original thickness, and that the phosphoric acid remained high both in catalyst layers the gas diffusion layers. In addition, the platinum content in the electrocatalyst remained constant.

The reason why AB-PBI's cell showed better performance than PBI's cell will be discussed in the next stage.

References

[1] J.A. Asensio, S. Borros, P.G. Romero ; J. Electrochem. Soc. 151(2) (2004) A304.
[2] J.R.P. Jayakody, S.H. Chung, L. Durantio, H. Zhang, L. Xiao, B.C. Benicewicz, S.G. Greenbaum ; J. Electrochem. Soc. 154 (2007) B242.
[3] Y. Zhai, H. Zhang, D. Xing, Z.G. Shao ; J. Power Sources 164 (2007) 126.
[4] Y. Oono, A. Sounai, M. Hori ; J. Power Sources 210 (2012) 366.
[5] Y. Oono, T. Fukuda, A. Sounai, M. Hori ; J. Power Sources 195 (2010) 1007.
[6] L. A. Diaz, G. C. Abuin, H. R. Corti ; J. Power Sources 188 (2009) 45.
[7] J. A. Asensio, P. G-Romero ; Fuel Cells 5 (3) (2005) 336.
[8] Y. Oono, A. Sounai, M. Hori ; J. Power Sources 189 (2009) 943.
[9] J. Yu, Y. Yoshikawa, T. Matsuura, M.N. Islam, M. Hori ; Electrochem. Solid-State Lett. 8 (3) (2005) A152.
[10] J. Yu, T. Matsuura, Y. Yoshikawa, M.N. Islam, M. Hori ; Electrochem. Solid-State Lett. 8 (3) (2005) A156.

Chapter 7
Conclusions

Chapter 2, Chapter 3, Chapter 4, Chapter 5 and Chapter 6 are concluded as follows;

Chapter 2

For HT-PEMFC with PBI-H_3PO_4 membranes, it was clarified that the amounts of phosphoric acid doped in the membranes could be controlled by changing the phosphoric acid solution temperature and the immersion time in the phosphoric acid solution. Cell performance was improved by optimizing the amounts of phosphoric acid doped in the membrane and by the diffusion of phosphoric acid into the catalyst layer at the initial stage of cell operation. It was concluded that approximately 10mg cm^{-2} is the optimum amount of phosphoric acid for a catalyst layer with a thickness of approximately 20μm.

Chapter 3

For HT-PEMFC with PBI-H_3PO_4 membranes, it was clarified that, in the region from 150 to 190˚C, a higher cell temperature results in a higher cell voltage, but a shorter cell life. The reduction in cell voltage of approximately 20mV during the long-term power generation tests was considered to be caused both by aggregation of the electrode catalyst particles in the early stages of operation, in addition to the effects of crossover due to the depletion of phosphoric acid in the terminal stage. However, the cell power generation time exceeds 16,000h at 150˚C, and it is shown that enhanced long-term durability for practical applications can be achieved through effective management of phosphoric acid transfer.

Chapter 4

The electrode catalysts' aggregation mentioned in the chapter 3 was simulated with the UA-QCMD method which can calculate the affinity of Pt electrocatalysts with the support surface as a function of temperature.

With the method, the diameters of agglomerated electrocatalysts were theoretically estimated as 4.4, 5.5 and 6.2nm after aging about 1,000h at 150˚C, 170˚C, and 190˚C, respectively. These theoretical results showed good agreement with experimental TEM data.

The particle-based 3D CCL structure was modeled and the tortuosity values of pores, protons, and electrons inside of the constructed CCL microstructure model were three-dimensionally calculated. In case of reflecting only loss of electrochemical active surface, the calculation results showed that the cell voltage drops were 0.20, 0.74 and 5.02mV/h respectively. In case of reflecting both the losses of acid and electrochemical active surface area, those were 3.97, 11.73 and 47.78mV/h at 150, 170, and 190˚C, respectively,

On the other hand, the cell voltage drops experimentally obtained in the chapter 3 were 3.16, 10.09 and 44.01mV/h at 150, 170˚C and 190˚C, respectively、which agreed with theoretical results which were reflected both the losses of acid and electrochemical active surface area Thus, the reduction in measured cell voltage during the long-term operation of three cells was considered to be caused both by aggregation of the electrode catalyst particles and evaporation of acids.

Chapter 5

Long-term power generation tests were conducted on five identical single cells of HT-PEMFC with PBI-H_3PO_4 membranes at a temperature of 150˚C and a current density of 0.2Acm^{-2} for periods of up to 17,860h.

The results indicated that the cell voltage declined very gradually until 14,000h, after which a more rapid decrease occurred. The former was guessed to be caused by the active area decrease due to catalyst agglomeration and so on. And the latter was found to correlate well with decreases in the membrane thickness. It was also found that parts of the membrane became dissolved and migrated together with the phosphoric acid into the catalyst layers. Regions of the catalyst layers that were depleted of phosphoric acid were identified, which resulted in a reduction in the active area, and which is thought to be the cause of the accelerated drop in the cell voltage after about 14,000h of operation.

Chapter 6

Power generation tests were carried out on HT-PEMFCs with AB-PBI membranes doped with phosphoric acid to levels of 62%, 72% and 76% in order to evaluate the influence of the acid-doping level on cell performance.

Tests were also carried out on two cells with an acid-doping level of 78% at a current density of 0.2Acm^{-2} for 1,000 and 17,500h in order to verify that the stability of the electrolyte membrane has the main influence on the durability of HT-PEMFCs up to around 20,000h. The latter cells were post-analyzed using SEM and EPMA. The results were compared with those for cells with PBI membranes, allowing the mechanism of cell performance reduction in HT-PEMFCs to be clarified.

The long-term test results showed although a voltage decrease of 10% occurred for the cell with the PBI membrane, the decrease was only 4.4% for the cell with the AB-PBI membrane, and this was mainly due to accidental shutdowns of the test station during the testing period.

The results of the post-analysis indicated that, following cell operation for 17,500h, the AB-PBI membrane maintained its original thickness, and that the phosphoric acid remained high both in catalyst layers the gas diffusion layers. In addition, the platinum content in the electrocatalyst remained constant.

Future Works

In this study, the cell performance of 0.68V was achieved for a current density of 0.2Acm^{-2}, which almost reaches the goal of cell performance required for HT-PEMFC for residential use. Furthermore, the cell with a ABPBI-H_3PO_4 membrane was operated at the cell temperature of 150℃ for around 20,000 hours with the cell voltage drop rate of 1.3μVh^{-1}. Based on these results, it is estimated that a cell voltage drop is 73mV per 40,000 hours, which almost achieves the goal of cell voltage drop, less than 10% of peak cell voltage (680mV). Thus, the final goal of initial cell performance and long life is thought to be achieved, which is definitely supported by taking the cell degradation mechanism into consideration,

The residual issue for practical use of HT-PEMFC is daily-start and -stop (DSS) operation. Electric demands of ordinary households are lower during nighttime than during daytime. In order to keep high system efficiency through all day, the residential co-generation system had better be stopped during nighttime. However, if the cell temperature of HT-PEMFC drops to less than 100℃, phosphoric acid in membrane and catalyst layers are washed away. Consequently the cell voltage after DSS does not recover to that before DSS.

At present, the author has conducted DSS tests on the single cells of HT-PEMFC under various operation conditions. The results show that keeping such cells in the temperature range more than 100℃ during DSS operation, remarkable cell voltage drop has been not observed . The author intends to show such results in the future.

Acknowledgements

I am deeply thankful to Professor Michio Hori from Daido University, who advised me during this study. I am thankful to Professor Atsuo Sounai from Suzuka National College of Technology, Doctor Tomas Klicpera, and Takashi Fukuda from Daido University, who collaborated on this study. And I am thankful to Junko Kojima and Megumi Ishibashi, who supported for application of doctoral dissertation.